



**NAVAL
POSTGRADUATE
SCHOOL**

MONTEREY, CALIFORNIA

DISSERTATION

**DESIGN, TEST, AND EVALUATION OF A TRANSONIC
AXIAL COMPRESSOR ROTOR WITH SPLITTER
BLADES**

by

Scott Drayton

September 2013

Dissertation Co-Supervisors:

Garth V. Hobson
Anthony J. Gannon

Approved for public release; distribution is unlimited

THIS PAGE INTENTIONALLY LEFT BLANK

REPORT DOCUMENTATION PAGE			<i>Form Approved OMB No. 0704-0188</i>	
Public reporting burden for this collection of information is estimated to average 1 hour per response, including the time for reviewing instruction, searching existing data sources, gathering and maintaining the data needed, and completing and reviewing the collection of information. Send comments regarding this burden estimate or any other aspect of this collection of information, including suggestions for reducing this burden, to Washington headquarters Services, Directorate for Information Operations and Reports, 1215 Jefferson Davis Highway, Suite 1204, Arlington, VA 22202-4302, and to the Office of Management and Budget, Paperwork Reduction Project (0704-0188) Washington DC 20503.				
1. AGENCY USE ONLY (Leave blank)		2. REPORT DATE September 2013	3. REPORT TYPE AND DATES COVERED Doctoral Dissertation	
4. TITLE AND SUBTITLE DESIGN, TEST, AND EVALUATION OF A TRANSONIC AXIAL COMPRESSOR ROTOR WITH SPLITTER BLADES			5. FUNDING NUMBERS	
6. AUTHOR(S) Scott Drayton				
7. PERFORMING ORGANIZATION NAME(S) AND ADDRESS(ES) Naval Postgraduate School Monterey, CA 93943-5000			8. PERFORMING ORGANIZATION REPORT NUMBER	
9. SPONSORING /MONITORING AGENCY NAME(S) AND ADDRESS(ES) U.S. Army Research Laboratory, Mechanical Sciences Division, Research Triangle Park, NC 27709-2211			10. SPONSORING/MONITORING AGENCY REPORT NUMBER	
11. SUPPLEMENTARY NOTES The views expressed in this thesis are those of the author and do not reflect the official policy or position of the Department of Defense or the U.S. Government. IRB protocol number ____N/A ____.				
12a. DISTRIBUTION / AVAILABILITY STATEMENT Approved for public release; distribution is unlimited			12b. DISTRIBUTION CODE A	
13. ABSTRACT (maximum 200 words) A new design procedure was developed and documented that uses commercial-off-the-shelf software (MATLAB, SolidWorks, and ANSYS-CFX) for the geometric rendering and analysis of a transonic axial compressor rotor with splitter blades. Predictive numerical simulations were conducted and experimental data were collected at the NPS TPL utilizing the Transonic Compressor Rig. This study advanced the understanding of splitter blade geometry, placement, and performance benefits. In particular, it was determined that moving the splitter blade forward in the passage between the main blades, which was a departure from the trends demonstrated in the few available previous transonic axial compressor splitter blade studies, increased the mass flow range with no loss in overall performance. With a large 0.91 mm (0.036 in) tip clearance, to preserve the integrity of the rotor, the experimentally measured peak total-to-total pressure ratio was 1.69 and the peak total-to-total isentropic efficiency was 72 percent at 100 percent design speed. Additionally, a higher than predicted 7.5 percent mass flow rate range was experimentally measured, which would make for easier engine control if this concept were to be included in an actual gas turbine engine.				
14. SUBJECT TERMS Transonic, Axial Compressor, Rotor, Splittered, Splitter Blade, Design Tool			15. NUMBER OF PAGES 99	
			16. PRICE CODE	
17. SECURITY CLASSIFICATION OF REPORT Unclassified	18. SECURITY CLASSIFICATION OF THIS PAGE Unclassified	19. SECURITY CLASSIFICATION OF ABSTRACT Unclassified	20. LIMITATION OF ABSTRACT UU	

THIS PAGE INTENTIONALLY LEFT BLANK

Approved for public release; distribution is unlimited

**DESIGN, TEST, AND EVALUATION OF A TRANSONIC AXIAL
COMPRESSOR ROTOR WITH SPLITTER BLADES**

Scott Drayton
Commander, United States Navy
B.S., United States Naval Academy, 1995
M.S., Johns Hopkins University, 2007

Submitted in partial fulfillment of the
requirements for the degree of

DOCTOR OF PHILOSOPHY IN MECHANICAL ENGINEERING

from the

**NAVAL POSTGRADUATE SCHOOL
September 2013**

Author:

Scott Drayton

Approved by:

Garth V. Hobson
Professor
Dept. of Mech. & Aero. Engineering
Dissertation Committee Chair

John R. Lloyd
Visiting Distinguished Professor
Dept. of Mech. & Aero. Engineering

Hong Zhou
Professor
Dept. of Applied Mathematics

Christopher M. Brophy
Associate Professor
Dept. of Mech. & Aero. Engineering

Anthony J. Gannon
Assistant Research Professor
Dept. of Mech. and Aero. Engineering

Approved by:

Knox T. Millsaps, Chair, Dept. of Mech. and Aero. Engineering

Approved by:

Douglas Moses, Vice Provost of Academic Affairs

THIS PAGE INTENTIONALLY LEFT BLANK

ABSTRACT

A new design procedure was developed and documented that uses commercial-off-the-shelf software (MATLAB, SolidWorks, and ANSYS-CFX) for the geometric rendering and analysis of a transonic axial compressor rotor with splitter blades. Predictive numerical simulations were conducted and experimental data were collected at the NPS TPL utilizing the Transonic Compressor Rig. This study advanced the understanding of splitter blade geometry, placement, and performance benefits. In particular, it was determined that moving the splitter blade forward in the passage between the main blades, which was a departure from the trends demonstrated in the few available previous transonic axial compressor splitter blade studies, increased the mass flow range with no loss in overall performance. With a large 0.91 mm (0.036 in) tip clearance, to preserve the integrity of the rotor, the experimentally measured peak total-to-total pressure ratio was 1.69 and the peak total-to-total isentropic efficiency was 72 percent at 100 percent design speed. Additionally, a higher than predicted 7.5 percent mass flow rate range was experimentally measured, which would make for easier engine control if this concept were to be included in an actual gas turbine engine.

THIS PAGE INTENTIONALLY LEFT BLANK

TABLE OF CONTENTS

I.	INTRODUCTION.....	1
	A. MOTIVATION	1
	B. PREVIOUS WORK.....	1
	1. Wennerstrom Supersonic Axial Compressor Stage Incorporating Splitter Vanes	1
	2. Newer Developments	3
	C. OBJECTIVES	4
II.	DESIGN TOOLS	5
	A. ADAPTATION OF SANGER DESIGN METHODOLOGY	5
	B. INCORPORATION OF A SHOCK LOSS MODEL	9
	C. AUTOMATION	12
	1. Geometry Generation	14
	2. CFD Analysis.....	23
III.	DESIGN OF A TRANSONIC AXIAL COMPRESSOR ROTOR WITH SPLITTER BLADES.....	27
	A. OVERVIEW	27
	B. AERODYNAMIC DESIGN PROCEDURE.....	27
	C. STRUCTURAL ANALYSIS.....	35
	D. MODAL ANALYSIS	44
	E. RESULTS	45
IV.	DETAILED ANALYSIS	47
	A. BLADE TIP GAP INCORPORATION.....	47
	B. STEADY STATE COMPRESSOR MAPPING USING ANSYS CFX....	48
V.	EXPERIMENTAL FACILITY AND PROCEDURE	55
	A. TRANSONIC COMPRESSOR RIG AND INSTALLATION	55
	1. Compressor Installation and Instrumentation.....	55
	2. Measurement Devices	57
	3. Instrument Placement	57
	B. EXPERIMENTAL PROCEDURE.....	60
	C. DATA ACQUISITION AND REDUCTION.....	61
VI.	RESULTS	63
	A. EXPERIMENTAL RESULTS.....	63
	B. COMPARISON OF CFD TO EXPERIMENTAL RESULTS	67
VII.	CONCLUSIONS AND RECOMMENDATIONS.....	77
	A. CONCLUSIONS	77
	B. RECOMMENDATIONS.....	77
	LIST OF REFERENCES	79
	INITIAL DISTRIBUTION LIST	81

THIS PAGE INTENTIONALLY LEFT BLANK

LIST OF FIGURES

Figure 1.	Wennerstrom’s transonic axial compressor splittered rotor	2
Figure 2.	Wennerstrom’s tip section blade and passage geometry	3
Figure 3.	Sanger’s NPS transonic axial compressor rotor.....	5
Figure 4.	Sanger design method meridional plot geometry parameters.....	7
Figure 5.	Shock loss model: standing normal passage shock.....	9
Figure 6.	Rotor tip section inlet velocity triangle.....	10
Figure 7.	Rotor tip section outlet velocity triangle.....	11
Figure 8.	Rotor tip section combined velocity triangle	12
Figure 9.	TPL design tool process flow chart	13
Figure 10.	TPL design tool software suite	14
Figure 11.	HardCodeBlade blade input parameters	16
Figure 12.	HardCodeBlade passage input parameters.....	17
Figure 13.	Third-order spline fit for blade camber line distribution	18
Figure 14.	Third-order spline fit for blade thickness distribution	19
Figure 15.	Blade leading edge: third-order spline fit for thickness distribution	20
Figure 16.	Blade leading edge and trailing edge slope blending.....	21
Figure 17.	Blade leading edge: slope blending	22
Figure 18.	Example rotor total-to-total pressure ratio map	26
Figure 19.	Example rotor isentropic efficiency map.....	26
Figure 20.	TASR baseline: Numerically derived total-to-total pressure ratio map.....	30
Figure 21.	TASR baseline: Numerically derived isentropic efficiency map	30
Figure 22.	TASR spiral 1: Numerically derived total-to-total pressure ratio map.....	31
Figure 23.	TASR spiral 1: Numerically derived isentropic efficiency map.....	32
Figure 24.	TASR spiral 2: Numerically derived total-to-total pressure ratio map.....	33
Figure 25.	TASR spiral 2: Numerically derived isentropic efficiency map.....	33
Figure 26.	TASR spiral 3: Numerically derived total-to-total pressure ratio map.....	34
Figure 27.	TASR spiral 3: Numerically derived isentropic efficiency map.....	35
Figure 28.	TASR spiral 3b BladeHub_Full solid model	36
Figure 29.	TASR Spiral 3b structural analysis solid model	37
Figure 30.	Mesh used for structural and modal analysis.....	38
Figure 31.	High equivalent stress in TASR intermediate hub bolt holes	39
Figure 32.	High equivalent stress in TASR nose cone mount bolt hole	40
Figure 33.	Structural analysis modification 1 equivalent stress.....	41
Figure 34.	Stress analysis modification 2 equivalent stress	42
Figure 35.	Structural analysis: Numerically derived total-to-total pressure ratio map	43
Figure 36.	Structural analysis: Numerically derived isentropic efficiency map	43
Figure 37.	ANSYS Workbench project for static structural and modal analysis.....	44
Figure 38.	TASR Campbell diagram.....	45
Figure 39.	Final machined TASR blisk.....	46
Figure 40.	TASR radial deformation.....	48
Figure 41.	TASR gas path final mesh used for compressor mapping.....	50

Figure 42.	TASR 100 percent design speed numerically derived total-to total pressure ratio map	51
Figure 43.	TASR 100 percent design speed numerically derived isentropic efficiency map.....	52
Figure 44.	TASR numerically derived total-to-total pressure ratio map.....	53
Figure 45.	TASR numerically derived isentropic efficiency map.....	53
Figure 46.	TASR numerically derived power map	54
Figure 47.	TCR cross-section with the TASR installed	56
Figure 48.	TASR axially segmented casing	56
Figure 49.	TASR AS2 instrumentation station locations	58
Figure 50.	TCR configuration	60
Figure 51.	TASR 60 percent design speed experimentally measured total-to-total pressure ratio map	64
Figure 52.	TASR experimentally measured total-to-total pressure ratio map	65
Figure 53.	TASR experimentally measured isentropic efficiency map	65
Figure 54.	TASR experimentally measured power map	66
Figure 55.	TASR 100 percent speed near-stall experimental contour pressure plot.....	67
Figure 56.	TASR experimentally versus numerically determined total-to-total pressure ratio map	68
Figure 57.	TASR experimentally versus numerically determined isentropic efficiency map.....	69
Figure 58.	TASR experimentally versus numerically determined power map	70
Figure 59.	TASR 100 percent speed near-stall CFD contour pressure plot.....	71
Figure 60.	Kulite (-2) experimental versus numerical pressure traces.....	72
Figure 61.	Kulite (-1) experimental versus numerical pressure traces.....	73
Figure 62.	Kulite 0 experimental versus numerical pressure traces.....	73
Figure 63.	Kulite 1 experimental versus numerical pressure traces.....	74
Figure 64.	Kulite 2 experimental versus numerical pressure traces.....	74
Figure 65.	Kulite 3 experimental versus numerical pressure traces.....	75
Figure 66.	Kulite 4 experimental versus numerical pressure traces.....	75
Figure 67.	Kulite 5 experimental versus numerical pressure traces.....	76

LIST OF TABLES

Table 1.	Sanger Method Input Design Parameters	6
Table 2.	HardCodeBlade parameters	15
Table 3.	SolidWorksGen solid models	23
Table 4.	WriteSpreadsheet output data	25
Table 5.	TASR design constraints and goals	27
Table 6.	TASR design iterations	28
Table 7.	ANSYS Workbench mesh statistics for aerodynamic design.....	28
Table 8.	ANSYS Workbench solver settings for aerodynamic design	29
Table 9.	ANSYS Workbench mesh statistics for structural and modal analysis	37
Table 10.	Structural analysis blade geometry modifications	41
Table 11.	ANSYS Workbench mesh statistics for compressor mapping	49
Table 12.	ANSYS Workbench solver settings for compressor mapping.....	51
Table 13.	TASR instrumentation	59

THIS PAGE INTENTIONALLY LEFT BLANK

LIST OF ACRONYMS AND ABBREVIATIONS

CC	Compressibility Control
CFD	Computational Fluid Dynamics
CFX	The CFD simulation program in ANSYS Workbench. It is divided into CFX-Pre, CFX-Solver, and CFX-Post. It uses an implicit solver and can run both steady-state and transient simulations.
CFX-Pre	The portion of CFX where boundary conditions and solver settings are selected. The first CFX program used while conducting a simulation.
CFX-Solver	The portion of CFX that runs the solver program set up by CFX-Pre. It displays variable residuals as the simulation reaches convergence.
CFX-Post	The portion of CFX that performs post processing on the resultant flow field data from CFX-Solver.
GDMC	Global Dynamic Model Control
HSN	High Speed Numerics
LE	Leading Edge (blade)
MB	Main Blade
NPS	Naval Postgraduate School
NPSMF	NPS Military Fan
NTG	No Tip Gap
PS	Pressure Side
SB	Splitter Blade
SS	Suction Side
SolidWorks	A solid modeling program
TASR	TPL Axial Splittered Rotor
TE	Trailing Edge (blade)
TG	Tip Gap
TCR	Transonic Compressor Rig
TPL	Turbopropulsion Lab

THIS PAGE INTENTIONALLY LEFT BLANK

ACKNOWLEDGMENTS

A sincere thank you to my principal advisors, Dr. Garth Hobson and Dr. Anthony Gannon, for their guidance and patience. Their insight and prodding was instrumental in ensuring my research was relevant, focused, and stayed on track. I would also like to thank Professors Jack Lloyd, Chris Brophy, and Hong Zhou for serving on my committee. The numerical simulation and experimentation required for this study would not have been possible without the outstanding support of Milan Vukceвич, John Gibson, and Chris Clay. Thank you to summer interns Ben Clemente, Steven Ambers, Jared VanCuren, and Joey Hall for their contributions. Finally, this study would not have been possible without generous funding from our project sponsor, Dr. Frederick Ferguson, at the U.S. Army Research Laboratory. I am very grateful for your support.

I would like to acknowledge the people that have had a significant positive impact on my life and prepared me to meet and overcome this challenge:

- My father, M. Stuart Drayton, for teaching me the value of hard work, perseverance, and education. His love of all things mechanical and career in the supercomputer industry ignited my enthusiasm for science and engineering. Thanks Dad, rest in peace.
- My father-in-law, Harry S. Pond III, for embracing me as part of his family, and his enthusiastic support, guidance, and friendship. Thanks Doc, rest in peace.
- Friend, Alan G. Poindexter, for sharing his infectious passion for life, loyal friendship, and frequent reminders that a spirited motorcycle ride is good for what ails you. Thanks Dex; rest in peace.
- Family friend and high school calculus teacher, Bob Nelson, for giving me a solid foundation in math and setting a positive example as an educator, service-oriented citizen, and family man. Thanks Bob!

Finally and most importantly, I would like to thank my beautiful wife, Alice, and wonderful children, Ellie (8) and Charlie (5). Without their unwavering love, support, humor, and words of encouragement this would not have been possible. In this spirit of gratitude, I dedicate this work to them.

THIS PAGE INTENTIONALLY LEFT BLANK

I. INTRODUCTION

A. MOTIVATION

Over the course of turbomachinery history splitter vanes have been used extensively in centrifugal compressors. Axial compressor rotors with splitter blades have been studied and shown potential for producing desirable performance characteristics (high stage pressure ratios and efficiencies), but have failed to gain traction due to perceived negative performance characteristics such as narrow mass flow operating ranges. According to Dr. Arthur J. Wennerstrom [1];

Starting in the late 1980s, three different engine companies have explored the concept with contemporary CFD tools and have tested some prototypes. Some of these results showed great promise. None of this work has been published openly yet, but this approach does appear to offer prospects for good diffusion factors on the order of 0.5 to 0.7 and possibly higher. The key to successful application will be the development of a splitter-vane design procedure that balances and optimizes the pressure distributions in the two passages created by the splitter vane. An important component of this will be a viscous CFD code that handles shock waves, high diffusion, and separated regions well.

This study revisited axial compressor rotors with splitter blades by the design, build, test, and evaluation of a non-axisymmetric rotor with splitter blades that retains the positive performance characteristics while addressing the previously identified deficiencies. Axial compressor rotors with splitter blades will be desirable in large and smaller gas turbine applications such as helicopters and unmanned aerial vehicles.

B. PREVIOUS WORK

1. Wennerstrom Supersonic Axial Compressor Stage Incorporating Splitter Vanes

Starting in 1971, Dr. Arthur J. Wennerstrom [2] and co-workers at the Fluid Dynamics Research Laboratory, Aerospace Research Laboratories, Wright-Patterson Air Force Base, Ohio designed and tested a variant of a supersonic axial compressor stage that incorporated splitter vanes in the aft section of the rotor passage. This study resulted in a rotor that contained 30 main blades and 30 splitter blades depicted in Figure 1.

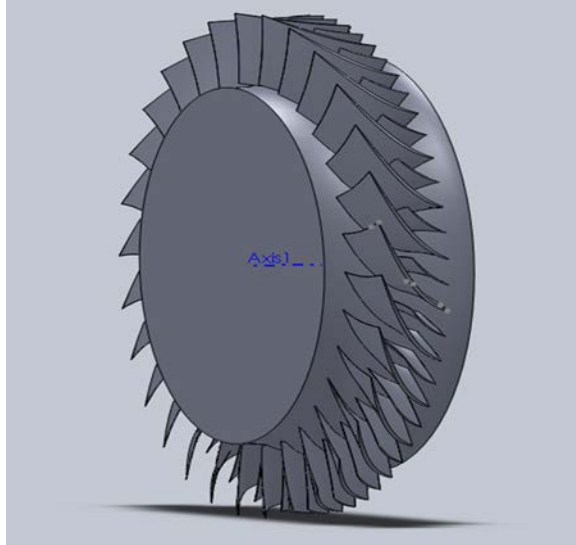


Figure 1. Wennerstrom's transonic axial compressor splitter rotor

The splitter blade camber line duplicated the camber line of the main blades and was circumferentially positioned exactly midway between main blades. The splitter blades extended the full radial span and their leading edges were placed halfway between the inlet and exit planes of the rotor. Additionally, the trailing edges of the splitter blades were in the same axial plane as the trailing edges of the main blades as shown in Figure 2. At 100 percent design speed, Wennerstrom's rotor achieved an experimentally measured peak total-to-total pressure ratio of 3.47 and a peak total-to-total isentropic efficiency of 85 percent. Detracting from these impressive results was a very narrow mass flow rate range of 3 percent.

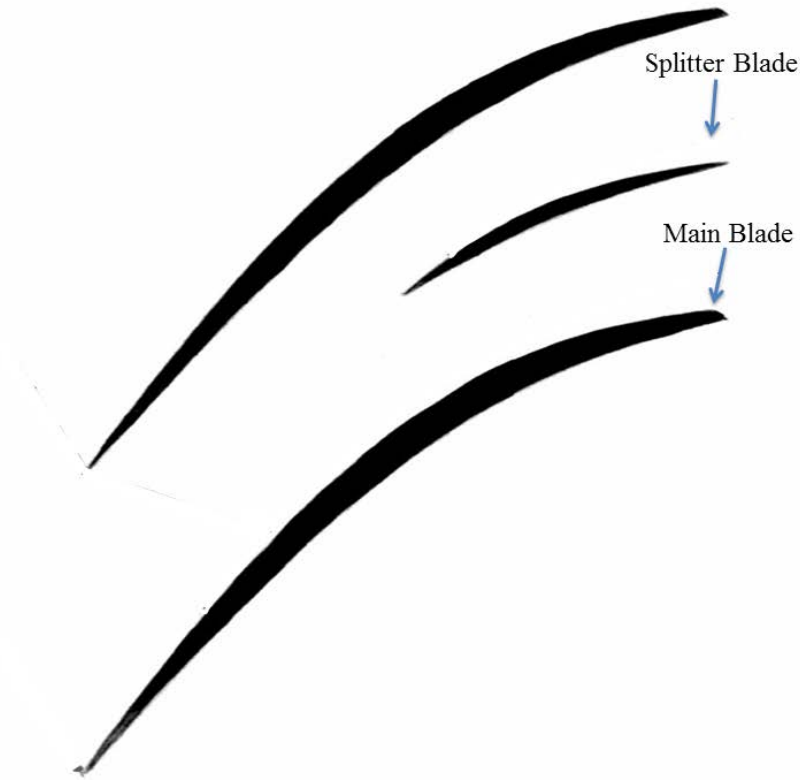


Figure 2. Wennerstrom's tip section blade and passage geometry

2. Newer Developments

Tzuoo, et al. [3] revisited Wennerstrom's work and developed a design methodology that combined a meridional flow calculation, an arbitrary blading design procedure, and 3-D inviscid and viscous analyses. Their methodology advanced the overall design approach of splintered axial compressor rotors and was demonstrated via analyses of Wennerstrom's splintered rotor showing the importance of 3-D viscous effects.

McClumphy [4] focused on the numerical analysis of tandem airfoils in the rear stages of a core axial-flow compressor in subsonic conditions. This work advanced the understanding of tandem rotor fluid mechanics providing a better understanding of forward and aft blade behavior.

C. OBJECTIVES

The object of this study is design, test, and evaluate a transonic axial compressor rotor with splitter blades. A brief outline of the study is as follows:

- Development of an in-house design tool for rapid rotor geometry and solid model generation and aerothermodynamic performance evaluation.
- Design of a transonic axial compressor rotor with splitter blades.
- Numerical modeling and analysis of a transonic axial compressor splintered rotor.
- Experimental performance testing and evaluation of a transonic axial compressor splintered rotor.
- Validate the use of commercial-off-the-shelf software packages for the design, evaluation, and test of a modern, highly loaded transonic compressor rotor.
- Measurement of the unsteady pressures on the casing over the splintered rotor to determine the shock structure and tip leakage vortex interaction over the operating range of the compressor.

II. DESIGN TOOLS

A. ADAPTATION OF SANGER DESIGN METHODOLOGY

In the 1990s, a transonic axial rotor–stator stage was designed by Nelson L. Sanger of NASA Lewis Research Center exclusively for the Naval Postgraduate School (NPS) as a research and teaching tool. Sanger’s NPS transonic axial compressor rotor is shown in Figure 3. The design process and methodology followed is documented in Sanger [5, 6] which resulted in a low aspect ratio (1.2) rotor with a tip relative inlet Mach number of 1.3, and an overall stage pressure ratio of 1.57. Over the course of approximately ten years experimental and numerical investigations evaluated the Sanger compressor performance over a variety of operating speeds and conditions.



Figure 3. Sanger’s NPS transonic axial compressor rotor

Having proven that the Sanger design methodology was robust by extensive performance evaluation, parts of his work were adapted as a starting point for the design portion of this study. The preliminary design steps which he followed and documented in detail in reference 4 were coded in a MATLAB script. Initially the Sanger method required ambient conditions and gas properties and the input design parameters listed in Table 1.

Table 1. Sanger method input design parameters

Input Parameter Description	Definition
Stagnation Pressure Ratio	$PR = \frac{P_{02}}{P_{01}}$
Efficiency	$\eta = \frac{PR^{\frac{\gamma-1}{\gamma}} - 1}{TR - 1}$
Aspect Ratio	$AR = \frac{\text{Average Blade Height (ABH)}}{\text{Average Blade Chord (ABC)}}$
Stagger Angle	$SA = \tan^{-1} \frac{\text{Blade Tip Speed}}{C_{z1}}$
Specific Weightflow	$W = \frac{\dot{m}}{A_1}$
Axial Velocity Ratio	$AVR = \frac{C_{z2}}{C_{z1}}$
Tip Inlet Radius	TIR
Tip Exit Radius	TER
Hub Exit Radius	HER
Outer Casing Diameter	OCD

The Sanger method meridional plot geometry parameters are shown in Figure 4.

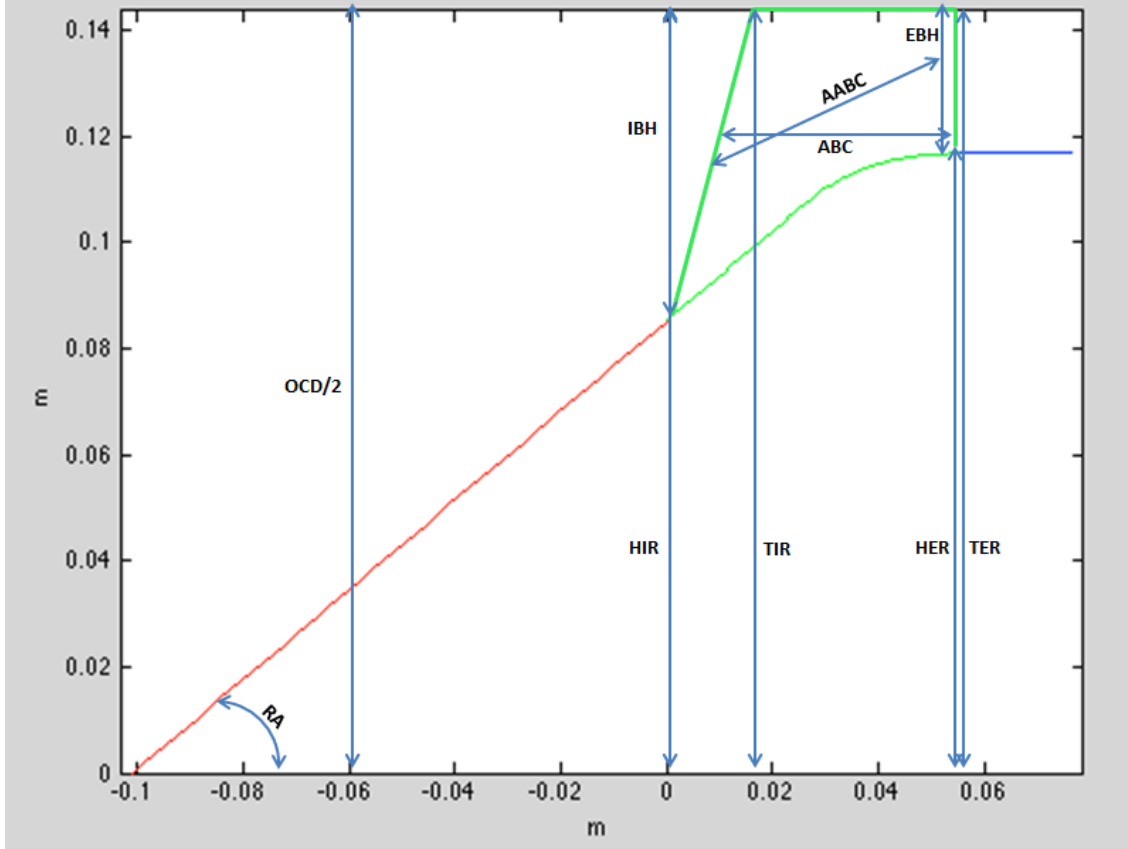


Figure 4. Sanger design method meridional plot geometry parameters

Following Sanger's methodology, the following parameters were calculated using the provided formulas and the input parameters from Table 1:

The stagnation temperature ratio was calculated by rearranging the equation defining efficiency in Table 1 and specifying the pressure ratio and efficiency.

$$\text{Stagnation Temperature Ratio (TR)} = \frac{T_{02}}{T_{01}} \quad (1)$$

By assuming static density ratio equal equals total density ratio. The rotor inlet-to-exit area ratio (ARAT) is calculated as follows:

$$\text{Area Ratio (ARAT)} = \frac{PR}{TR} \times AVR \quad (2)$$

Other terms used in the design method are outlined below.

$$\text{Rotor Exit Area } (A_2) = (TER^2 - HER^2) \times \pi \quad (3)$$

$$\text{Rotor Inlet Area } (A_1) = A_2 \times ARAT \quad (4)$$

$$\text{Mass Flow Rate } (\dot{m}) = W \times A_1 \quad (5)$$

$$\text{Total Inlet Area } (TIA) = \pi \times TIR^2 \quad (6)$$

$$\text{Total Exit Area } (TEA) = \pi \times TER^2 \quad (7)$$

$$\text{Hub Inlet Radius } (HIR) = \sqrt{\frac{HER - A_1}{\pi}} \quad (8)$$

$$\text{Inlet Blade Height } (IBH) = TIR - HIR \quad (9)$$

$$\text{Exit Blade Height } (EBH) = TER - HER \quad (10)$$

$$\text{Average Blade Height } (ABH) = \frac{IBH + EBH}{2} \quad (11)$$

$$\text{Average Blade Chord } (ABC) = \frac{ABH}{AR} \quad (12)$$

$$\text{Average Axial Blade Chord } (AABC) = ABC \times \cos\left(\frac{\pi \times SA}{180}\right) \quad (13)$$

$$\text{Spinner Ramp Angle } (RA) = \arctan\left(\frac{HER - HIR}{AABC}\right) \times \frac{\pi}{180} \quad (14)$$

$$\text{Ramp Slope } (RS) = \frac{HER - HIR}{AABC} \quad (15)$$

$$\text{Blade Tip Speed } (V_{tip}) = \text{Rotor Angular Velocity} \times TIR \quad (16)$$

$$\text{Rotor Power } (\text{PowerKW}) = \left(\frac{\dot{m} \times \frac{C \times T_{01}}{\eta}}{\rho_1}\right) \left(PR^{\frac{\gamma-1}{\lambda}} - 1\right) \quad (17)$$

$$\text{Inlet Absolute Velocity } (C_{z1}) = \frac{\dot{m}}{\rho_1 \times A_1} \quad (18)$$

$$\text{Inlet Speed of Sound } (a_1) = \sqrt{\gamma \times R \times T_{01}} \quad (19)$$

$$\text{Inlet Mach Number } (M_1) = \frac{C_{z1}}{a_1} \quad (20)$$

B. INCORPORATION OF A SHOCK LOSS MODEL

To provide a more accurate estimate of the blade angles required to start the design process for the transonic conditions of the splitted rotor passage, a normal shock was assumed to be situated in the passage as show in Figure 5.

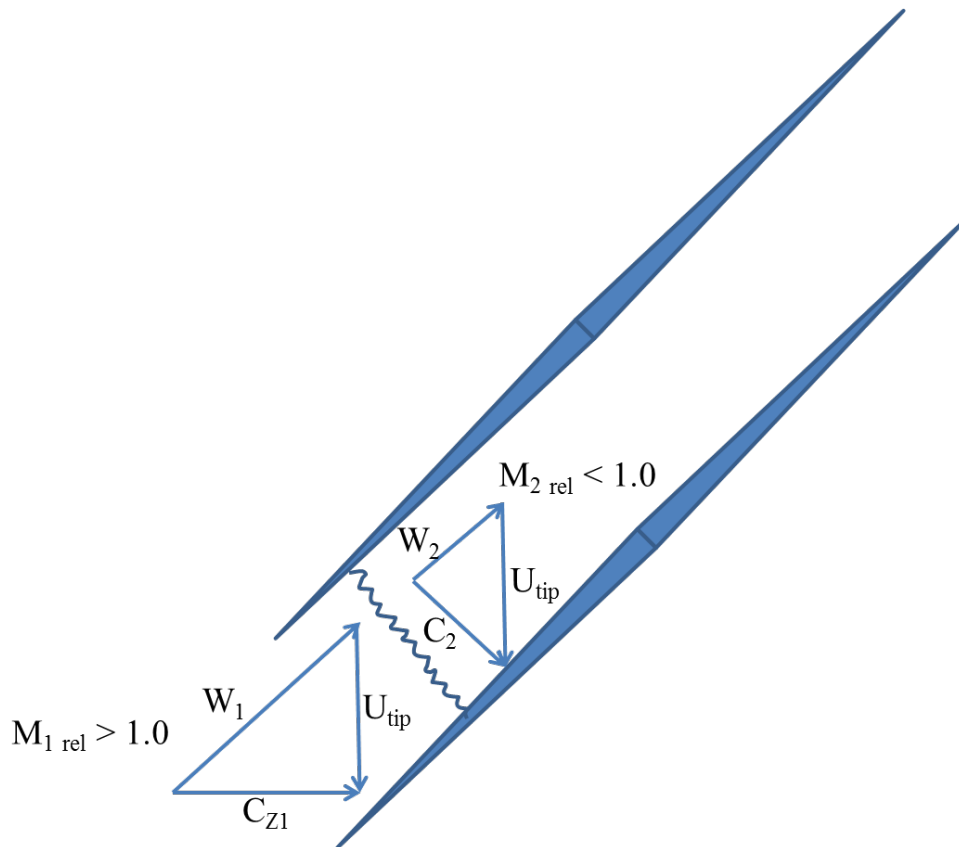


Figure 5. Shock loss model: standing normal passage shock

Calculations to construct the inlet velocity triangle were completed using the blade tip Mach number calculated earlier using the Sanger method. The tip section inlet velocity triangle is shown in Figure 6.

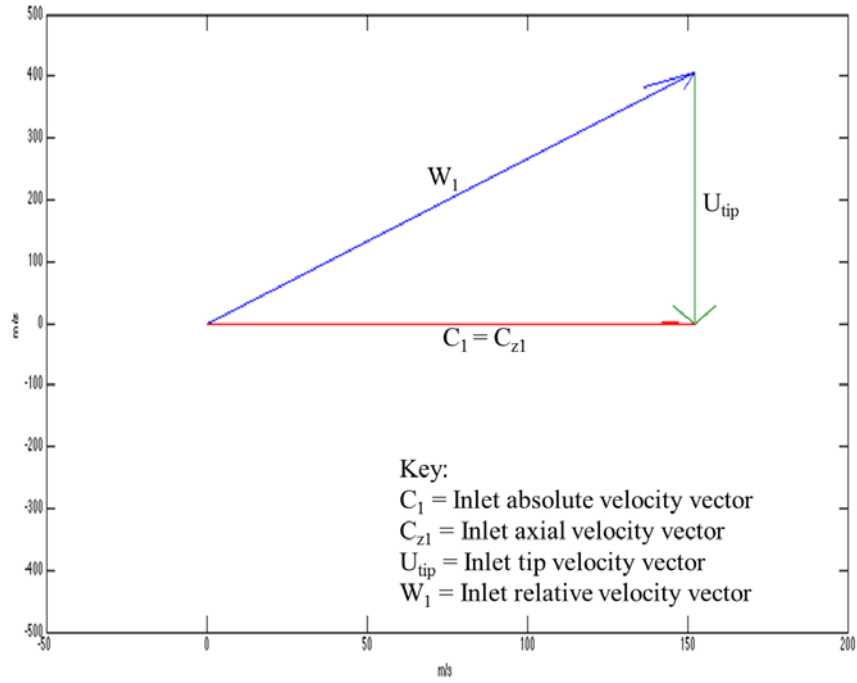


Figure 6. Rotor tip section inlet velocity triangle

Starting with the inlet relative Mach number at the tip as well as the specified AVR, a normal shock wave was computed using equation (21) to determine the downstream relative subsonic Mach number and associated velocity (W_2) shown in Figure 7.

$$M_2^2 = \frac{M_1^2 + \frac{2}{\gamma - 1}}{\left(\frac{2\gamma}{\gamma - 1}\right) (M_1^2 - 1)} \quad (21)$$

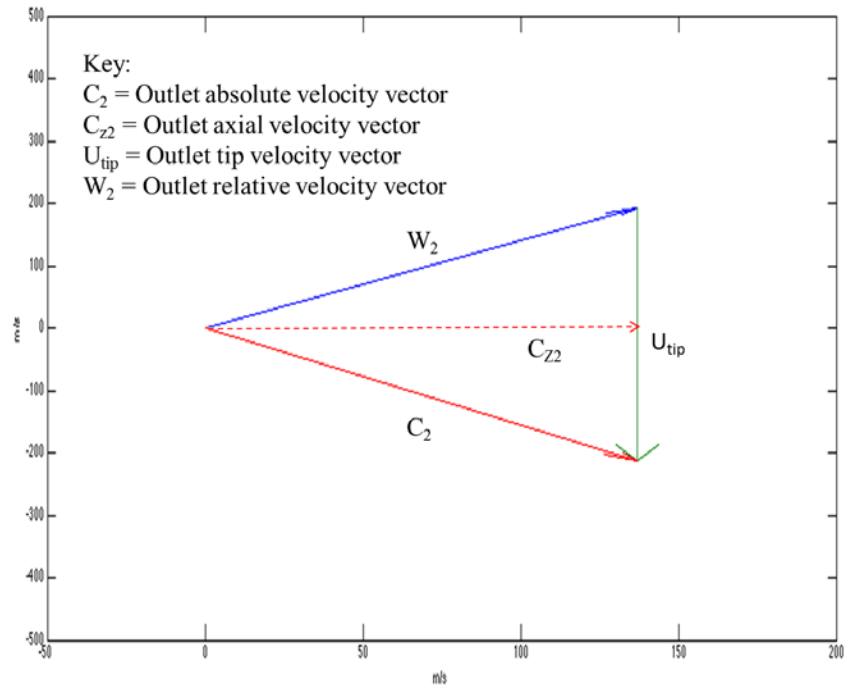


Figure 7. Rotor tip section outlet velocity triangle

The inlet and outlet velocity triangles are combined to show the net turning resulting from a normal shock located in the rotor passage. The combined velocity triangle with an AVR of 0.90 is shown in Figure 8.

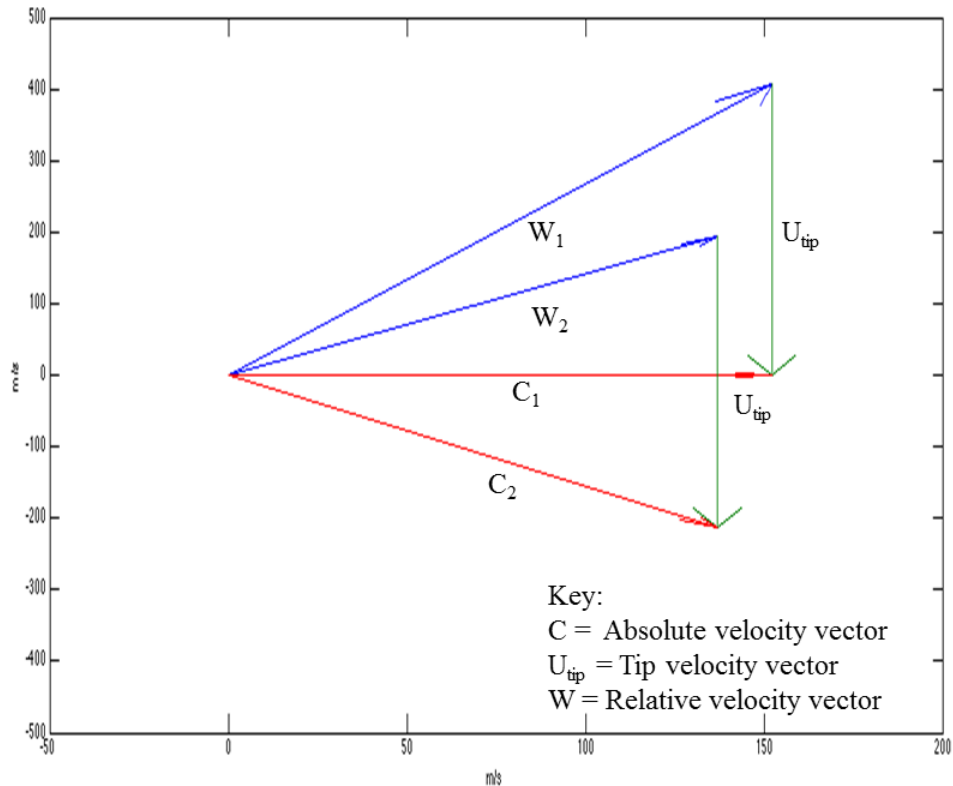


Figure 8. Rotor tip section combined velocity triangle

C. AUTOMATION

Recent computational fluid dynamics (CFD) studies at the NPS TPL have made extensive use of SolidWorks, a commercial solid modeling program, and ANSYS Workbench, a commercial simulation package that includes amongst others mesh generation, structural analysis, modal analysis, and CFD modules. The gas path analysis methods used in those previous studies are well documented in Boyter [7] and McNab [8]. Rotor gas path solid models were developed in SolidWorks and then imported into ANSYS CFX for performance analysis. The interface between SolidWorks and ANSYS required manual intervention. Any changes to the rotor gas path solid model required human-in-the-loop modification followed by manual updating of ANSYS Design Modeler and refreshing of ANSYS CFX setup for performance analysis. Additionally, to

predict the data required to produce a rotor performance map, throttling needed to occur via manual manipulation of the rotor gas path outlet pressure.

Given this study’s objectives and time constraints, it was apparent a design tool that automated geometry generation and CFD analysis as well as the interface between the standalone commercial software packages SolidWorks and ANSYS was required. MathWorks’ MATLAB technical computing language was chosen as the software package to interface with SolidWorks and ANSYS Workbench. Versions MATLAB R2012b, SolidWorks 2010, and ANSYS Workbench 14.0 were used for this study. The resultant design tool process flow chart is shown in Figure 9 and the MATLAB script calling structure is outlined in Figure 10.

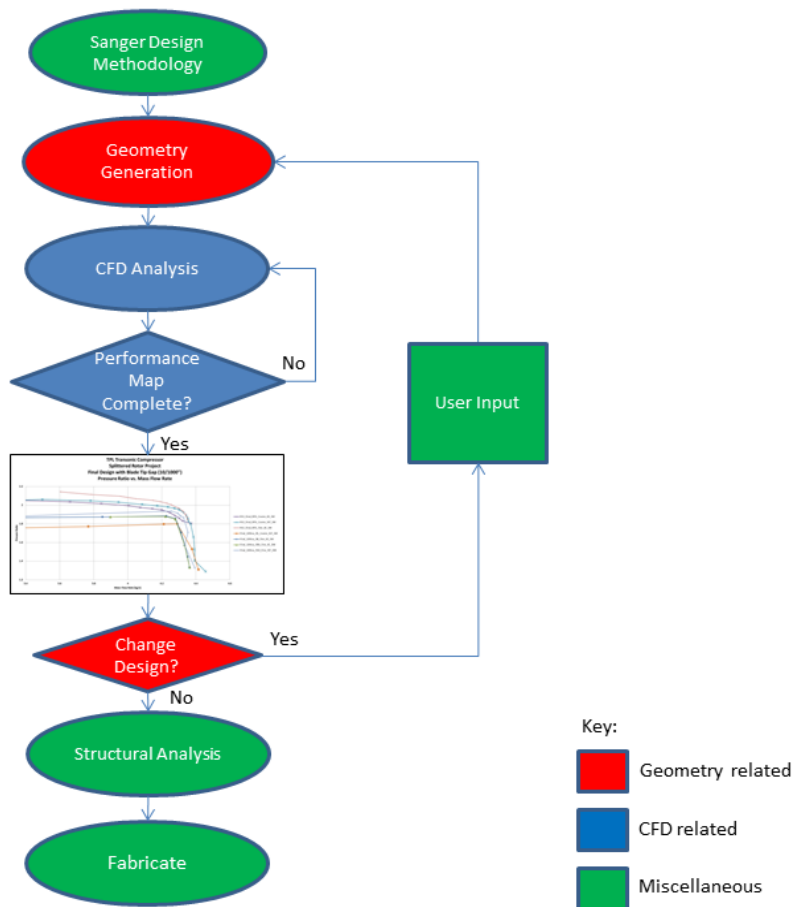


Figure 9. TPL design tool process flow chart

Each software routine and subroutine listed is available in a TPL technical note [9] and will be explained in detail in the following sections.

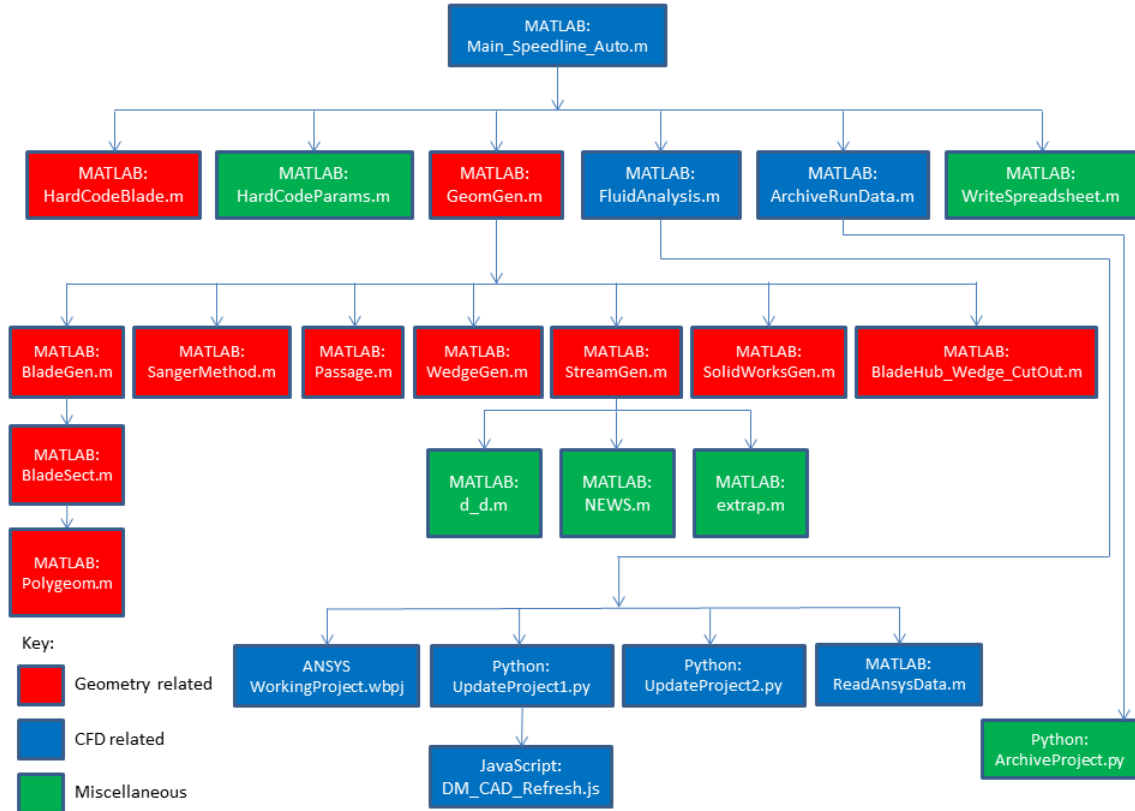


Figure 10. TPL design tool software suite

1. Geometry Generation

To begin the design process, the Sanger design methodology with the shock loss model incorporated was used to produce inlet and outlet velocity triangles. From these velocity triangles, overall stage flow turning angles were calculated and used to guide the user inputs for blade angles and thickness distributions. Armed with basic blade geometry parameters the TPL design tool was initiated by running the MATLAB script (*.m) Main_SpeedLine_Auto. Main_SpeedLine_Auto called the following six MATLAB scripts:

- HardCodeBlade
- HardCodeParams
- GeomGen
- FluidAnalysis
- ArchiveRunData
- WriteSpreadsheet

These MATLAB scripts will now be discussed. The HardCodeBlade script was responsible for loading all main and splitter blade user customizable parameters into Main_Speedline_Auto. Those parameters are shown in Table 2.

Table 2. HardCodeBlade parameters

Input Parameter Description	Input Parameter Symbol
Number of blade passages around the rotor assembly	Blade.PassNo
Number of blade sections used to generate the blade	Blade.S
Number of points that define half the blade profile	Blade.P
Blade heights at which properties are inputted	Blade.Heights
Blade chords at prescribed blade heights	Blade.Chord
Blade leading edge (LE) shift as a fraction of axial chord at prescribed blade heights	Blade.LE
Blade leading and trailing edge (TE) ellipse characteristics (minor axis/chord, eccentricity).	Blade.Edges
Blade chord control locations	Blade.Controls
Blade stagger at prescribed blade heights and blade chord control locations	Blade.Stagger
Blade element thickness at prescribed blade heights and blade chord control locations	Blade.Thickness
Blade offset representing the fraction of the passage to rotate each blade element (Main blades at 0.0)	Blade.Offset
Blade axial shift for all blades	Blade.MasterXShift
Fillet radius of all blades	Blade.Fillet

Input Parameter Description	Input Parameter Symbol
Centering feature (Boolean) specifying whether to center the main blade on the hub origin (true) or align the main blade leading edge with the origin (false) before applying the prescribed axial shift	Blade.Center

Some of the blade input parameters and passage input parameters listed above are shown in Figure 11 and Figure 12 respectively.

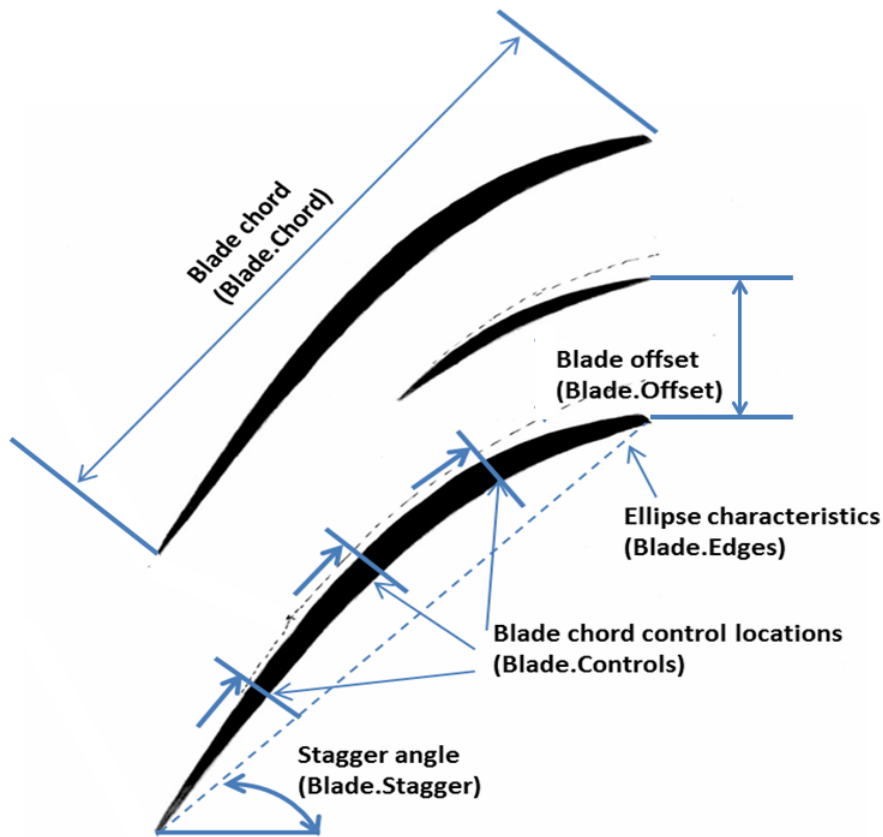


Figure 11. HardCodeBlade blade input parameters

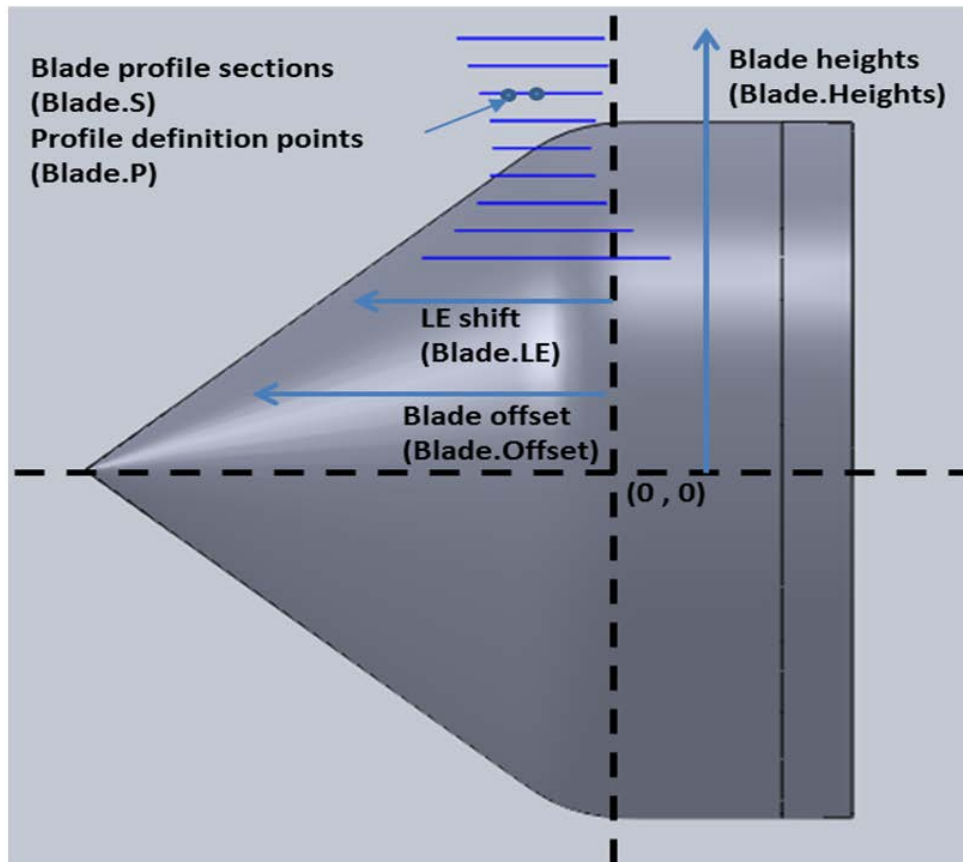


Figure 12. HardCodeBlade passage input parameters

The HardCodeParams script was responsible for loading the ambient conditions, gas properties, and the other constants and parameters previously listed in Table 1 into Main_Speedline_Auto.

The GeomGen script was the main routine responsible for blade, hub, spinner, and casing geometry generation and rotor and air wedge solid model generation in SolidWorks. To accomplish this GeomGen called the following seven MATLAB scripts:

- BladeGen
- SangerMethod
- Passage
- WedgeGen
- StreamGen
- SolidWorksGen

- BladeHub_Wedge_CutOut

Using the parameters passed in and described above, BladeGen started the blade profile generation process by calling the BladeSect script. Depending on the number of blade sections prescribed earlier, BladeGen generated blade sections by repeatedly calling BladeSect for both the main blade and splitter blade. BladeSect used a third-order spline between control points for camber line distribution as shown in Figure 13.

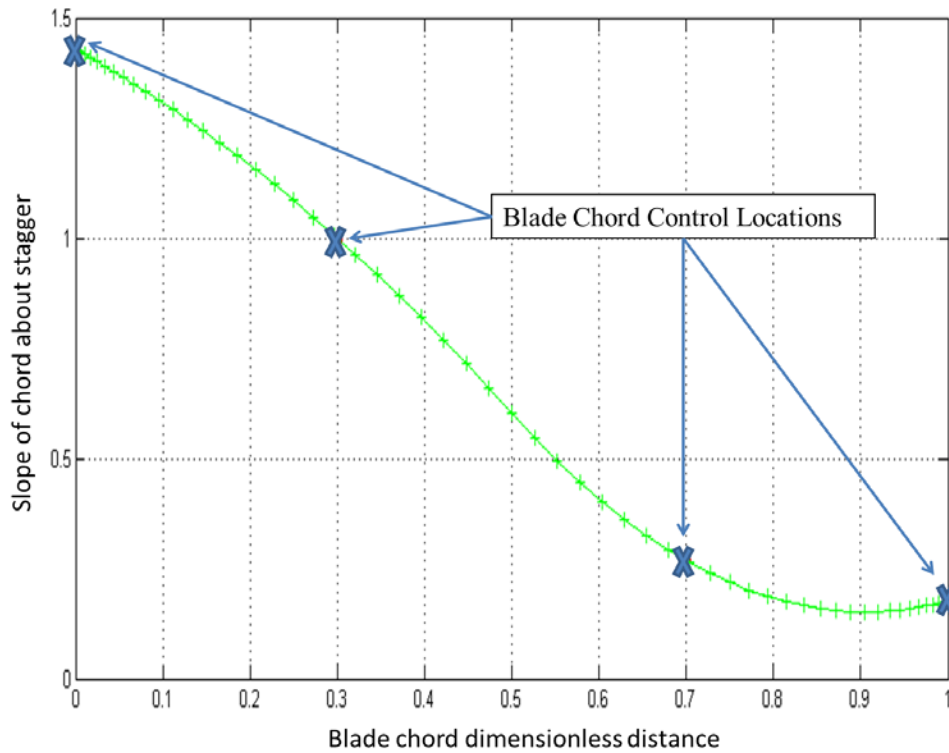


Figure 13. Third-order spline fit for blade camber line distribution

Blade profile generation continued by using a third-order spline between control points for thickness distribution as shown in Figure 14.

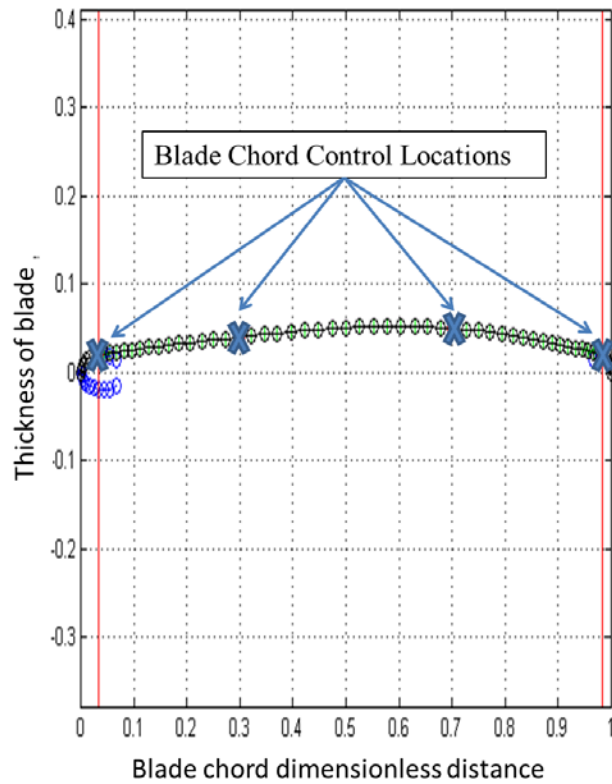


Figure 14. Third-order spline fit for blade thickness distribution

A magnification of Figure 14 at the blade leading edge which shows the blend point between the third order spline on the blade and the ellipse of the leading edge is shown in Figure 15.

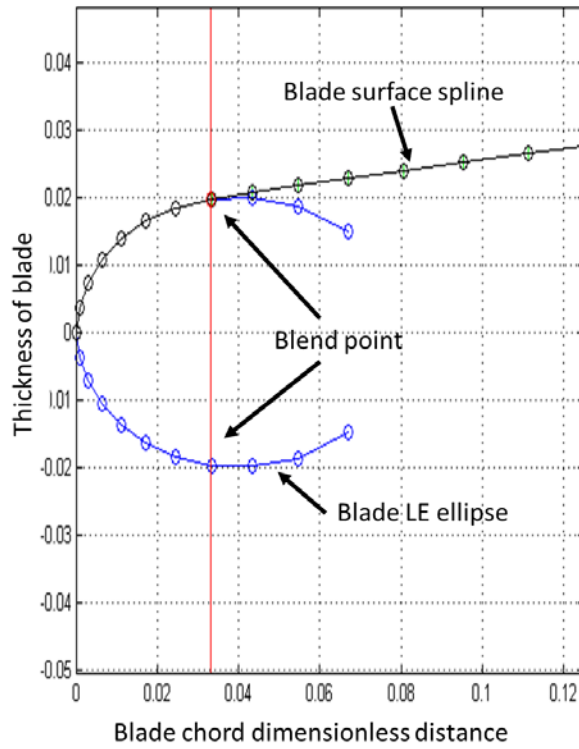


Figure 15. Blade leading edge: third-order spline fit for thickness distribution

The thickness distribution accounted for the user defined blade leading edge and trailing edge ellipse dimensions and eccentricity in blending to the blade surface by matching slopes at corresponding transition points as shown in Figure 16.

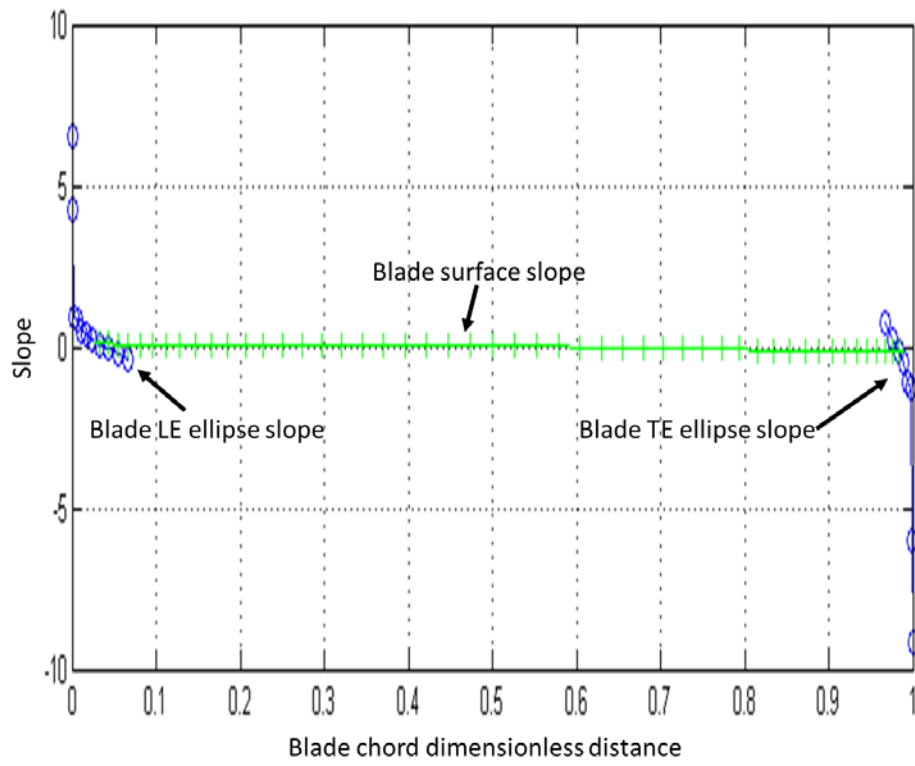


Figure 16. Blade leading edge and trailing edge slope blending

A magnification of Figure 16 at the blade leading edge is shown in Figure 17.

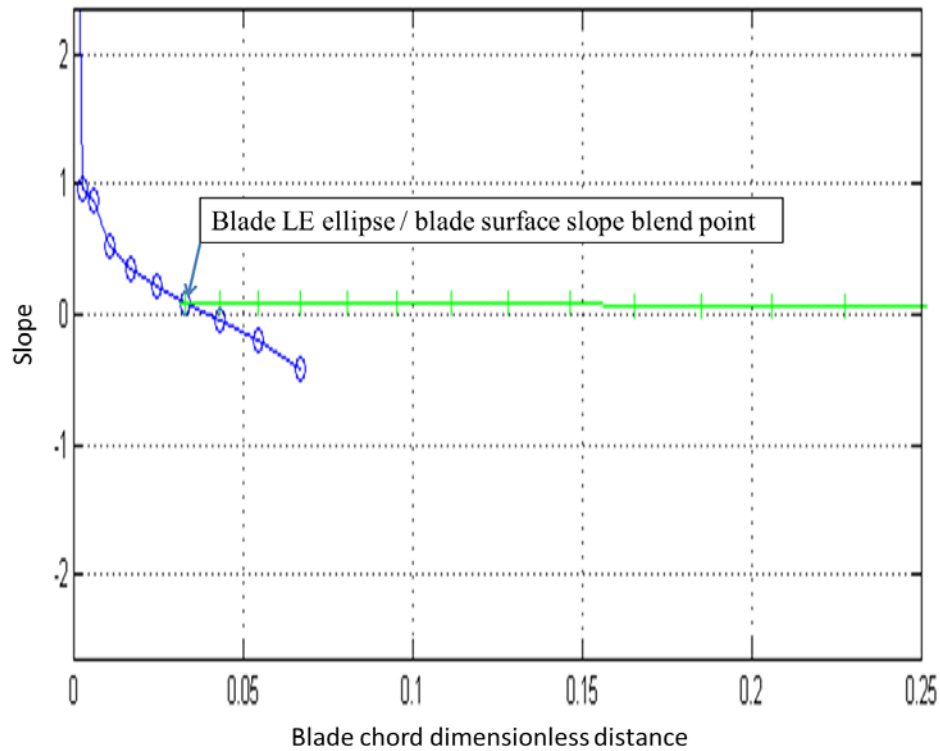


Figure 17. Blade leading edge: slope blending

Each blade section generated within BladeSect was stacked on its centroid by using the values passed from the polygeom MATLAB script. The polygeom script was derived from Sommer [10] and generated properties (area, x-centroid, y-centroid, perimeter, and area moments of inertia) of a planar polygon. These blade profiles were then passed to SolidWorks for solid model generation of the blade shapes.

With all required blade section geometries generated, GeomGen then used the SangerMethod, Passage, and WedgeGen MATLAB scripts to generate spinner, hub, passage and air wedge geometries. GeomGen then called MATLAB script StreamGen to calculate streamline radial positions with assistance from the following MATLAB scripts:

- d-d which utilized a numerical method to find the first derivative of two variables.
- NEWS which found the north, south, east, and west points of a non-uniform grid.

- extrap which performed quadratic extrapolation on three internal points to fit a quadratic polynomial in order to find the edge point.

With all required geometries and streamline data computed, GeomGen then called MATLAB script SolidWorksGen which sent commands to SolidWorks to generate a solid model of the full air wedge. This was accomplished by modifying the existing SolidWorks part files (*.SLDPRT) BasicRotor and BasicWedge with the geometry and streamline data generated earlier. Via its interface with SolidWorks, SolidWorksGen produced the solid models listed in Table 3.

Table 3. SolidWorksGen solid models

Solid Model	Description
BladeHub_Full	Complete rotor
BladeHub_Wedge_Cutout	Portion of rotor contained within a one-passage air wedge
AirWedge	One-passage air wedge without blade fillets
AirWedge_Fillets	One-passage air wedge with blade fillets
AirWedge_Upstream	Portion of one-passage air wedge removed upstream of rotor inlet area to reduce computational domain
AirWedge_Downstream	Portion of one-passage air wedge removed downstream of rotor exit area to reduce computational domain

All these solid models were saved as Parasolid (*.x_t) and SolidWorks (*.SLDPRT) files. These solid models could now be used for CFD and structural/modal analyses.

2. CFD Analysis

With solid models generated of the gas-path air wedge, automated numerical performance analysis using CFX within ANSYS Workbench was performed. This was desired in order to produce the data required to generate rotor performance maps. Main_Speedline_Auto continued operation by calling the MATLAB script FluidAnalysis to produce a single speed line from open throttle (zero back pressure) to near stall. FluidAnalysis completed the following calls:

- WorkingProject.
- UpdateProject1 or UpdateProject2
- ReadAnsysData

When ANSYS Workbench was opened the Python script (*.py), UpdateProject1, utilized a JavaScript file (*.js), DM_CAD_Refresh, to update the project geometry in the existing complete rotor air wedge simulation saved as the ANSYS Workbench Project (*.wbpj). Once the geometry was updated in ANSYS CFX DesignModeler, the mesh was updated in ANSYS CFX Meshing. The Python script (*.py) UpdateProject2 was used in subsequent runs when the geometry and mesh did not need refreshing in ANSYS DesignModeler and ANSYS CFX Meshing and only the rotor back pressure was increased. FluidAnalysis then passed the desired rotor outlet pressure and angular velocity to ANSYS CFX-Pre to initiate CFX-Solver settings prior to the simulation. Once CFX-Solver completed the simulation, the results were collected in CFX-Post. At the completion of the simulation, FluidAnalysis used the MATLAB script ReadAnsysData to read the values ANSYS saved to the file SavedOutput.dat. These values were displayed in the MATLAB Command Window for user interpretation.

At this point FluidAnalysis had finished running and control was passed back to Main_Speedline_Auto which then called the MATLAB script ArchiveRunData. This script created a new directory and copied all project files (.m, .js, .py, .x_t, and .SLDPRT) into the new directory. It also triggered an ANSYS script to save the ANSYS WorkBench Project WorkingProject into an archive file in the new directory. Finally, Main_Speedline_Auto called the MATLAB script WriteSpreadsheet to save specific data generated in the simulation to an Excel spreadsheet (*.xls) titled “Results.” The WriteSpreadsheet output data is shown in Table 4.

Table 4. WriteSpreadsheet output data

Parameter	Units
Outlet Pressure	atm
Angular Velocity	RPM
Inlet Mass Flow	kg/s
Outlet Mass Flow	kg/s
Total-to-Total Isentropic Efficiency	None
Outlet Total Pressure	Pa
Inlet Total Pressure	Pa
Total-to-Total Pressure Ratio	None
Power	W

This automated CFD analysis process repeated for each rotor outlet pressure increment specified in Main_Speedline_Auto. The Excel spreadsheet was updated with the data from each simulation at each rotor outlet pressure. The automation terminated when on the current simulation the parameter of interest (pressure ratio, efficiency, power, etc) specified in Main_Speedline_Auto was below the same parameter on the previous simulation or was not a valid number. The cumulative data stored in the spreadsheet was used to map rotor performance graphically. An example rotor pressure ratio performance map is shown in Figure 18. An example rotor efficiency performance map is shown in Figure 19.

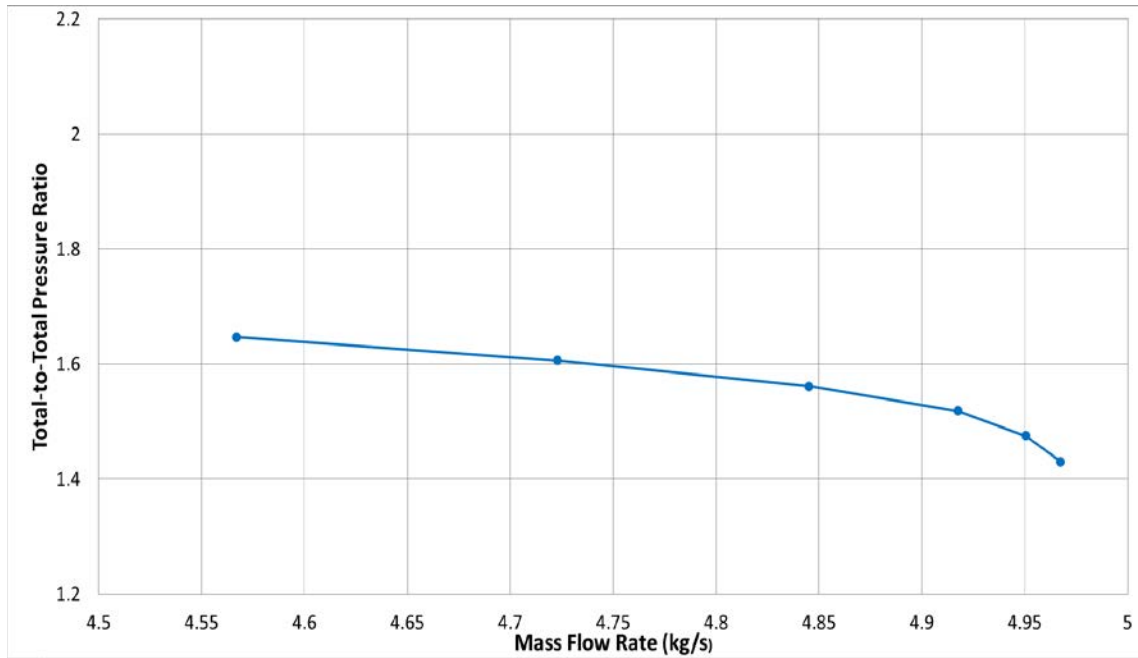


Figure 18. Example rotor total-to-total pressure ratio map

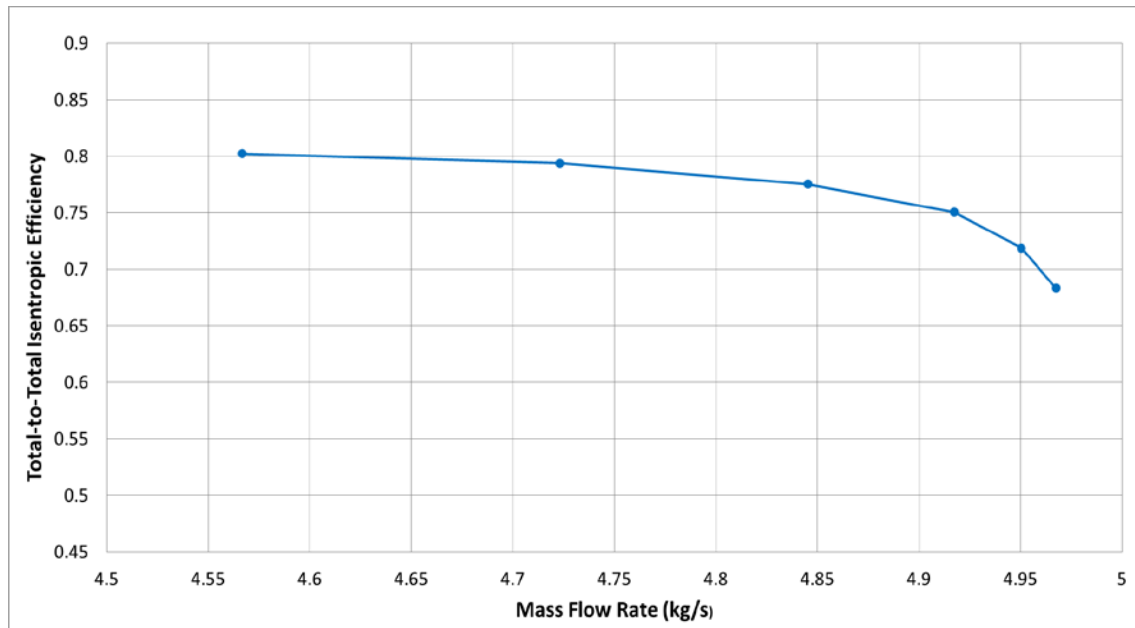


Figure 19. Example rotor isentropic efficiency map

III. DESIGN OF A TRANSONIC AXIAL COMPRESSOR ROTOR WITH SPLITTER BLADES

A. OVERVIEW

The purpose of this section is to describe how the design tool detailed in the previous section was used to design a transonic axial compressor rotor with splitter blades. This rotor is referred to as the TPL Axial Splittered Rotor (TASR). It proceeds in near chronological order and seeks to provide some of the major details involved in the design. The constraints and goals for the TASR are listed in Table 5.

Table 5. TASR design constraints and goals

Parameter	Goal	Constraint
Rotor Input Power	500 kW	Constrained by available TCR drive turbine output power
Outlet Total-to-Inlet Total Pressure Ratio	1.8 : 1	None
Outlet Total-to-Inlet Total Isentropic Efficiency	80%	None
100% rotor speed	27,000 RPM	None
Casing Diameter	287 mm (11.3 in)	Constrained by existing TCR geometry
Number of Passages	12	None

B. AERODYNAMIC DESIGN PROCEDURE

Due to the time and funding constraints of this study, a non-traditional approach to the design process was chosen. A blade tip-down design approach was used. The outputs of the previously described combined Sanger method and shock-loss model were used as the starting inputs for the design process. These served as the starting point for good practice human-in-the-loop design improvement.

Four major designs, referred to as Baseline and Spirals 1–3, were explored during the course of the design process and are listed in Table 6. Several iterations were made within each major design study and performance maps for each design and iteration at 100 percent speed (27,000 RPM) were constructed.

Table 6. TASR design iterations

Design Iteration	Blade Profile	Splitter Blade Chord	Axial Blade Placement (Blade.MasterXShift)	Splitter Blade Passage Placement
Baseline	Baseline	Splitter blade (SB) chord > 50% main blade (MB) chord	0.00	50%
Spiral 1	Improved Baseline	SB chord = 50% MB chord	0.00	45%
Spiral 2	Improved Spiral 1	SB chord = 50% MB chord	-0.50 - +0.01	40%
Spiral 3	Spiral 2	SB chord = 50% MB chord	-0.02	30 – 35%

The baseline design was derived from the outputs of the combined Sanger method and shock-loss model. The Baseline design solid model was inputted to the Fluid Flow (CFX) module and a mesh was created using Mechanical Model in ANSYS Workbench. The mesh statistics are listed in Table 7. This mesh was used for evaluation of all designs and iterations. The ANSYS Workbench Solver settings used are listed in Table 7.

Table 7. ANSYS Workbench mesh statistics for aerodynamic design

Physics Preference	Advanced Size Function	Sizing: Relevance Center	Sizing: Curvature Normal Angle	Blade Inflation Layers	Blade Inflation Layer Thickness	Nodes	Elements
Mech	Proximity & Curvature	Medium	18°	9	2.00E-03 m	2,941,086	1,813,731

Table 8. ANSYS Workbench solver settings for aerodynamic design

Fluid Model: Turbulence Model	Fluid Model: Transitional Turbulence	Solver Control: Timescale Control	Solver Control: Timescale Factor	Solver Control: Advanced Options	Expert Parameters: Max Continuity Loops	Expert Parameters: Physical Models: tef numerics option
k-epsilon	N/A	Auto	1.0	GDMC, CC, HSN	3	Checked (1)

The numerically derived total-to-total pressure ratio versus mass flow rate performance map is shown in Figure 20. At 100 percent design speed the predicted peak total-to-total peak pressure ratio was 1.65. The numerically derived total-to-total isentropic efficiency versus mass flow rate performance map is shown in Figure 21. At 100 percent design speed the predicted peak efficiency was 84.9 percent. Those results did not meet the TASR pressure ratio goal outlined in Table 5. Additionally, it was decided that the splitter blade’s chord was too long and it resembled a main blade. To ensure the design adhered to the SB concept developed by Wennerstrom [2] a new design constraint was implemented: the SB chord was limited to 50 percent or less of the MB chord.

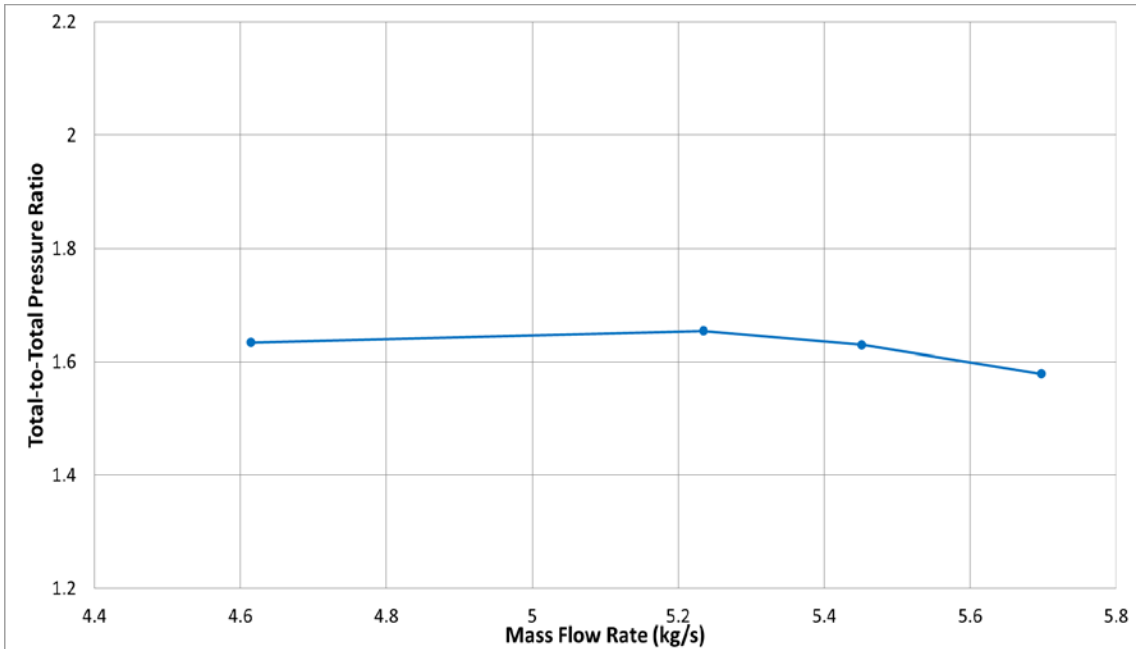


Figure 20. TASR baseline: Numerically derived total-to-total pressure ratio map

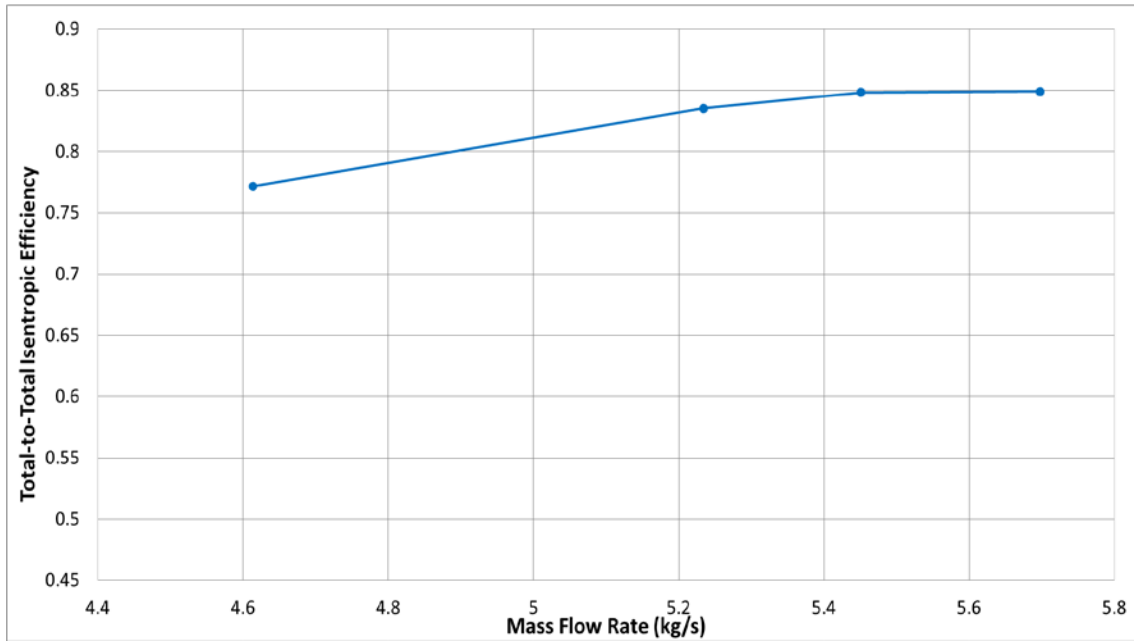


Figure 21. TASR baseline: Numerically derived isentropic efficiency map

The Spiral 1 design implemented the new, self-imposed SB chord design constraint. To counteract the reduction in solidity caused by the shorter SB chord both the MB and SB chords were adjusted, the SB was moved from 50 percent circumferential

passage placement (location between the pressure side (PS) and suction side (SS) of the two adjacent MBs) to 45 percent, and both blade profiles were improved. Iterations examined the performance impacts of increased chord lengths on both blades, forward sweep on the MB, and thinner MB and SB. At 100 percent design speed the predicted peak total-to-total pressure ratio was 1.70 and the predicted peak total-to-total isentropic efficiency was 87.7 percent. These performance results also did not meet the TASR pressure ratio design goal outlined in Table 5 and the mass flow rate range was narrower than desired and intuition indicated performance improvements could be achieved by further blade geometry manipulation. The numerically derived total-to-total pressure ratio versus mass flow rate performance map is shown in Figure 22. The numerically derived total-to-total isentropic efficiency versus mass flow rate performance map is shown in Figure 23.

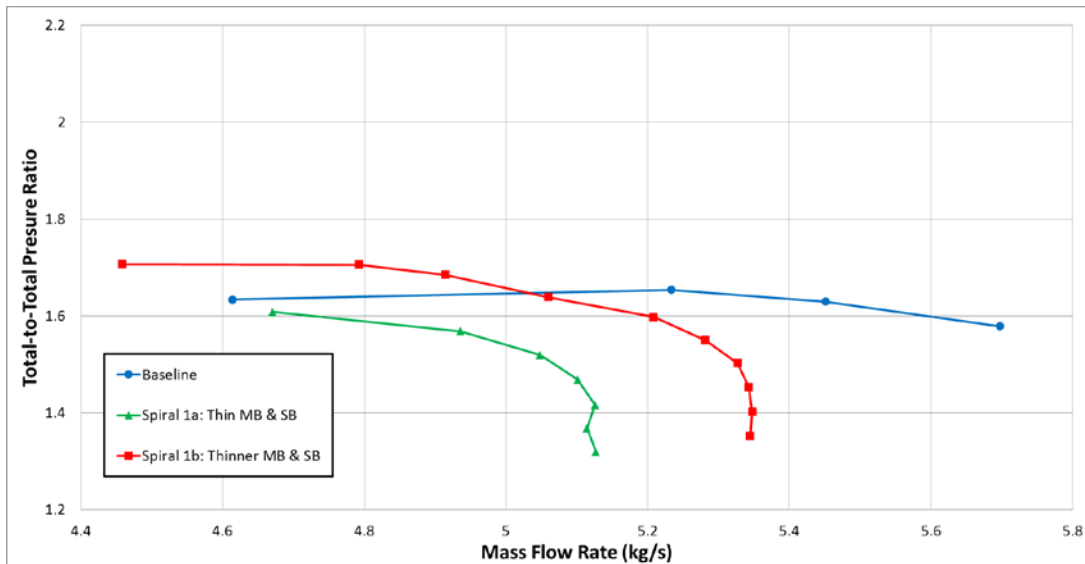


Figure 22. TASR spiral 1: Numerically derived total-to-total pressure ratio map

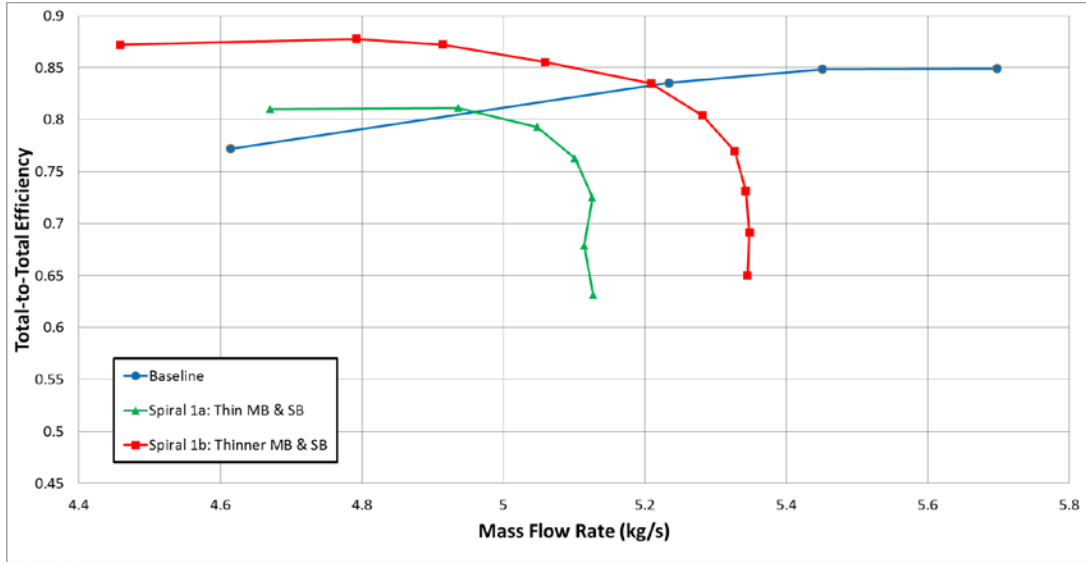


Figure 23. TASR spiral 1: Numerically derived isentropic efficiency map

The Spiral 2 design improved upon the Spiral 1 blade profile, retained the SB chord restriction, shifted the SB radial placement to 40 percent, and explored the performance impacts of moving the MB and SB axially forward and aft along the hub using the MATLAB script `HardCodeBlade` input parameter `Blade.MasterXShift` previously described in Table 2. Varying performance resulted from moving the blades forward and aft. The Spiral 2b design predicted peak total-to-total pressure ratio was 1.83 and the predicted peak total-to-total peak isentropic efficiency was 86.9 percent meeting the design goals of 1.8 and 80 percent respectively; however, the mass flow rate range was still too narrow. The numerically derived total-to-total pressure ratio versus mass flow rate performance map is shown in Figure 24. The numerically derived total-to-total isentropic efficiency versus mass flow rate performance map is shown in Figure 25.

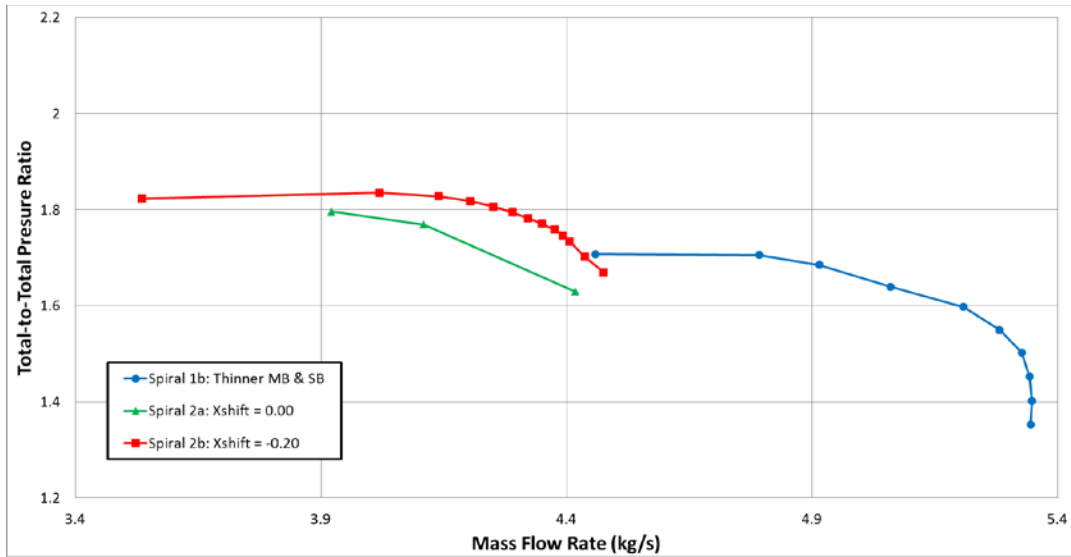


Figure 24. TASR spiral 2: Numerically derived total-to-total pressure ratio map

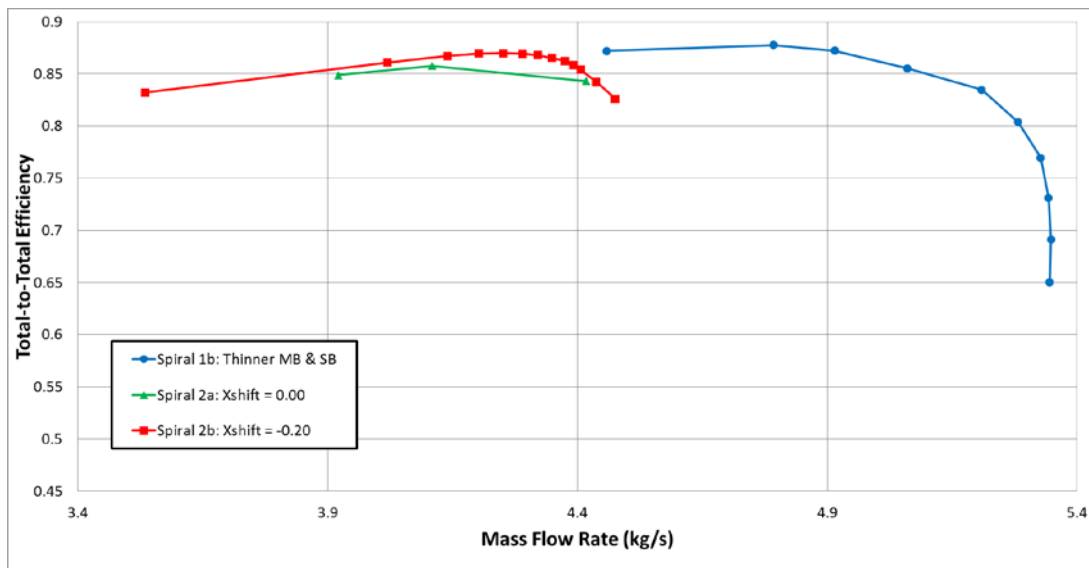


Figure 25. TASR spiral 2: Numerically derived isentropic efficiency map

The results of this axial blade placement study showed that with Blade.MasterXShift = -0.02 (forward) the rotor produced the best results.

The Spiral 3 design froze the geometry of the Spiral 2b design and concentrated on exploring the performance impacts of moving the SB radially in the passage. Varying performance resulted from moving the SB radially between the adjacent MBs. The numerically derived total-to-total pressure ratio versus mass flow rate performance map

is shown in Figure 26. The numerically derived total-to-total isentropic efficiency versus mass flow rate performance map is shown in Figure 27. The results of this SB radial placement study showed that with SB place at 35 percent passage the rotor produced the best results. For this configuration, the predicted peak total-to-total pressure ratio was 2.12 and the predicted peak total-to-total isentropic efficiency was 85.3 percent. The mass flow rate range, Equation (22), was 23 percent.

$$\text{Mass-Flow-Rate-Range} = \frac{\dot{m}_{\max} - \dot{m}_{\min}}{\dot{m}_{\max}} \quad (22)$$

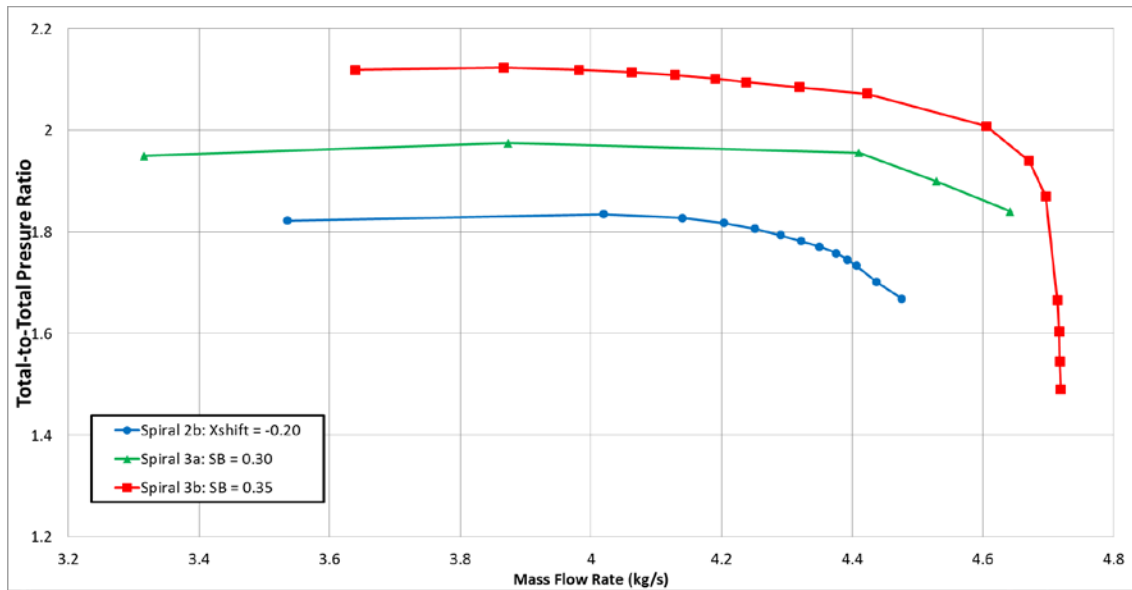


Figure 26. TASR spiral 3: Numerically derived total-to-total pressure ratio map

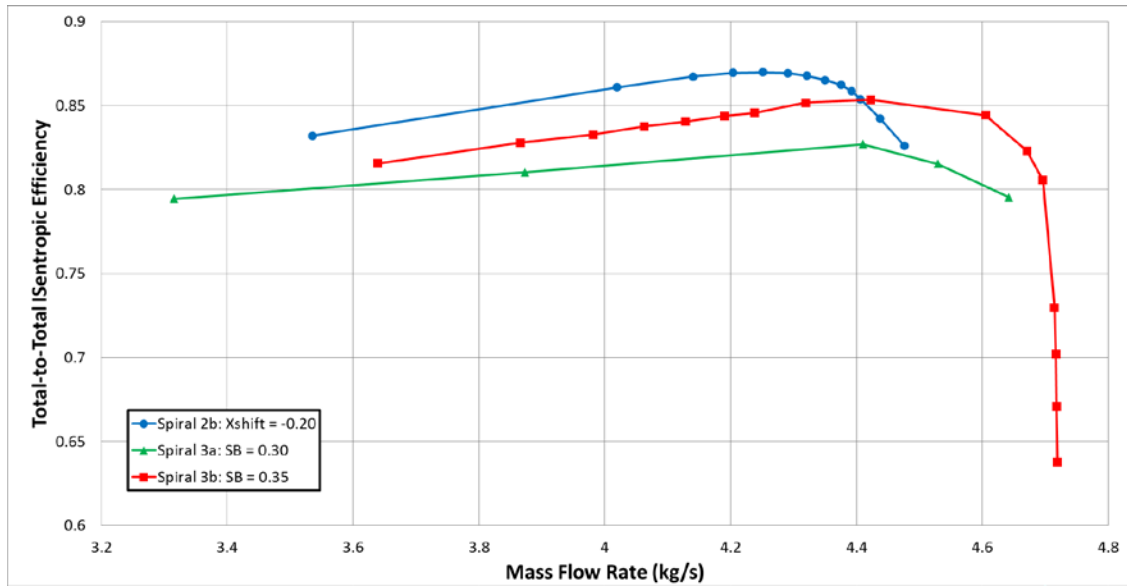


Figure 27. TASR spiral 3: Numerically derived isentropic efficiency map

C. STRUCTURAL ANALYSIS

Structural analysis was performed using the Static Structural module of ANSYS Workbench. Material properties for 7075-T6 aluminum alloy were selected to initiate the Static Structural module. The SolidWorks solid model file BladeHub_Full listed in Table 3 was used as the starting point for generation of a geometry file for input to the Static Structural module. This model incorporated the TASR Spiral 3b geometry. The BladeHub_Full solid model is shown in Figure 28.

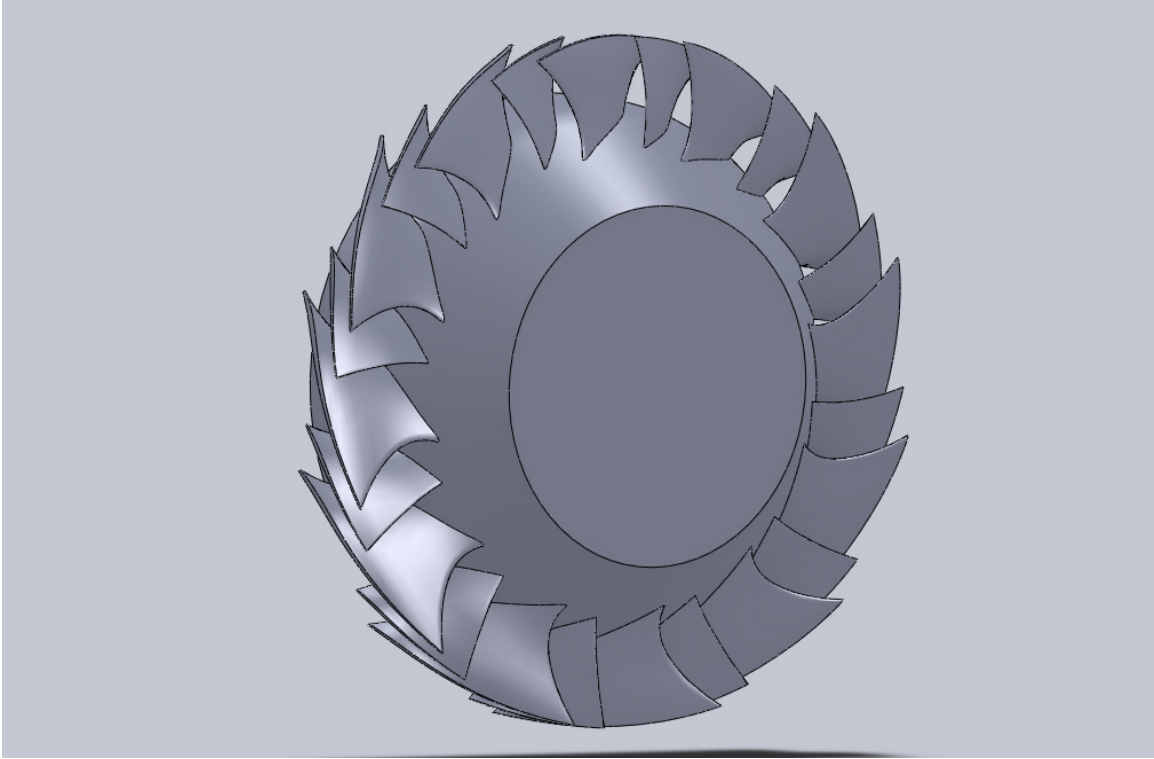


Figure 28. TASR spiral 3b BladeHub_Full solid model

The BladeHub_Full solid model center hub region was then modified to accurately represent the holes required to mount the blisk to the intermediate hub and TCR driveshaft and the minor hub modifications required to mount the nose cone. The modified solid model is shown in Figure 29.

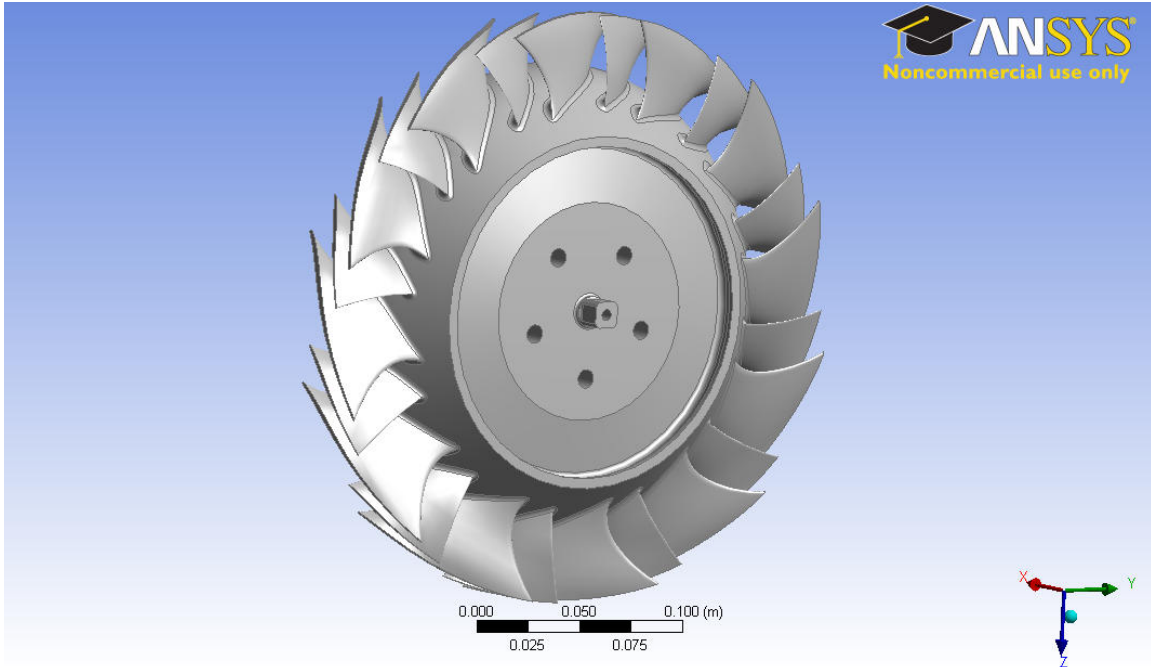


Figure 29. TASR Spiral 3b structural analysis solid model

With the TASR structural analysis solid model inputted to Static Structural module a mesh was created using Mechanical Model in ANSYS Workbench. A medium physical mesh was used. Mesh statistics are listed in Table 9.

Table 9. ANSYS Workbench mesh statistics for structural and modal analysis

Physics Preference	Sizing Relevance Center	Advanced Size Function	Nodes	Elements
Mechanical	Medium	Proximity and Curvature	2,941,086	1,813,731

The meshed TASR 3b structural analysis solid model is show in Figure 30.

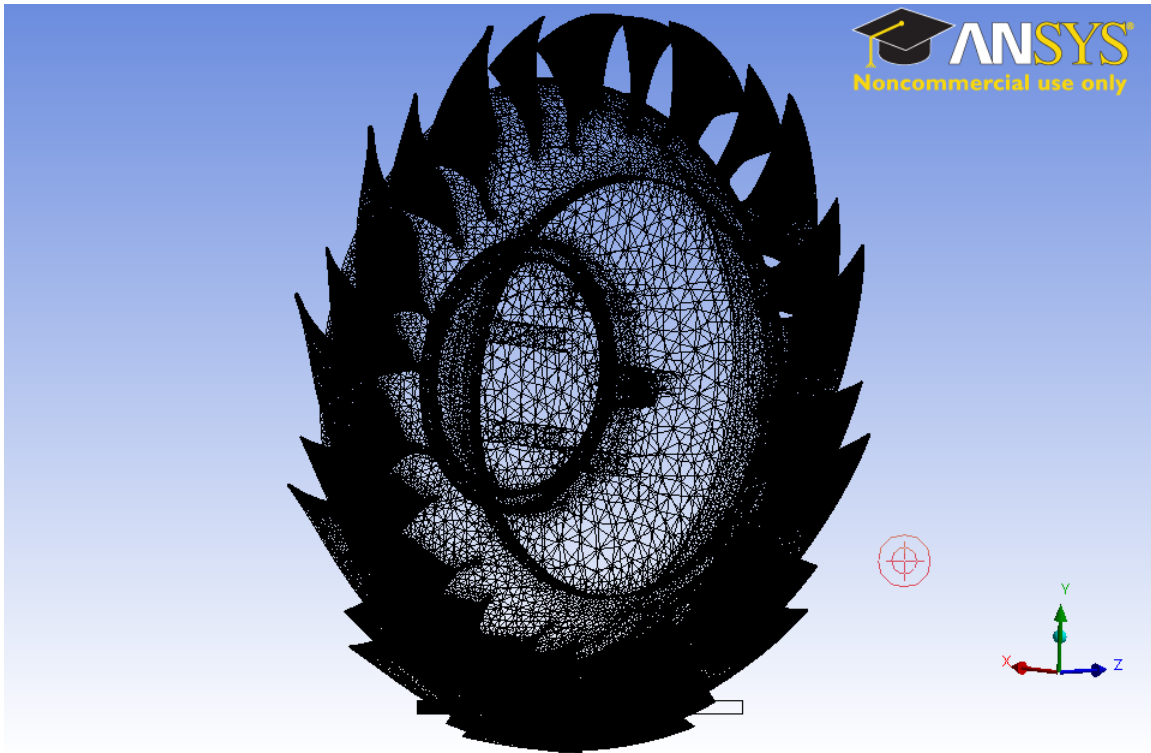


Figure 30. Mesh used for structural and modal analysis

To perform the structural analysis radial and axial constraints were applied and a 30,000 RPM rotational velocity was applied. The design 100 percent rotor speed was 27,000 RPM but performing the structural analysis at 30,000 RPM ensured structural integrity would be maintained during over speed conditions that may be experienced during stall events when conducting experimental testing. Equivalent stress, total deformation, directional deformations, and factor-of-safety were determined.

The first structural analysis run determined a high equivalent stress of 334.8 MPa existed on the rear face of the blisk in the five intermediate hub bolt holes as show in Figure 31.

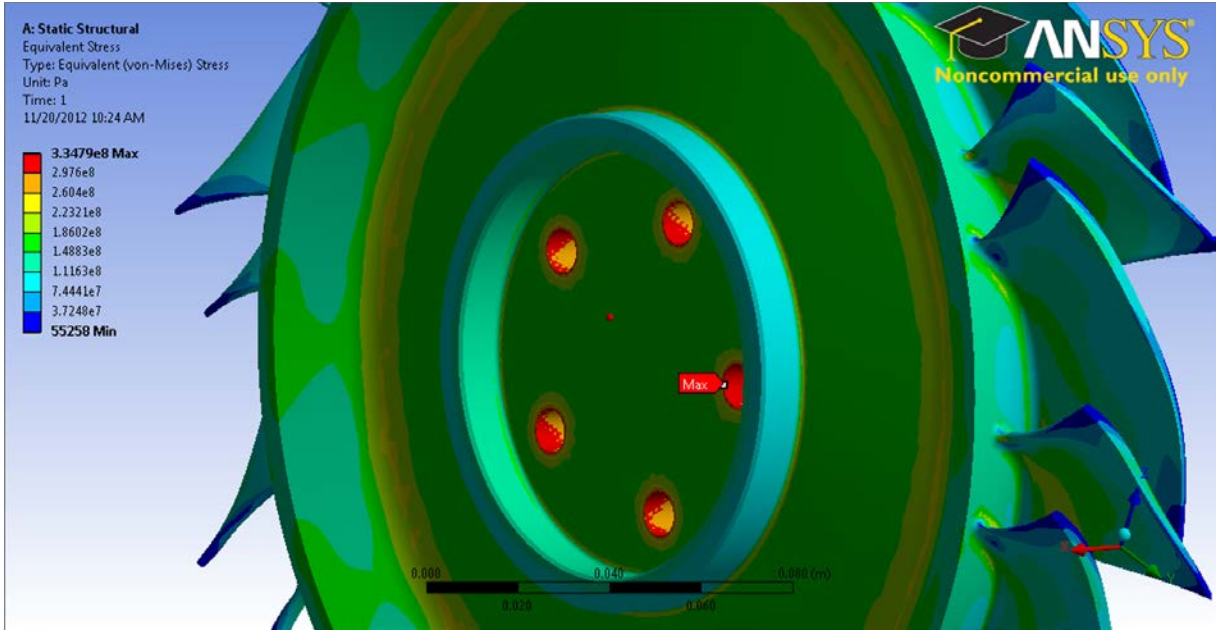


Figure 31. High equivalent stress in TASR intermediate hub bolt holes

Based on a 503 MPa tensile yield strength for 7075-T6 aluminum alloy, the blisk was axially thickened from a 35.56 mm (1.4”) center thickness to a 40.64 mm (1.6”) center thickness. The subsequent structural analysis run determined a significant reduction in this area of concern, but determined there was a new area of high stress of 359.7 MPa in the center of the nose cone mount bolt hole as show in Figure 32.

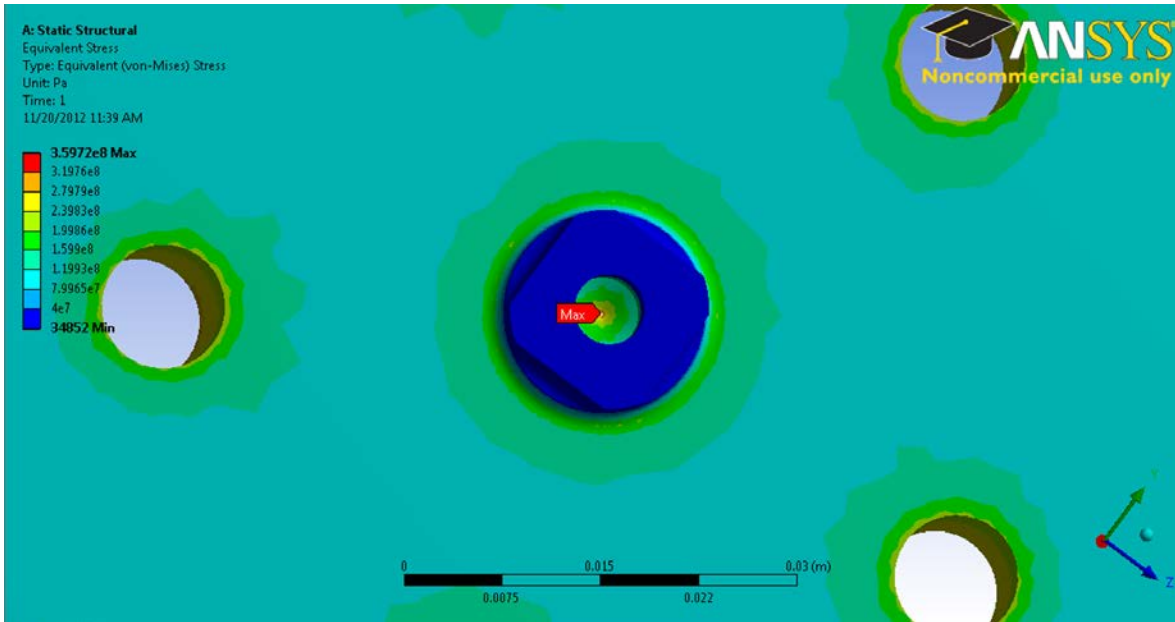


Figure 32. High equivalent stress in TASR nose cone mount bolt hole

To reduce this stress, the nose cone mounting was axially extended from 6.35 mm (0.25”) to 15.24 mm (0.60”). The subsequent run determined this area of concern had been eliminated but a high stress area of 291.1 MPa had returned to the five intermediate hub mounting holes. Once again the blisk was axially thickened from a 40.64 mm (1.6”) center thickness to a 45.72 mm (1.8”) center thickness. The following run determined this geometry change was successful in eliminating this stress concentration but found a new area of concern at the main blade trailing edge and hub intersection. Equivalent stresses in this area were determined to exceed 503 MPa, the tensile yield strength of the 7075-T6 aluminum alloy. Some small blade geometry changes were required to reduce the equivalent stress in this area to acceptable levels. Two different versions of blade geometry changes were examined. The highlights of those two versions are shown in Table 10.

Table 10. Structural analysis blade geometry modifications

Structural Analysis Modification	MB Chord	SB Chord	MB Leading Edge	SB Leading Edge	MB Stagger	MB Thickness	SB Thickness	Maximum Equivalent Stress
1	12.7 mm (0.5") longer at hub	NA	Slightly thicker at hub and midspan	Slightly thicker at hub and midspan	Small increase at TE near hub & midspan	Thinner at 70% chord near tip	NA	325.6 Mpa
2	25.4 mm (1.0") longer at hub	12.7 mm (0.5") longer at hub	Hub: Doubled thickness Midspan: Slightly thicker	Hub: Doubled thickness Midspan: Slightly thicker	Larger increase at TE near hub & midspan	Thicker at 30% chord near hub Thinner at 70% chord near tip	Thicker at 30% chord at midspan Thicker at 30% chord near tip	270 Mpa

Structural analysis modification 1 reduced equivalent stress at the main blade trailing edge and hub intersection to 325.6 MPa as show in Figure 33.

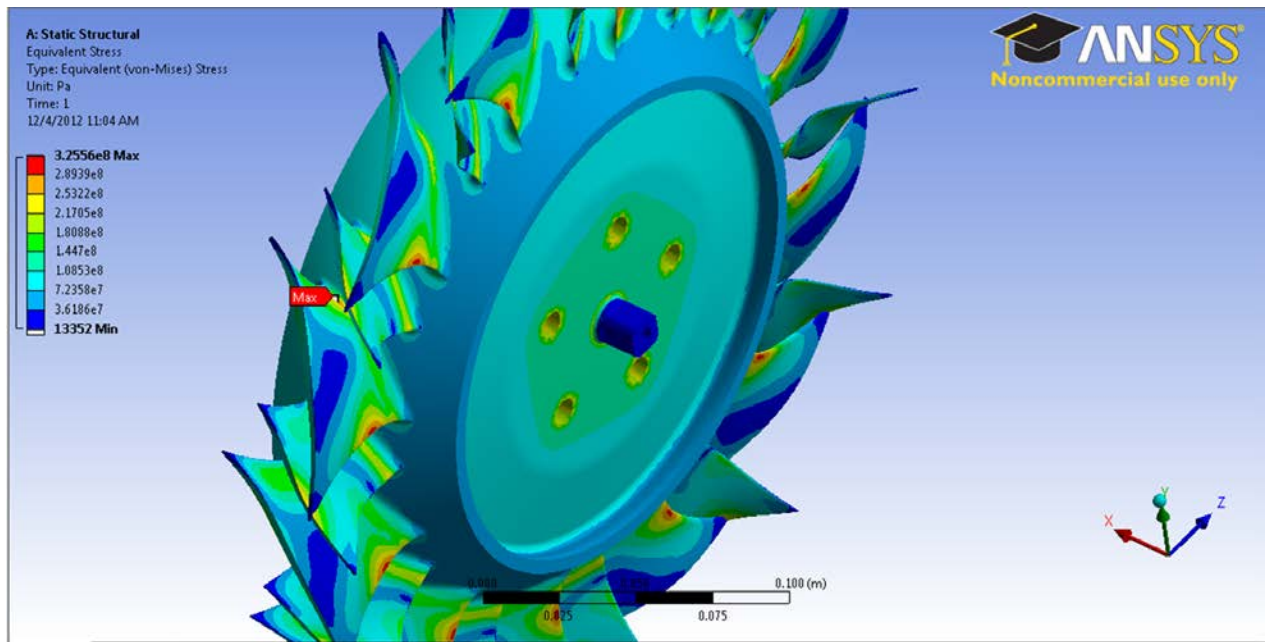


Figure 33. Structural analysis modification 1 equivalent stress

Structural analysis modification 2 reduced equivalent stress at the main blade trailing edge and hub intersection further to 270 MPa as show in Figure 34.

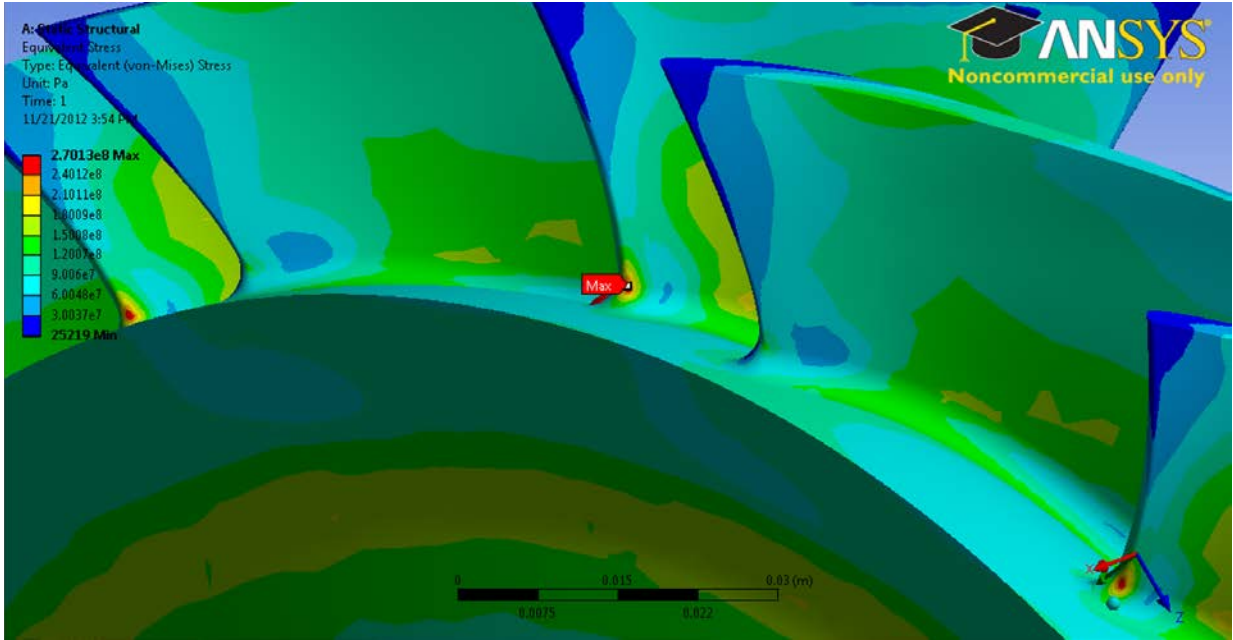


Figure 34. Stress analysis modification 2 equivalent stress

Performance maps for both stress analysis modifications at 100 percent speed (27,000 RPM) were constructed. The numerically derived total-to-total pressure ratio versus mass flow rate performance map for both is shown in Figure 35. The numerically derived total-to-total isentropic efficiency versus mass flow rate performance map is shown in Figure 36.

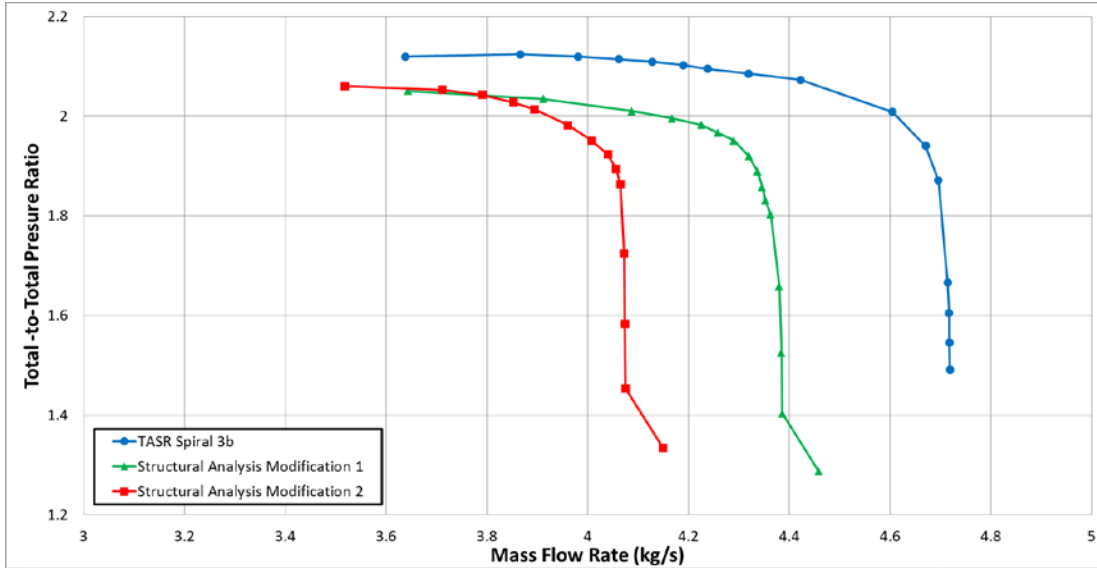


Figure 35. Structural analysis: Numerically derived total-to-total pressure ratio map

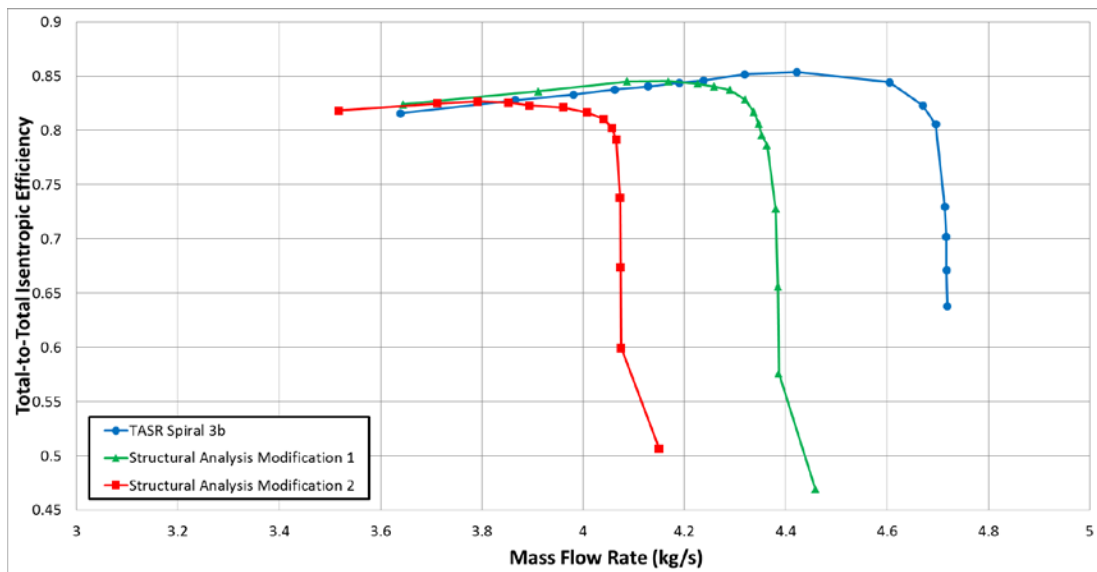


Figure 36. Structural analysis: Numerically derived isentropic efficiency map

Although, the equivalent stress reduction was better with structural analysis modification 2, 1 was chosen as the final design since its performance more closely matched the TASR spiral 3b performance while still reducing equivalent stress to acceptable levels. The pressure ratio decreased to 2.05 and the efficiency dropped to 84.5 percent while the predicted mass flow range was 18.2 percent

The structural changes compromised the aero/thermo performance by reducing the total-to-total pressure ratio to 2.05, the isentropic efficiency to 84.5 percent, and the mass flow rate range to 18 percent.

D. MODAL ANALYSIS

With a completed analysis of the structural stresses for the TASR blisk at 30,000 RPM the Static Structural module was rerun at 27,000 RPM (100 percent rotor speed). A modal analysis was created by transferring the results of the 27,000 RPM structural analysis to the Modal module in ANSYS Workbench shown in Figure 37.

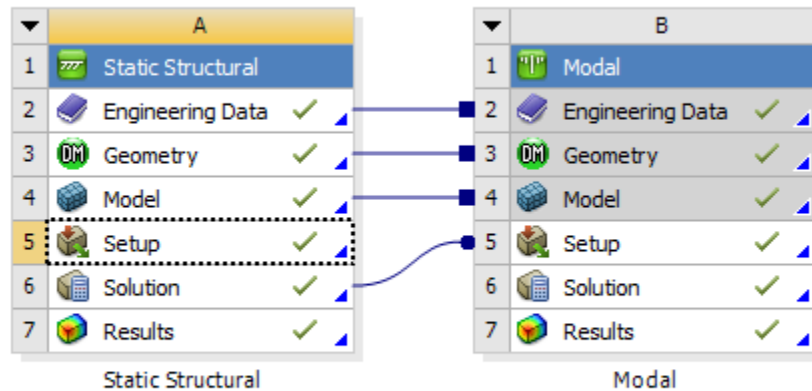


Figure 37. ANSYS Workbench project for static structural and modal analysis

The connecting lines indicated the transfer of engineering, geometric, mesh, and solution data from the static structural module to the setup portion of the modal module. No further setup was required to perform the modal analysis. The solver in the modal module was used to determine the first 30 modal frequencies for the design 100 percent rotor speed (27,000 RPM).

Modal analyses were then performed for rotational velocities at 0 percent, 50 percent, and 75 percent design speed. Because the modal analysis described above was conducted for the entire TASR blisk and across the entire range of speeds, the results were sufficient to generate a Campbell diagram. The TASR Campbell diagram is shown in Figure 38.

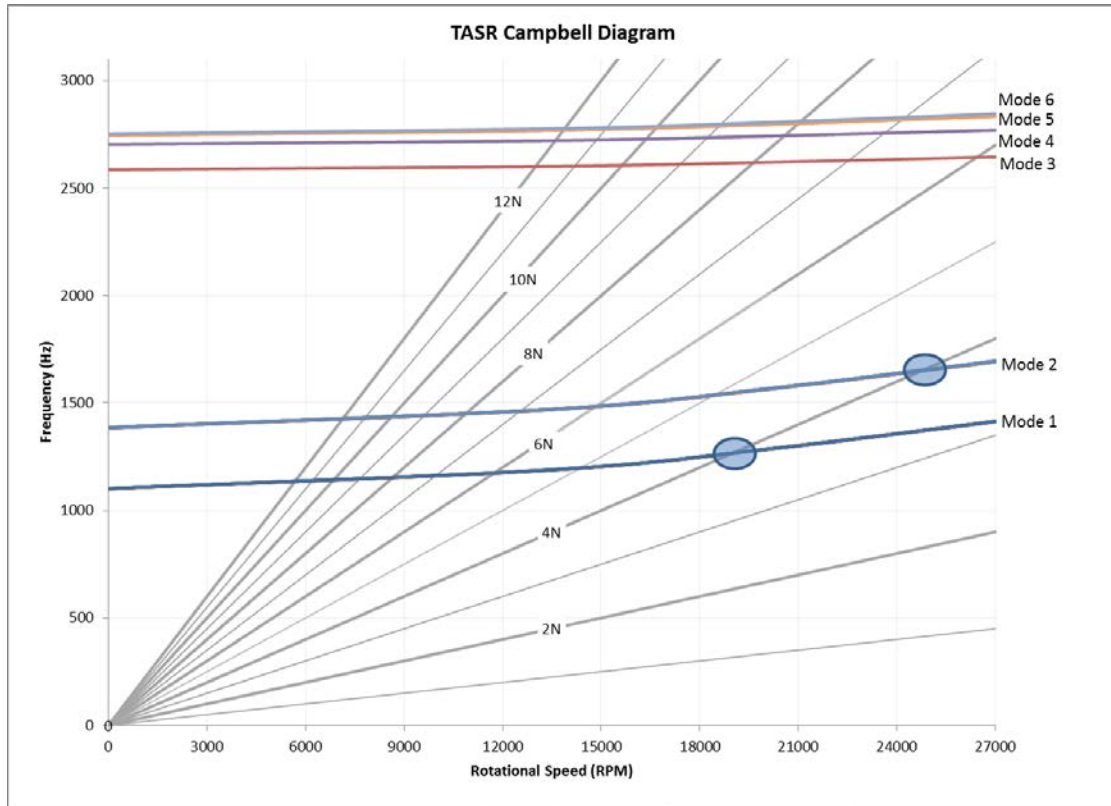


Figure 38. TASR Campbell diagram

E. RESULTS

The design phase of this study produced the following results:

- A new novel design procedure has been developed and documented that uses commercial-off-the-shelf software for the geometric rendering and analysis of a transonic compressor rotor.
- MATLAB was used to script the whole design procedure by performing a preliminary tip section design, defining blade parameters, and controlling both SolidWorks and ANSYS-CFX.

- During a design cycle a complete constant speedline of the compressor was analyzed from open throttle (choke) to stall conditions. This allowed overall performance to be evaluated and compared during each cycle.
- After restacking of the blade profiles and including fillet radii at the blade roots the design was frozen. A solid blisk (blade and disk) was machined out of 7075-T6 aluminum alloy, which is shown in Figure 39.



Figure 39. Final machined TASR blisk

IV. DETAILED ANALYSIS

A. BLADE TIP GAP INCORPORATION

Utilizing the TASR structural analysis modification 1 geometry (from here on this rotor will be referred to simply as the TASR), which produced satisfactory stress reduction but retained the best overall performance, the SolidWorks model was modified to incorporate a tip gap (TG) between the rotor and the casing. An integral part of the TCR rotor casing is an abradable rubber material in the vicinity of the TG region. The abradable material is designed to be machined away by the blade tips as the blisk deforms and the blade tip grows during rotation. Optimally at design speed the blade tip diameter would grow larger than the inside diameter of the abradable rubber material and the difference in fit would be accommodated by the removal of abradable rubber by the spinning compressor blades. However, early tests revealed that the thin 7075-T6 aluminum blade tips were not strong enough to abrade the material at operating speeds. Additionally, while using a model with no TG would have been acceptable for modeling the first run at design speed it would not accurately reflect the TG condition for subsequent runs after abradable material is removed.

The ANSYS Static Structural module was used to analyze the TASR geometry for radial deformation at design speed and resulted in a maximum radial deformation of 0.33 mm (0.013 in) on the SB tips as show in Figure 40. Due to the demonstrated incompatibility of the thin aluminum blade tips and the abradable material, the abradable material in the TCR casing was machined for a cold-shape TG of 0.91 mm (0.036 in). This would allow for a 0.56 mm (0.022 in) TG at design speed and also accommodate the additional blade tip deformation experienced during over-speed conditions caused by stall at design speed. Based on past experience, a 10 percent over-speed was expected during stall causing rotor speed to increase to approximately 30,000 RPM. At 30,000 RPM the SB tips would continue to deform to 0.41 mm (0.016 in) reducing the TG to 0.51 mm (0.020 in).

For the purpose of compressor mapping using ANSYS CFX, the TASR SolidWorks model was modified to incorporate a 0.25 mm (0.010 in) TG to model the anticipated TGs ranging from 0.91 mm (0.036 in) at 0 RPM to 0.50 mm (0.019 in) at 30,000 RPM during stall at design speed.

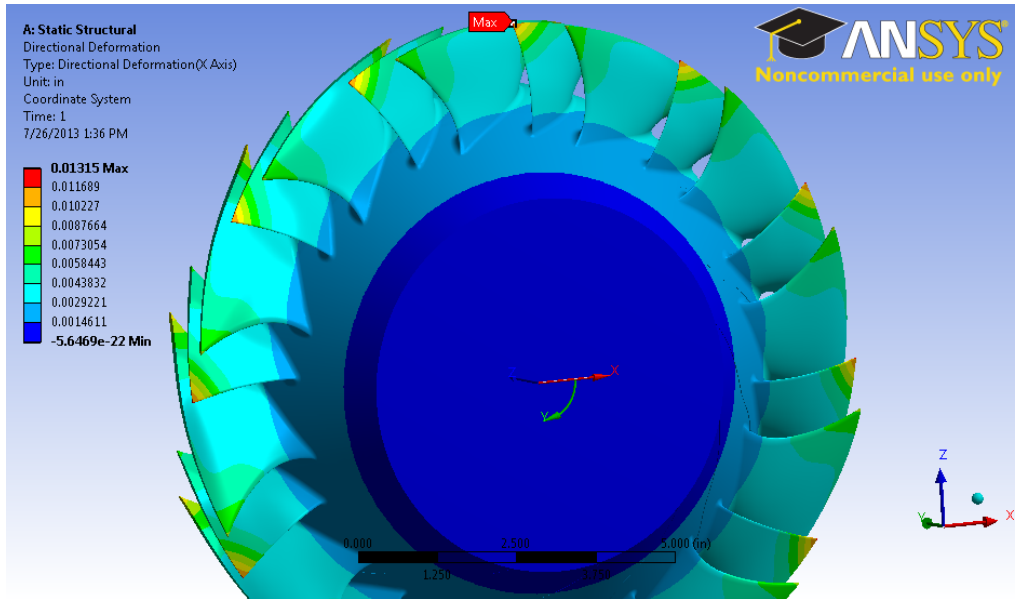


Figure 40. TASR radial deformation

B. STEADY STATE COMPRESSOR MAPPING USING ANSYS CFX

Computational fluid dynamics (CFD) was performed for the TASR using the ANSYS Workbench 14.0 CFX module. Modeling was completed for 70 percent (18,900 RPM), 80 percent (21,600 RPM), 90 percent (24,300 RPM), 95 percent (25,650 RPM), and 100 percent (27,000 RPM) speeds for the purpose of comparison against the TCR experimental results.

The CFX analysis began by importing the gas path obtained from TASR SolidWorks model with the 0.25 mm (0.010 in) TG incorporated. Using the meshing tool within ANSYS Workbench, the gas path was meshed. Match control was assigned to all regions of the periodic gas path faces to ensure that the meshes would be identical between the right and left periodic gas path faces. A “Curvature Normal Angle” of 8° was used to ensure a sufficiently fine mesh in the highly curved surfaces. The number of

cells across the gap was specified to be 25 to ensure accurate modeling of the TG region. Additionally, 25 inflation layers with a maximum thickness of 1 mm were specified for both the MB and SB to ensure accurate modeling of the boundary layers around the blades. The mesh statistics are shown in Table 11. The average dimensionless distance from the wall (y^+), as defined by equation (23) from White [11], for the entire mesh was 22. The average (y^+) for the blade tip regions was seven. The gas path with the resultant very fine mesh is shown in Figure 41.

$$y^+ = \frac{u^* y}{\nu} \quad (23)$$

Where u^* is the friction velocity, y is the distance from the wall, and ν the dynamic viscosity.

Table 11. ANSYS Workbench mesh statistics for compressor mapping

Physics Preference	Advanced Size Function	Sizing: Relevance Center	Sizing: Curvature Normal Angle	Blade Inflation Layers	Blade Inflation Layer Thickness	Nodes	Elements
Mech	Proximity & Curvature	Fine	8	25	1.00E-03 m	7,602,119	31,425,581

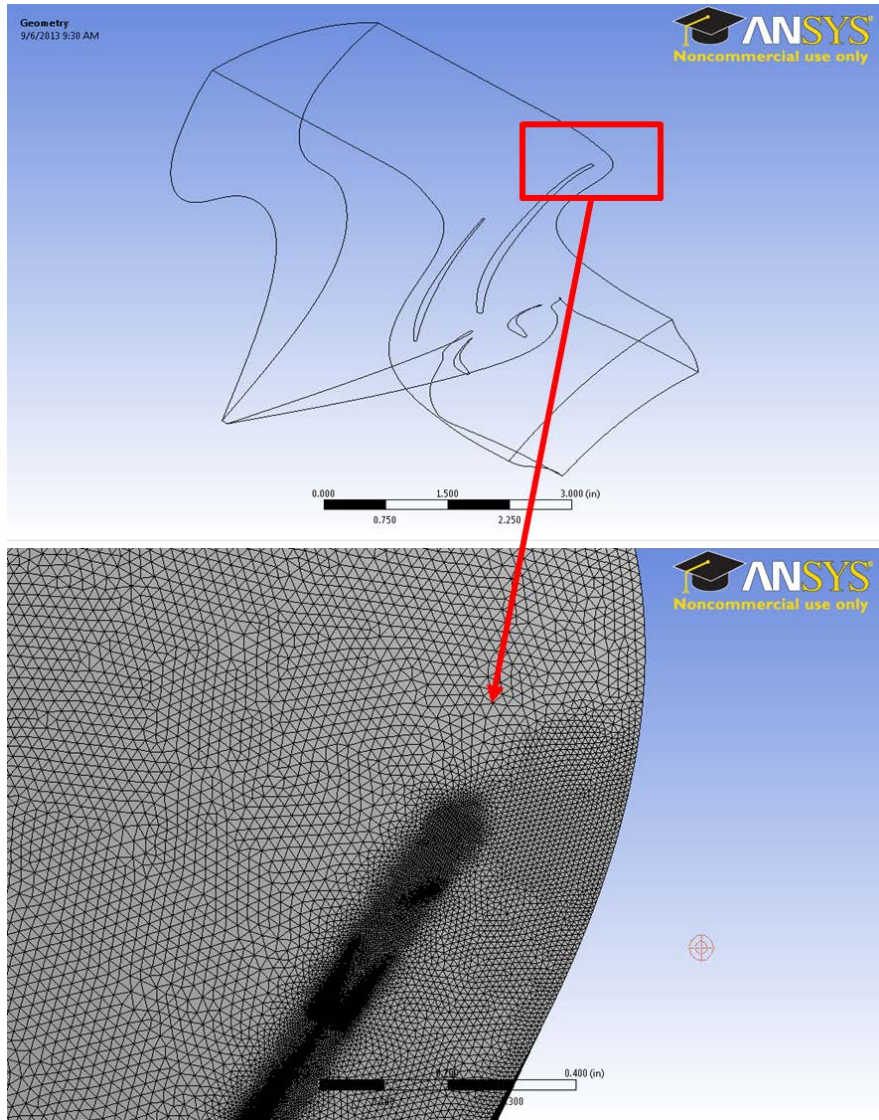


Figure 41. TASR gas path final mesh used for compressor mapping

CFX-Pre in ANSYS Workbench was used to apply the boundary conditions. A steady state analysis was conducted with the default domain specified as rotating with rotational velocity specified for the speed of interest. The casing was derotated at the opposite speed so as allow for tip leakage simulation. The reference pressure was specified to be one atmosphere. The outlet static pressure was incremented as required to map the TASR's performance at each speed of interest. The solver settings used are shown in Table 12.

Table 12. ANSYS Workbench solver settings for compressor mapping

Fluid Model: Turbulence Model	Fluid Model: Transitional Turbulence	Solver Control: Timescale Control	Solver Control: Timescale Factor	Solver Control: Advanced Options	Expert Parameters: Max Continuity Loops	Expert Parameters: Physical Models: tef numerics option
SST	Gamma Theta	Auto	0.5	GDMC, CC, HSN	3	Checked (1)

The ANSYS CFX simulations resulted in the following steady-state compressor maps. The numerically derived total-to-total pressure ratio versus mass flow rate compressor maps for 100 percent design speed with and without a TG are shown in Figure 42. The numerically derived total-to-total isentropic efficiency versus mass flow rate compressor maps for 100 percent design speed with and without a TG are shown in Figure 43.

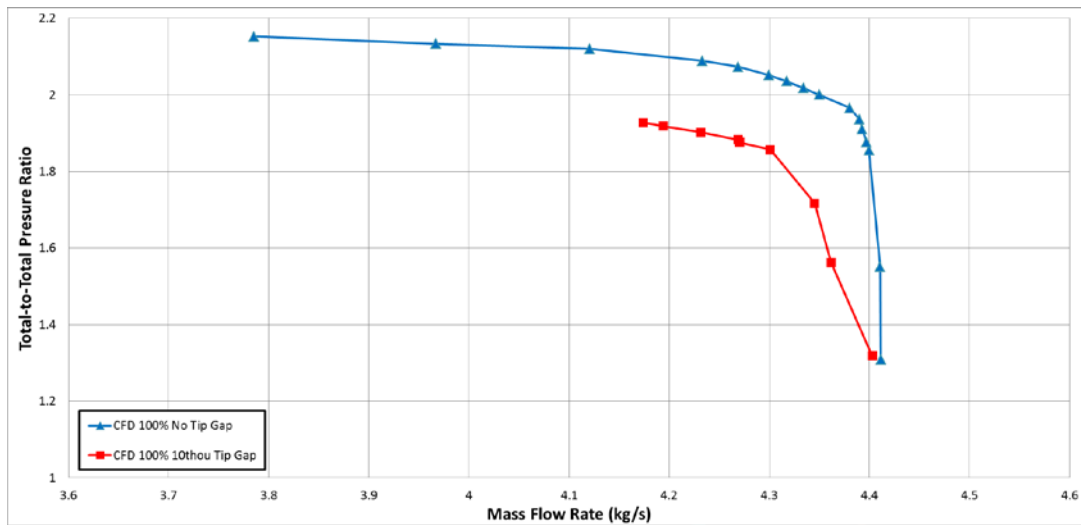


Figure 42. TASR 100 percent design speed numerically derived total-to total pressure ratio map

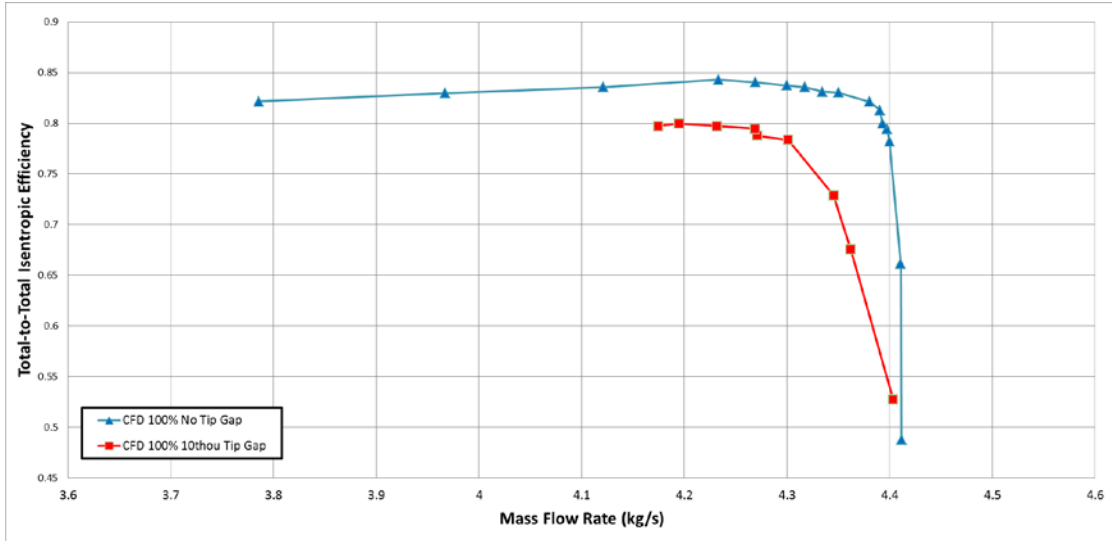


Figure 43. TASR 100 percent design speed numerically derived isentropic efficiency map

Incorporating a 0.25 mm (0.010 in) TG reduced the predicted total-to-total pressure ratio 11 percent to 1.92, the predicted total-to-total isentropic efficiency 5 percent to 79.9 percent, and the mass flow range 8 percent to 6 percent. The complete numerically derived total-to-total pressure ratio versus mass flow rate compressor map with TG incorporated is shown in Figure 44. The complete numerically derived total-to-total isentropic efficiency compressor map with TG incorporated is show in Figure 45. The complete numerically derived power vs. mass flow rate compressor map with TG incorporated is shown in Figure 46.

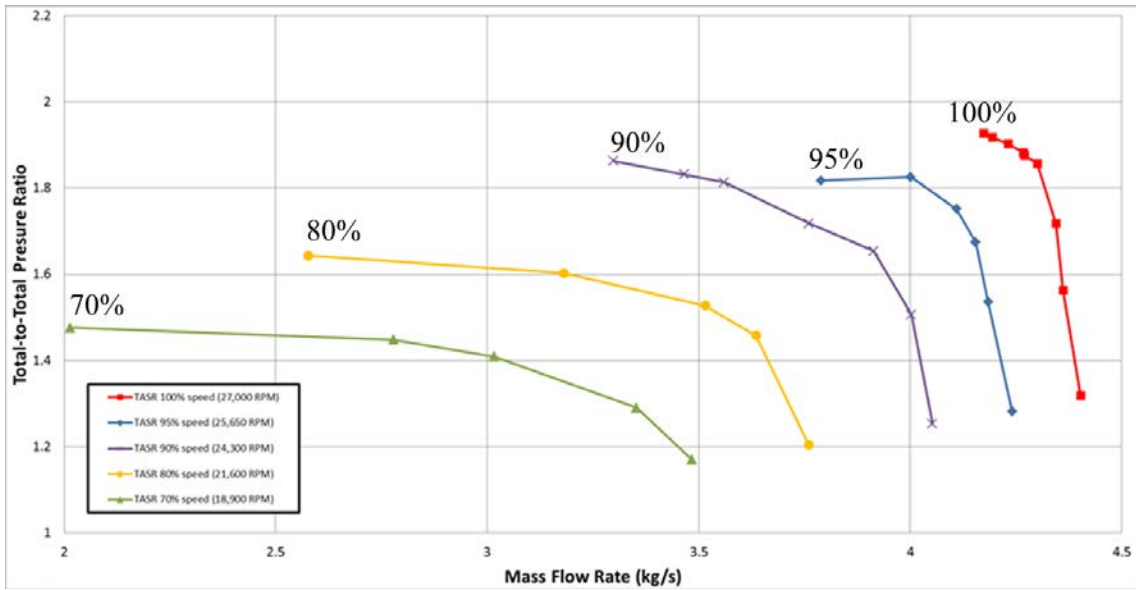


Figure 44. TASR numerically derived total-to-total pressure ratio map

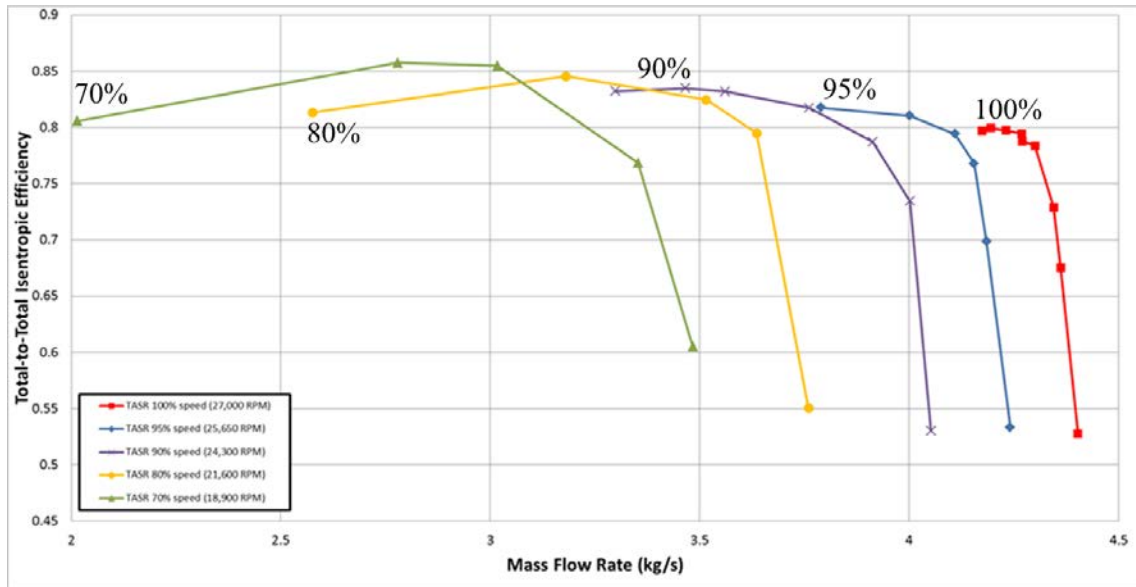


Figure 45. TASR numerically derived isentropic efficiency map

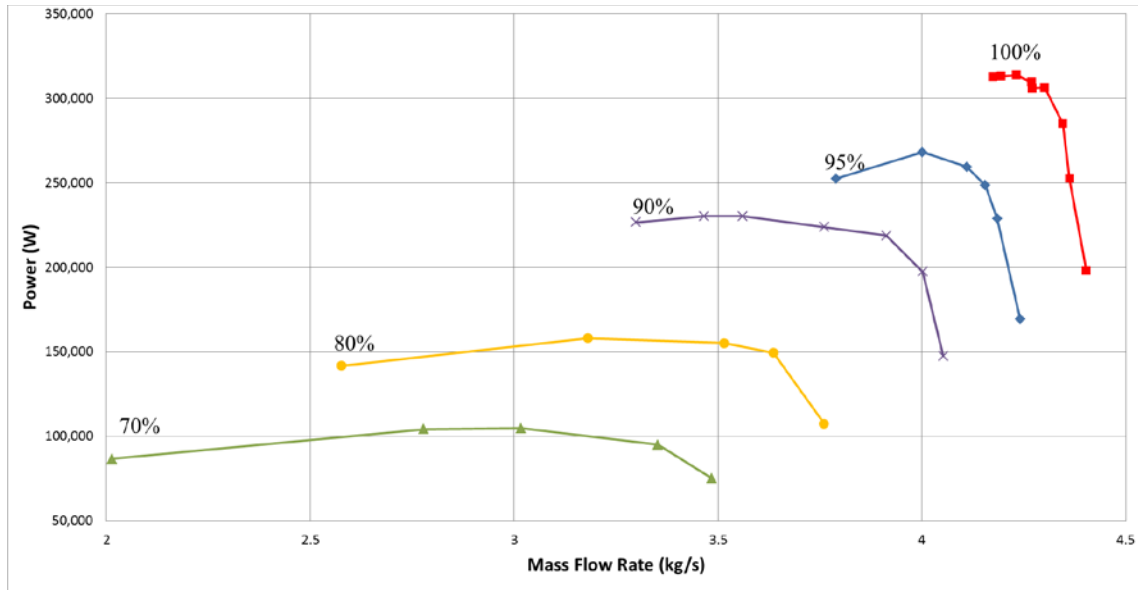


Figure 46. TASR numerically derived power map

V. EXPERIMENTAL FACILITY AND PROCEDURE

The TASR was experimentally tested in the TCR facility at the NPS TPL in a rotor-only configuration. The basic TCR layout was as designed by the original designer, Dr. M. H. Vavra, and as described by McNab [8] with the exception of the modifications required to accommodate the TASR.

This chapter describes the modifications required to install the TASR, the experimental procedures followed for data collection, and the data acquisition and reduction methods.

A. TRANSONIC COMPRESSOR RIG AND INSTALLATION

1. Compressor Installation and Instrumentation

Modifications were made to the rotor-only test section of the TCR to accommodate the TASR as shown schematically in Figure 47. Due to the axially segmented construction of the TCR, the TASR was easily accommodated into the rig by replacing the NPSMF rotor section with a TCR rotor section of identical dimensions with the exception of a wider inner ring of abradable rubber material to accommodate the longer chord of the TASR blades. After assembly the inlet instrumentation was located in axial segment 1 (AS1), the casing transient pressure instrumentation over the rotor were located in axial segment 2 (AS2), and the outlet instrumentation was located in axial segment 3 (AS3). The axial segments are show in Figure 48.

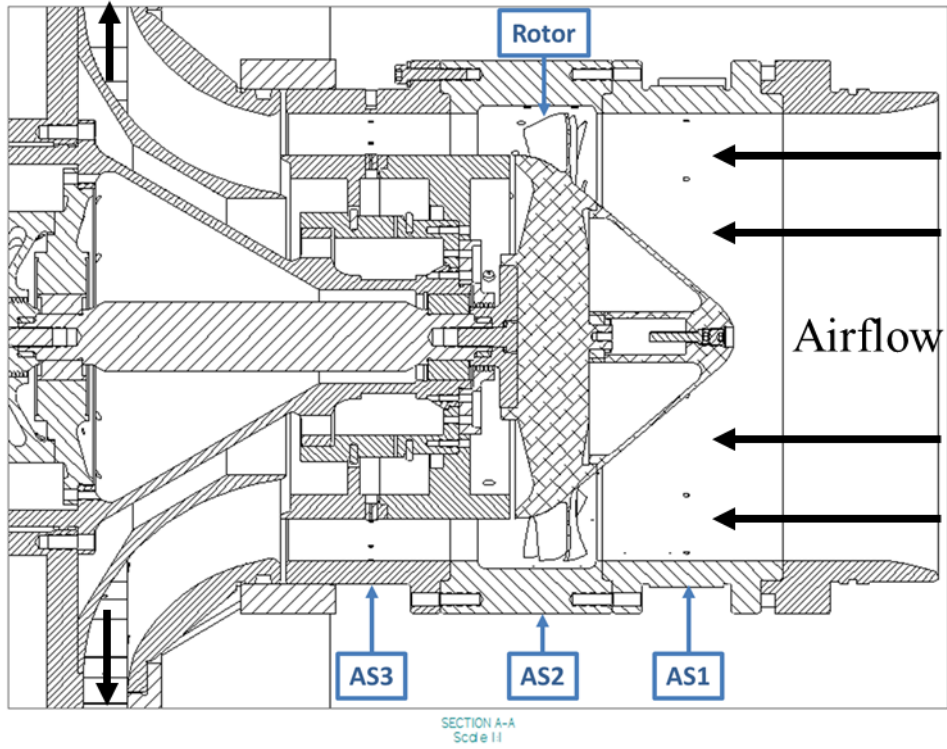


Figure 47. TCR cross-section with the TASR installed

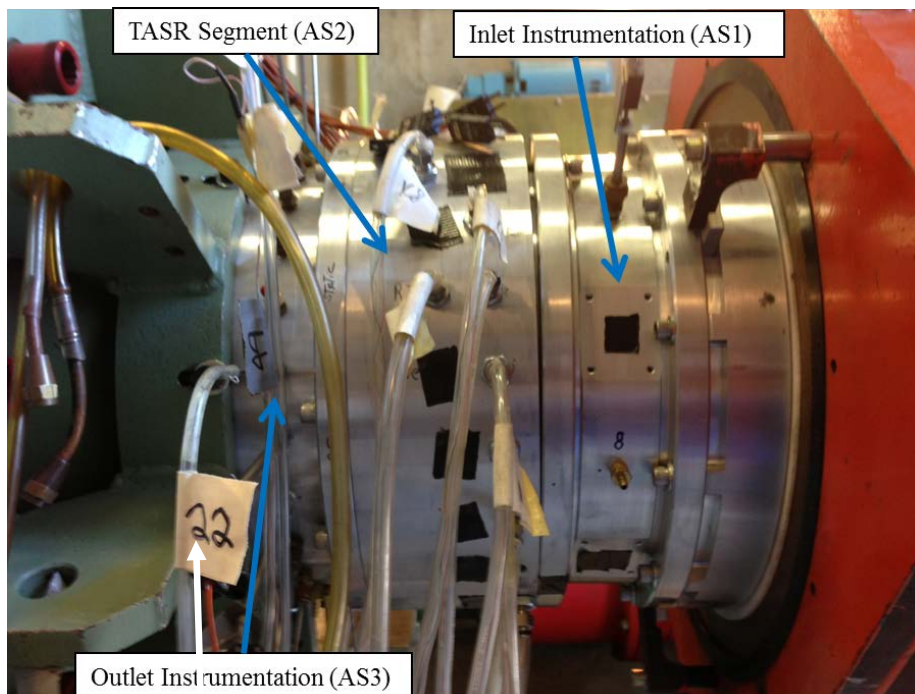


Figure 48. TASR axially segmented casing

2. Measurement Devices

Steady-state measurements were taken using stagnation temperature and stagnation pressure probes in the flow field as well as unsteady static pressure probes in the casing. The steady-state probes used were of the same types as described by McNab [8]. Those were 1/16 inch “miniature head” Kiel probes (United Sensor KAA-8) and 1/8 inch “Standard Head” combination Kiel/thermocouple probes (United Sensor KT-8J-12-C).

3. Instrument Placement

Inlet measurements for this study were taken at AS1 forward of the TASR using two combination Kiel/thermocouple probes and two static pressure ports. Outlet measurements were taken at AS3 using nine combination Kiel/thermocouple probes, 11 Kiel pressure probes, six static pressure ports in the hub, and two outlet static pressure ports in the casing. Two custom temperature probes were installed in AS3 to measure hub and casing temperatures.

In the TASR segment (AS2) eight Kulite Miniature IS Pressure Transducers (XCQ-080 Series) were installed at 15 degree increments around the TASR casing circumference at a range of radial stations in the blade tip regions. This array of Kulite pressure transducers were each sampled at 196 kHz to measure pressure distribution across the blade tips during operation. Additionally, 10 static pressure ports were also installed at 15 degree increments around the casing at a range of radial stations. The Kulite transducer and static pressure port stations are shown in detail in Figure 49. All of the installed instrumentation used during this study is listed in Table 13.

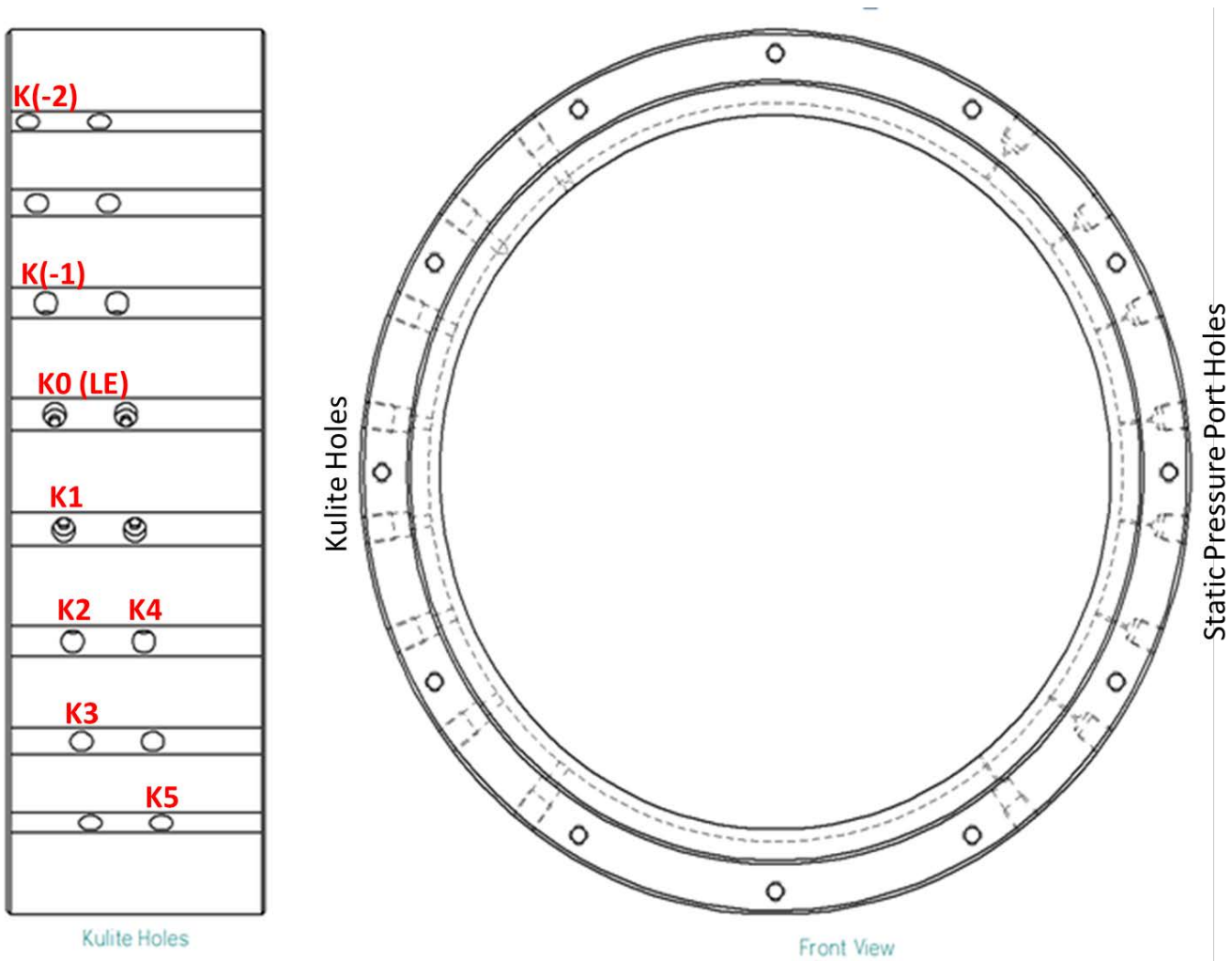


Figure 49. TASR AS2 instrumentation station locations

Table 13. TASR instrumentation

Pressure Port #	Instrument	(P) Depth [in] from casing	(T) Depth [in] from casing	Orientation Angle (deg)
1	Tare			
2	Scale			
3	Flow Nozzle P6			
4	Flow Nozzle Ps			
5	Inlet Pt1 Combo			
6	Inlet Pt1 Combo			
7	Inlet Ps1 (static)			
8	Inlet Ps1 (static)			
9	Outlet Ps3 (static)			
10	Outlet Ps3 (static)			
11	Kiel Probe	0.059		201.6
12	Kiel Probe	0.159		28.8
13	Kiel Probe	0.209		259.2
14	Combo	0.379	0.004	216.0
15	Combo	0.399	0.024	230.4
16	Kiel Probe	0.359		100.8
17	Combo	0.419	0.044	86.4
18	Kiel Probe	0.459		43.2
19	Combo	0.489	0.114	172.8
20	Combo	0.569	0.194	288.0
21	Combo	0.589	0.214	273.6
22	Kiel Probe	0.654		316.8
23	Combo	0.709	0.334	129.6
24	Kiel Probe	0.759		187.2
25	Combo	0.789	0.414	302.4
26	Kiel Probe	0.849		115.2
27	Kiel Probe	0.884		0.0
28	Kiel Probe	0.939		14.4
29	Kiel Probe	0.959		28.8
30	Combo	1.059	0.684	158.4
31	Hub static pressure P2 1	1.059		37.5
32	Hub static pressure P2 2	1.059		
33	Hub static pressure P2 3	1.059		
34	Hub static pressure P2 4	1.059		
35	Hub static pressure P3 1	1.059		
36	Hub static pressure P3 2	1.059		
37	Hub static pressure P3 3	1.059		
39	Casing static pressure	0.000		67.5
40	Casing static pressure	0.000		142.5
41	Casing static pressure	0.000		127.5
42	Casing static pressure	0.000		112.5
43	Casing static pressure	0.000		97.5
44	Casing static pressure	0.000		82.5
45	Casing static pressure	0.000		67.5
46	Casing static pressure	0.000		52.5
47	Casing static pressure	0.000		37.5
48	Casing static pressure	0.000		82.5
49	Custom T-probe (Hub)	1.059		345.6
50	Custom T-probe (Casing)	0.000		144
51	Static Kulite [-2]	0.000		322.5
52	Static Kulite [-1]	0.000		292.5
53	Static Kulite [0] - LE	0.000		277.5
54	Static Kulite [1]	0.000		262.5
55	Static Kulite [2]	0.000		247.5
56	Static Kulite [3]	0.000		232.5
57	Static Kulite [4]	0.000		247.5
58	Static Kulite [5]	0.000		217.5

B. EXPERIMENTAL PROCEDURE

The TCR configuration and operation are described in detail by Grossman [12] and are summarized here. The TASR was powered by two opposed rotor, single stage air-operated drive turbines mounted on a common shaft as shown in Figure 50. The drive turbines received supply air from a 12-stage Allis-Chalmers axial compressor capable of providing 2.2 kg/sec mass flow rate at up to 2 atmospheres gage pressure. The TASR was connected to the drive turbines via a splined quill shaft. An air-operated balance piston was located between the splined quill shaft and the TASR to counteract the axial forces exerted by the TASR during operation and reduce bearing stresses. TASR speed was controlled via an electronically actuated butterfly valve that was used to throttle the air supply to the drive turbines. Airflow to the TASR inlet was controlled using an electromechanical actuated rotating plate throttling valve and settling chamber. Mass flow rate through the TASR was measured by a flow nozzle positioned downstream of the settling chamber.

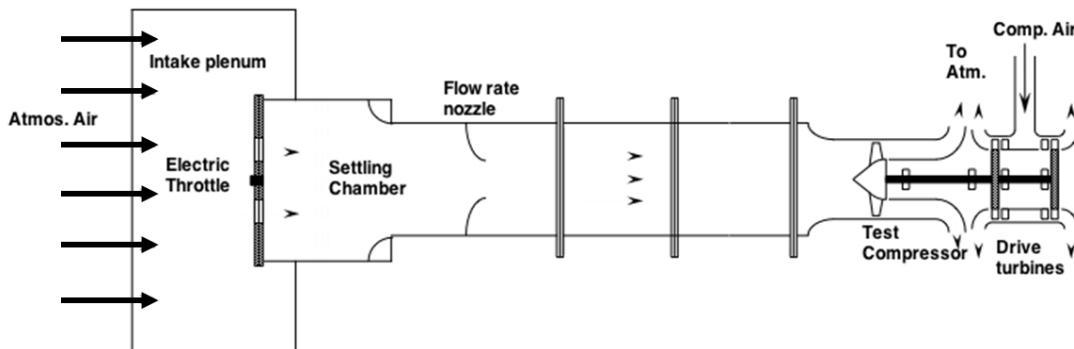


Figure 50. TCR configuration

Each experimental run began with the startup and warmup of the Allis-Chalmers compressor, applying air to the balance piston, and application of lubrication oil to the TASR and drive turbine bearings via an air driven oil mist system. A pre-test checklist is provided in McNab [8] Appendix C.

During each experimental run, one speed line was tested at a time. Each test began by throttling the supply air to the drive turbines to adjust the speed as necessary to

achieve a corrected TASR speed (adjusted for atmospheric temperature of the day) that was within one percent of the desired speed. Data collection began with the upstream throttling valve in the open position which was then incrementally closed to reduce the air mass flow through the TASR. Initial throttling increments were moderate, but as the operating condition approached stall, the throttle was closed in the smallest increments achievable by the electromechanical actuated rotating plate throttling valve. At each throttle position, data measurements were recorded and cross-checked with the CFD-derived performance maps.

C. DATA ACQUISITION AND REDUCTION

Steady-state data was collected using the existing TPL data collection system. An HPVEE data acquisition program developed by Gannon [13] and described by McNab [8] measured the TCR steady-state pressures and temperatures. A brief description is given for completeness. An HP E8404A VXI Mainframe controlled by HPVEE software installed on a PC used a 16-channel multiplexer to read near real-time voltage measurements from the TCR to measure temperature and a counter-totalizer module to measure rotational speed instrumentation. Three ScaniValve DSA 3217/16Px (25psid) pressure bricks were used to enable near real-time monitoring of all pressure probes. The steady-state data was then transferred directly to the PC via ethernet connection for data reduction. The HPVEE data acquisition program then mass-averaged the temperatures and pressures and calculated the stagnation pressure ratio.

Unsteady data was collected from the Kulite Miniature IS Pressure Transducers located in the TASR segment (AS2) using a DAC Express data acquisition system described by Londono [14]. A brief description is given for completeness. All probes were calibrated before each TCR run using 0.2 second samples for successive known backpressures applied to the backside of the probe. During testing, 20 second samples at a speed of 196,608 Hz were recorded on the system's two mainframes for different flow and operating conditions resulting in over a half a million data sample points during each run. Data files were saved in a comma delimited form (*.csv) for exporting to Microsoft Excel and processing in MATLAB. The MATLAB code developed by Londono [14]

was used to reduce the data. Each TASR blade passage was divided equally using 100 points. The mean of the blade passage pressures were transformed into a pressure distribution map by taking all the Kulite pressure signals at each of the points across the blade passage to produce the smooth mean. The final contour plot was formed by sequentially joining and interpolating the pressure averages for each Kulite data set.

VI. RESULTS

A. EXPERIMENTAL RESULTS

Prior to starting the experimental testing of the TASR installed in the TCR increased concern about the stability of the abradable strip material installed in the casing in the blade tip region necessitated the machining of the abradable material to expand the cold-shape TG from the planned 0.51 mm (0.020 in) to 0.91 mm (0.036 in). It was predicted that this would negatively impact the experimentally measured performance of the TASR, but the tradeoff was accepted to ensure the integrity of the TASR blisk.

Performance of the TASR was measured at 60 percent, 70 percent, 90 percent, 95 percent, and 100 percent of the 27,000 design speed. The total-to-total pressure ratio, total-to-total isentropic efficiency, and referred power were plotted versus mass flow rate for each specific test speed. For all the experimental data the greatest source of error was the mass flow instrumentation equating to a two percent error in the measured mass flow rate. The experimental testing completed at 60 percent speed were preliminary evaluations of the TCR operability with the newly installed TASR. Two 60 percent speed tests were conducted. The first evaluation was conducted with a 0.61 mm (0.024 in) TG. The second evaluation was conducted with a larger 0.91 mm (0.036 in) TG which was then used for all other operating speeds. The total-to-total pressure ratio map for the two 60 percent experimental evaluations are shown in Figure 51. Evaluating this figure shows a decrease in measured pressure ratio and an increase in measured mass flow rate as the TG was increased from 0.61 mm (0.024 in) to 0.91 mm (0.036 in). This was expected and would be a good predictor of the expected differences between the numerically derived performance maps modeled with a 0.25 mm (0.010 in) TG and the experimentally derived performance maps conducted with a 0.91 mm (0.036 in) TG.

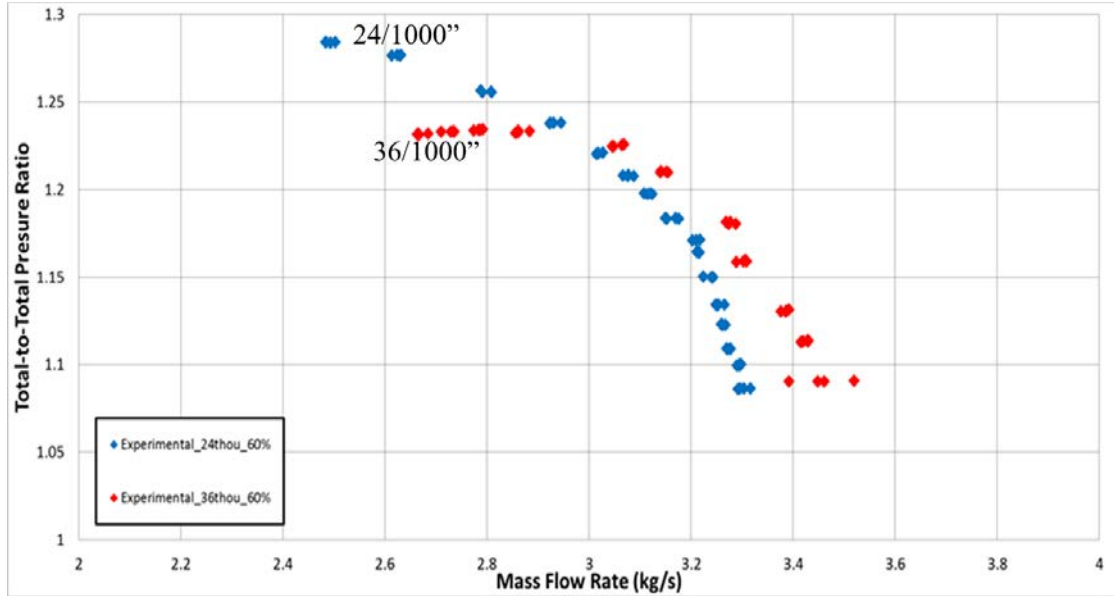


Figure 51. TASR 60 percent design speed experimentally measured total-to-total pressure ratio map

The total-to-total pressure ratio versus mass flow rate is shown in Figure 52. This figure shows the characteristic increase of pressure ratio as the mass flow rate is decreased as a constant rotational speed. The compressor was throttled to stall for all speeds. At 100 percent design speed, the measured peak pressure ratio was 1.69 and mass flow rate range was 7.5 percent. At 70 percent design speed, the measure peak pressure ratio was 1.33 and the mass flow rate range was 18 percent.

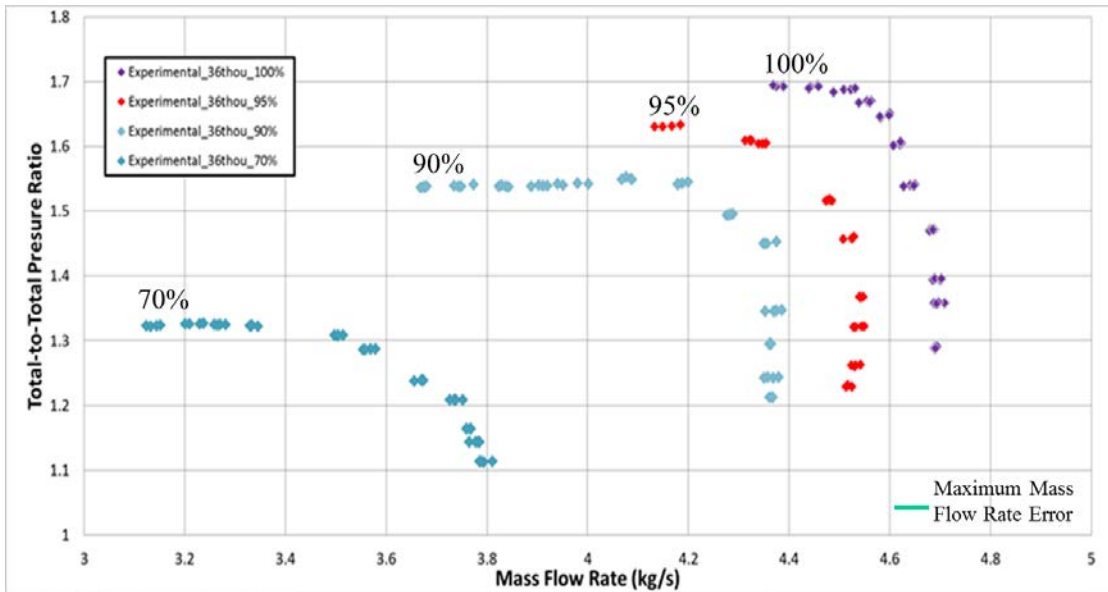


Figure 52. TASR experimentally measured total-to-total pressure ratio map

The total-to-total isentropic efficiency map for the compressor is shown in Figure 53. At 100 percent design speed, the maximum measured efficiency was 74 percent; however, higher efficiencies were measured at 70 percent, 90 percent, and 95 percent. The peak measured efficiency was 84 percent at 70 percent design speed.

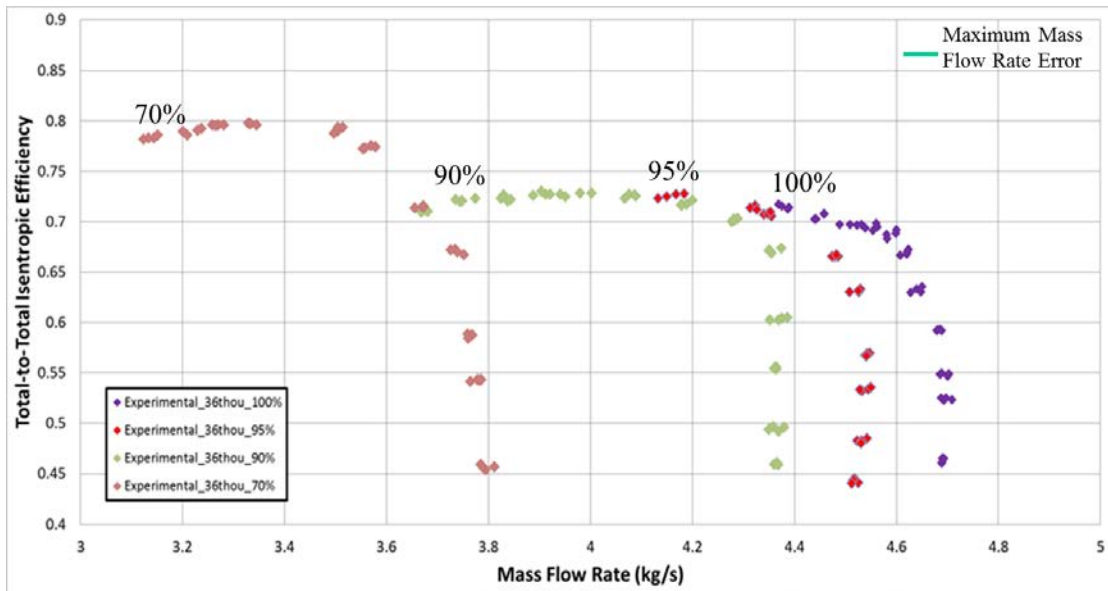


Figure 53. TASR experimentally measured isentropic efficiency map

The power absorbed by the compressor versus mass flow rate for the range of operating speeds is shown in Figure 54. This is the corrected mass flow rate and it should be noted that the actual power absorbed by the TASR was less due to the upstream throttling. At 100 percent design speed the compressor required a corrected peak power of 435kW.

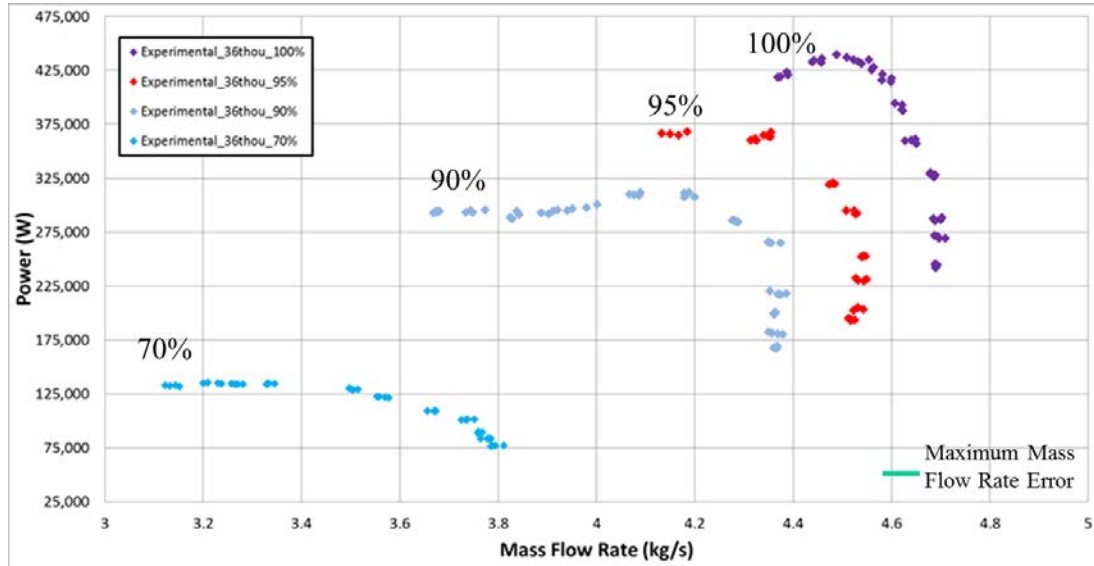


Figure 54. TASR experimentally measured power map

Utilizing the MATLAB code developed by Londono [14] the unsteady Kulite data was analyzed for the 100 percent design speed at the near-stall condition resulting in the contour plot shown in Figure 55. In this figure a strong oblique shock is originating from the LE of the SB and a weaker oblique shock is originating from the LE of the MB.

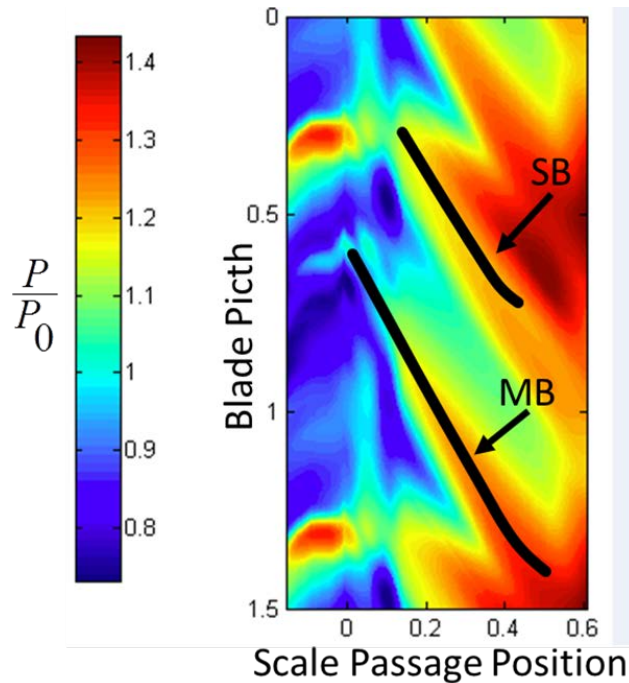


Figure 55. TASR 100 percent speed near-stall experimental contour pressure plot

B. COMPARISON OF CFD TO EXPERIMENTAL RESULTS

This section compares the numerically derived predicted performance of the TASR to the experimentally measured performance. Before proceeding with the comparison, it is important to recall that the numerically derived predicted performance was modeled using a TG of 0.25 mm (0.010 in) but the TASR was experimentally tested with a cold, non-deformed shape TG of 0.91 mm (0.036 in). Additionally, the numerical simulations performed in this study were predictive and time did not permit refining the simulations to try to match the predicted numerical performance to the measured experimental performance.

The numerical results for total-to-total pressure ratio are plotted on the map of the experimentally determined data in Figure 56. As predicted, with a larger TG, the experimental data shows a reduced peak pressure ratio and increased mass flow rate at all operating speeds. At 100 percent design speed the predicted peak pressure ratio was 1.92, but the measured peak pressure ratio was 1.69. The predicted mass flow range was 6.0 percent and the measured mass flow range was 7.5 percent. Neglecting the

pressure ratio reduction and mass flow rate increase, the experimental performance maps and the numerically determined maps matched in characteristic. Although the measured pressure ratio was lower than predicted the measure flow range was higher than predicted. This increased flow range will result in an increased operability range if used in an actual engine.

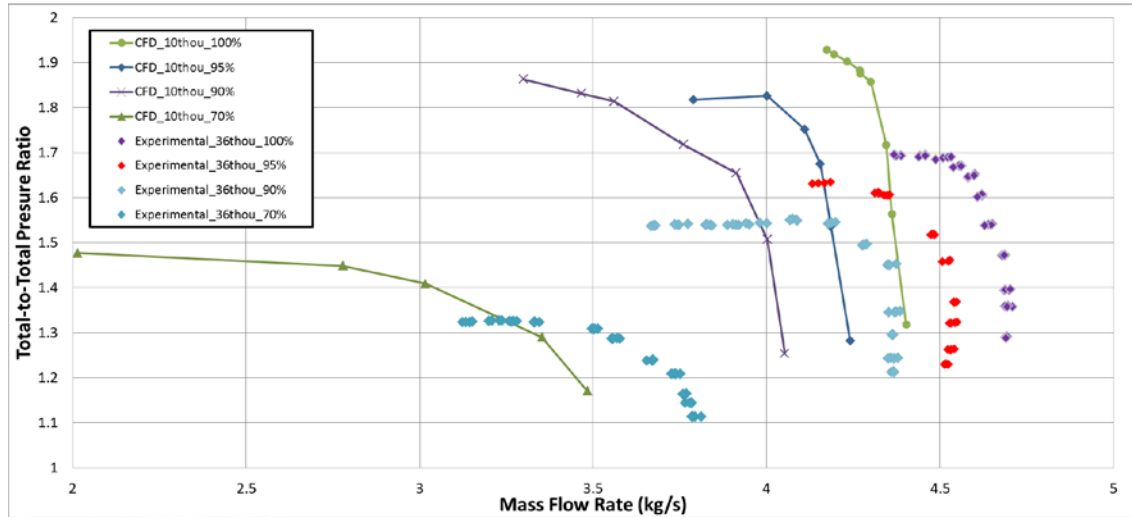


Figure 56. TASR experimentally versus numerically determined total-to-total pressure ratio map

Figure 56 shows the numerical results for total-to-total isentropic efficiency plotted on the map of the experimentally determined data. Again, the larger TG reduced performance and reduced the peak efficiency at all operating speeds but increased mass flow rate. The predicted peak efficiency for 100 percent design speed was 80 percent but the measured efficiency was 72 percent. Again, the experimental performance maps and the numerically determined maps matched in characteristic.

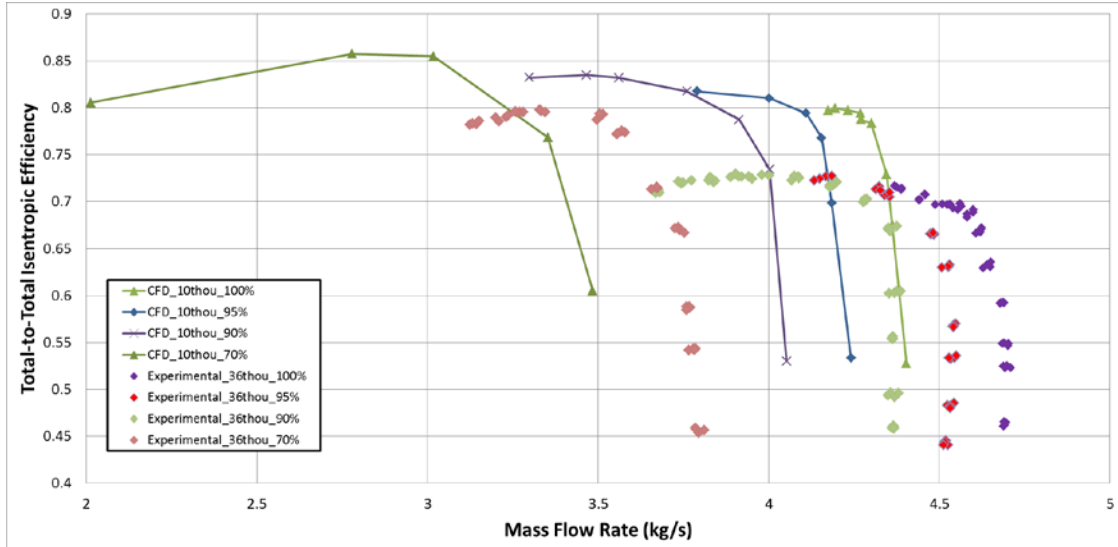


Figure 57. TASR experimentally versus numerically determined isentropic efficiency map

The numerical results for corrected absorbed power are plotted on the map of the experimentally determined data in Figure 58. It is important to recall when analyzing this figure that the actual power delivered to the compressor was less due to the upstream throttling. Therefore, the peak power actually absorbed by the compressor at each operating speed is lower than presented. For example, at 100 design speed the measured corrected peak power absorbed was 425 kW. The measured uncorrected peak power absorbed was 317 kW. The corrected power was calculated using equation (24). The map for each operating speed is shifted to a higher mass flow rate range as predicted due to the increase in TG.

$$HP_C = C_p \cdot \dot{m} \cdot (T_{03} - T_{01}) \quad (24)$$

where C_p is the specific heat of the air and \dot{m} is the corrected mass flow rate.

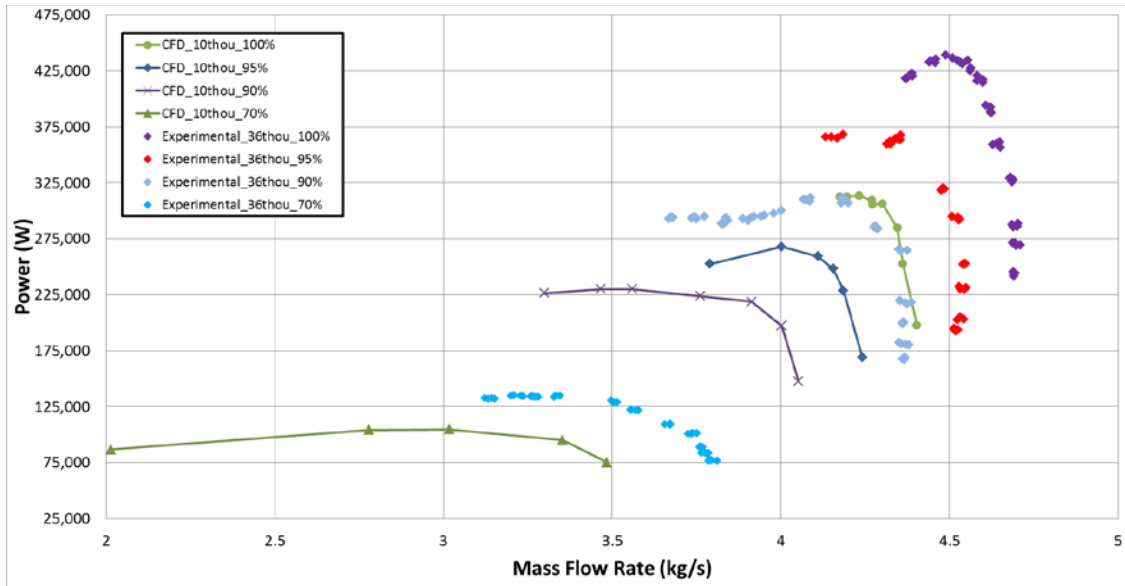


Figure 58. TASR experimentally versus numerically determined power map

The casing contour plot extracted from the numerically derived performance data at 100 percent design speed in the near stall condition is shown in Figure 59. Comparing this figure to experimentally derived contour plot for the same conditions in Figure 54 shows similar flow field characteristics. A strong oblique passage shock wave can clearly be seen starting in the SB LE tip region and a smaller oblique shock can be seen originating from the MB LE tip region. The combination of these shock waves inhibits the fluid flow creating a flow blockage into the passage and setting up a stall condition.

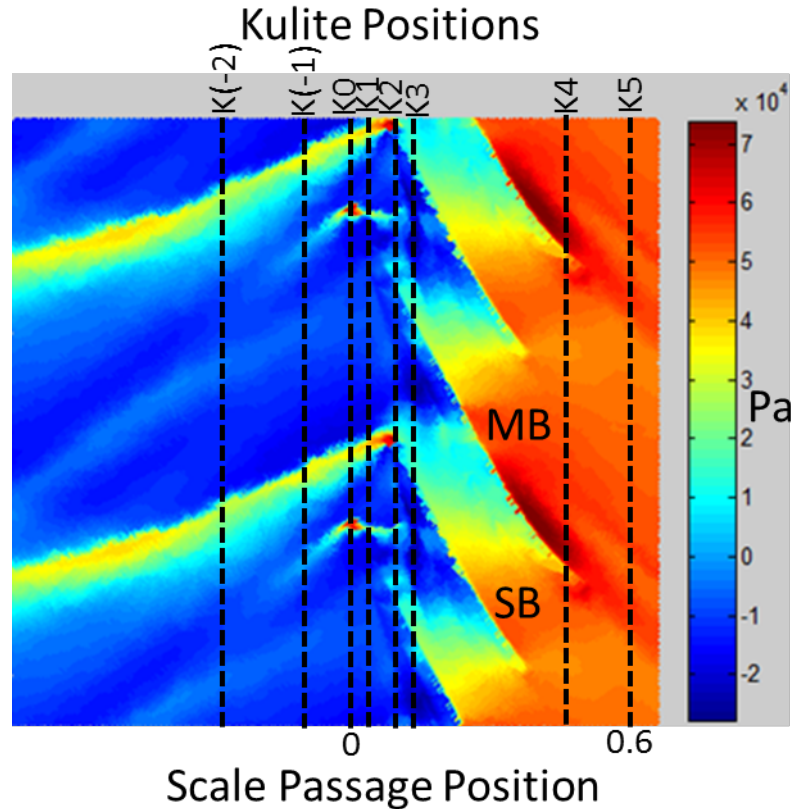


Figure 59. TASR 100 percent speed near-stall CFD contour pressure plot

Additionally, the experimentally measured pressure traces for all 8 Kulites are compared to the numerically derived pressure traces for identical locations on the modeled air wedge in Figures 60–67. A 20-second Kulite data sample was recorded at each operating point; therefore, at 100 percent design speed 108,000 passages are sampled. Each Kulite was sampling at 196,608 Hz equating to 36.4 samples per MB-to-MB passage. The experimental pressure traces were constructed by averaging the 108,000 passage pressures and sampling the average at 100 equally spaced points across the passage. The numerical pressure traces are comprised of approximately 300 data points that are not equally spaced due to the numerical mesh construction at the outer surface of the computational domain. All figures show agreement between the experimental and numerical data, especially just upstream of the rotor at Kulite (-1), where both the MB and SB shocks are captured. Of note in Figure 64 and Figure 65, the numerical pressure traces show the effect of the MB and SB tips at the casing while the

experimental pressure traces do not. This is due to the large cross-sectional area of the Kulite pressure transducer relative to the thin blade tips, their sensitivity, and their slightly recessed locations in the casing. Figure 66 shows remarkable overall agreement, but once again the Kulite traces do not accurately show the location of the main blade. Downstream of the rotor the numerical solution becomes less accurate as the flow becomes more complicated by turbulence, tip leakage vortices, and growing boundary layers.

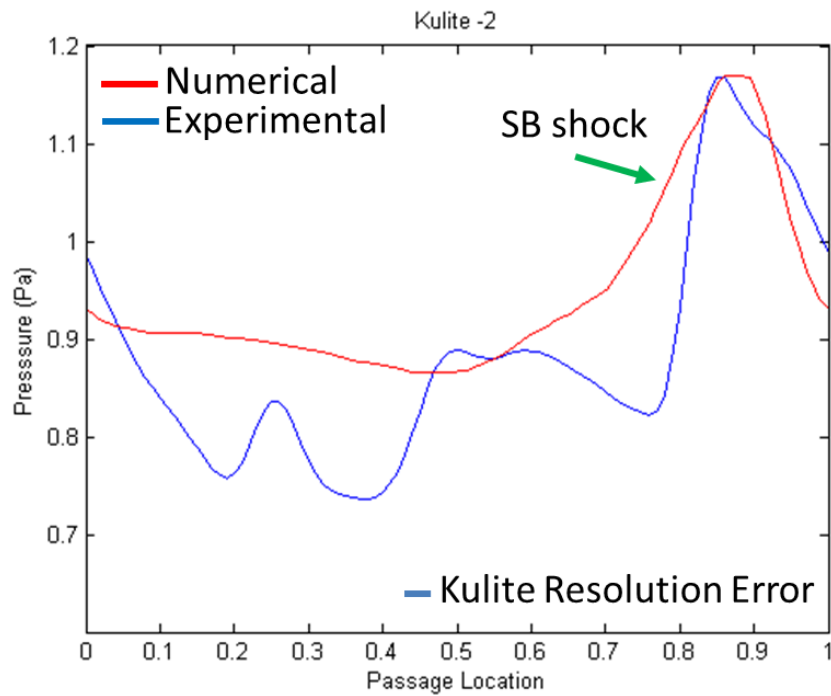


Figure 60. Kulite (-2) experimental versus numerical pressure traces

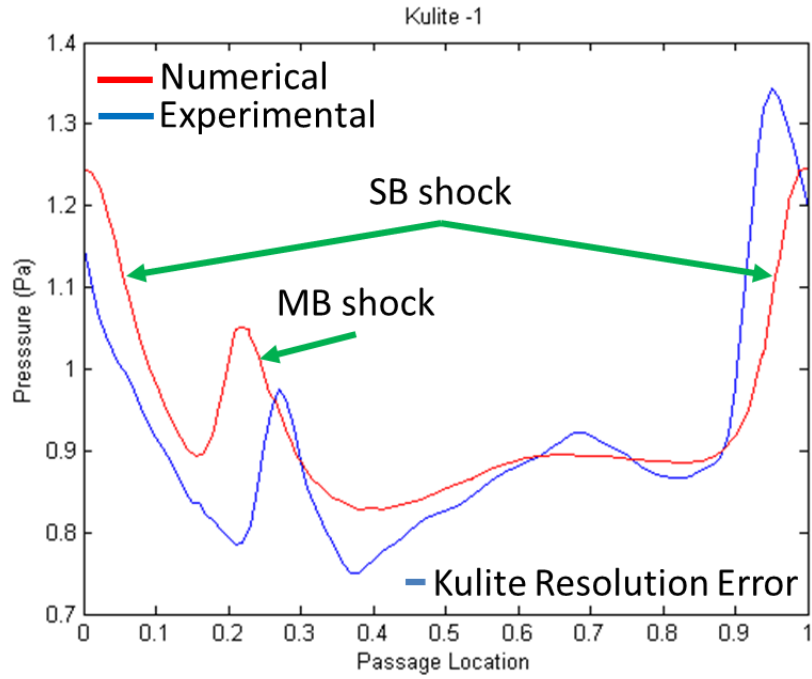


Figure 61. Kulite (-1) experimental versus numerical pressure traces

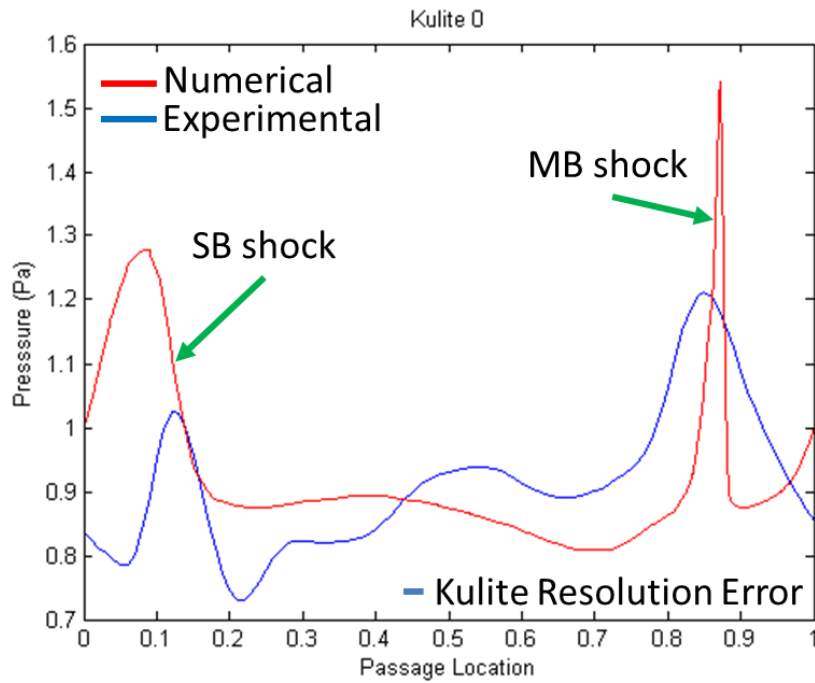


Figure 62. Kulite 0 experimental versus numerical pressure traces

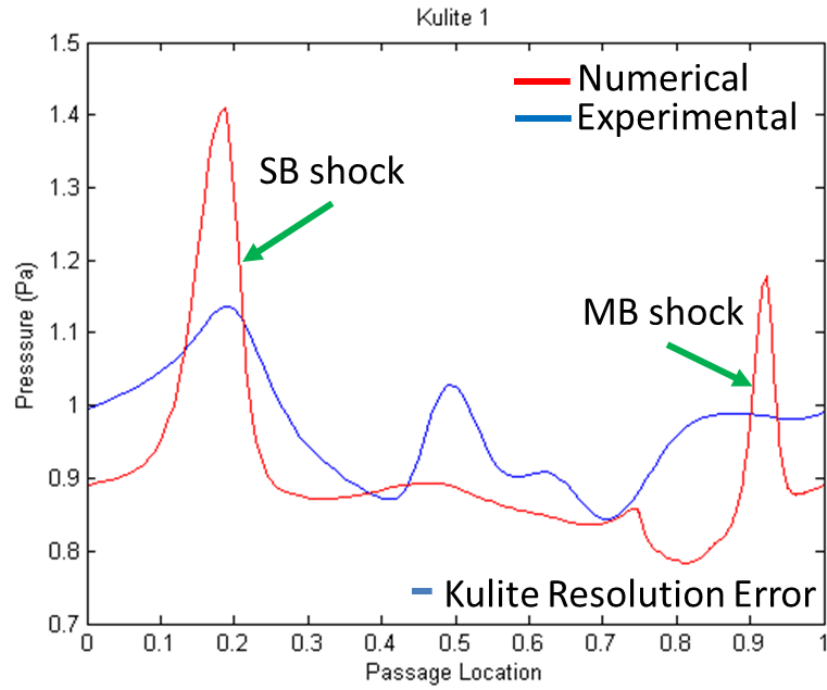


Figure 63. Kulite 1 experimental versus numerical pressure traces

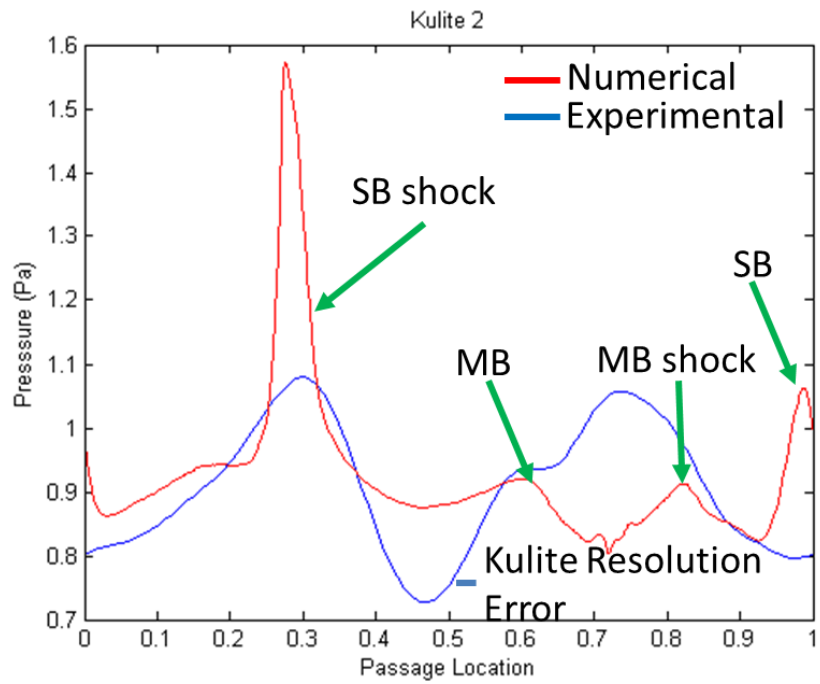


Figure 64. Kulite 2 experimental versus numerical pressure traces

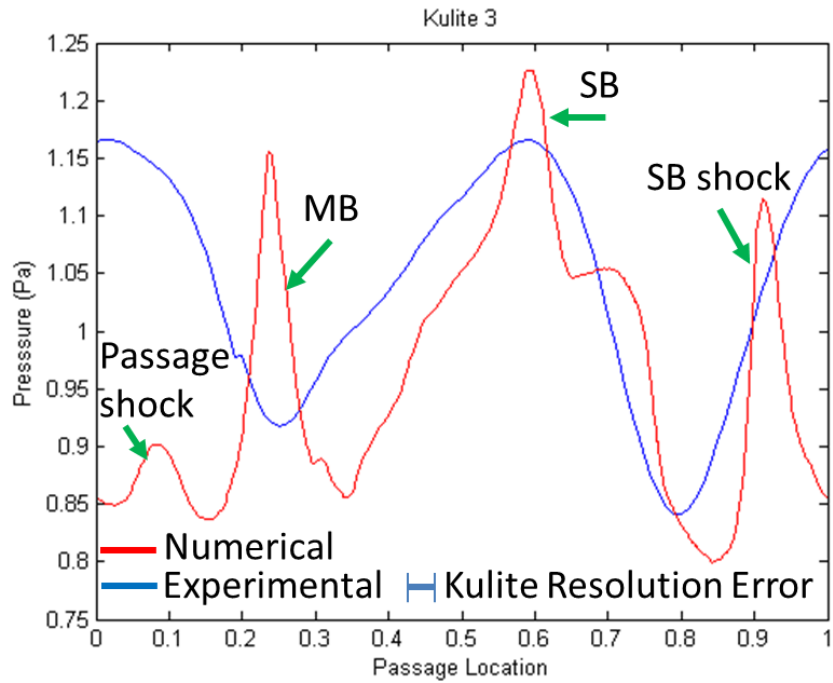


Figure 65. Kulite 3 experimental versus numerical pressure traces

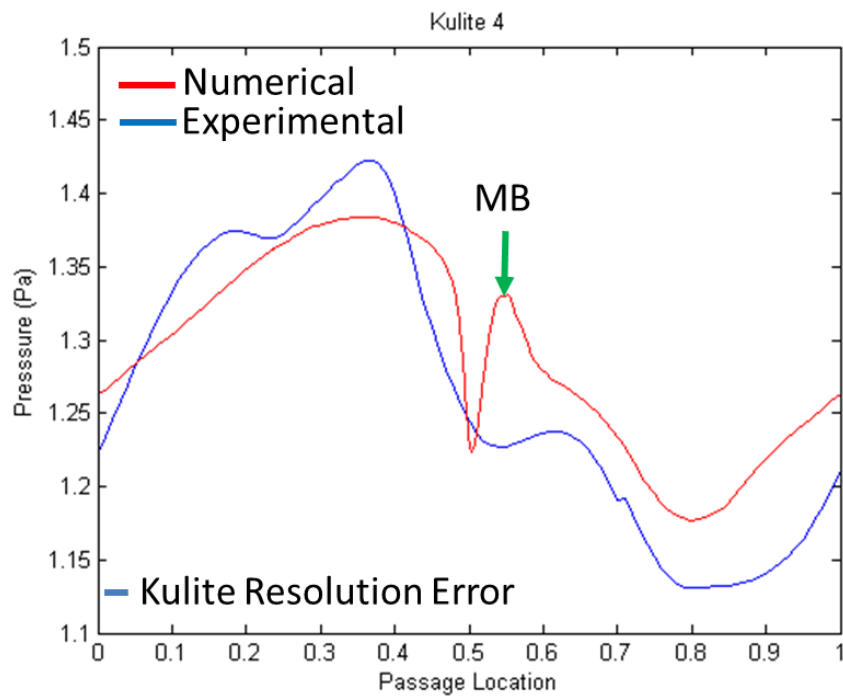


Figure 66. Kulite 4 experimental versus numerical pressure traces

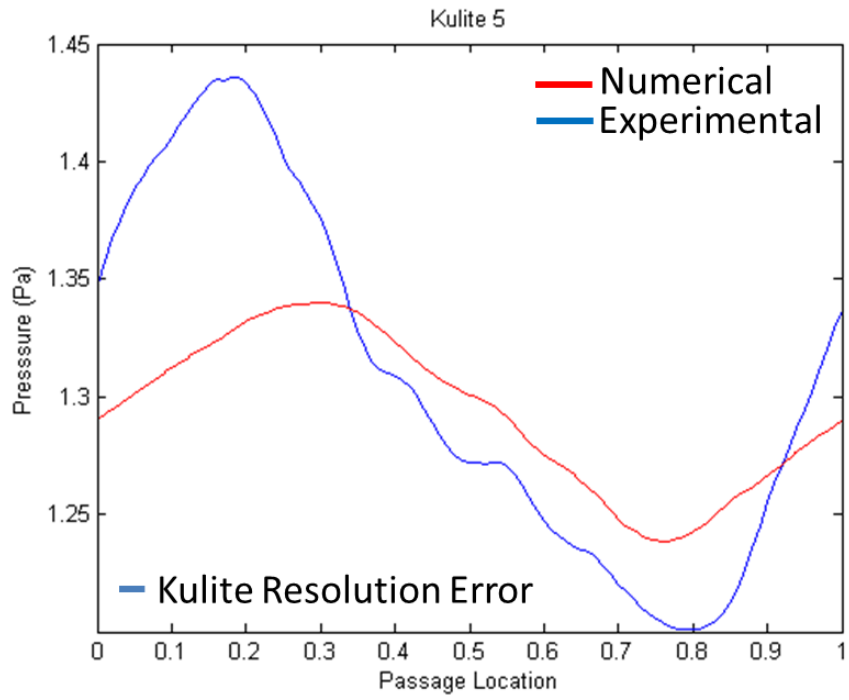


Figure 67. Kulite 5 experimental versus numerical pressure traces

VII. CONCLUSIONS AND RECOMMENDATIONS

A. CONCLUSIONS

This goal of this study was to design, test, and evaluate a transonic axial compressor rotor with splitter blades and all objectives were met. In accomplishing these objectives, several outcomes have been achieved:

1. A new design procedure has been developed and documented that uses commercial-off-the-shelf software for the geometric rendering and analysis of a transonic compressor rotor.
2. MATLAB was used to script the whole design procedure by performing a preliminary tip section design, defining blade parameters, and controlling both SolidWorks and ANSYS-CFX.
3. During a design cycle a complete constant speedline of the compressor was analyzed from open throttle (choke) to stall conditions. This allowed overall performance to be evaluated and compared during each cycle.
4. After restacking of the blade profiles and including fillet radii at the blade roots the design was frozen. A solid blisk (blade and disk) was machined out of 7075-T6 aluminum alloy and tested in the Transonic Compressor Rig.
5. This study advanced the understanding of splitter blade geometry, placement, and performance benefits. In particular, it was determined that moving the splitter blade forward in the passage between the main blades, which was a departure from the trends demonstrated in the few available previous transonic axial compressor splitter blade studies, increased the mass flow range with no loss in overall performance.
6. With a large 0.91 mm (0.036 in) tip clearance, to preserve the integrity of the rotor, the experimentally measured peak total-to-total pressure ratio was 1.69 and the peak total-to-total isentropic efficiency was 72 percent at 100 percent design speed. Additionally, a higher than predicted 7.5 percent mass flow rate range was experimentally measured, which would make for easier engine control if this concept were to be included in an actual gas turbine engine.

B. RECOMMENDATIONS

This work should be used as a starting point for further investigation into the performance advantages of incorporating splitter blades into transonic axial compressor rotors. Recommendations are as follows:

1. That further studies should examine incorporating optimization algorithms into this study's design software tool to allow for 'smart', integrated optimization to be performed in each design increment evaluated. Due to time constraints, the design of this rotor was frozen during the intermediate stages of human-in-the-loop geometry optimization and it is believed that significant performance gains can be achieved through further geometry optimization.
2. That further studies should investigate modifying the TASR numerical model to incorporate the 'hot shape' of the rotor. Rotor blades deform slightly at high angular velocities producing a 'hot shape' that decreases the mass flow through the compressor. This is especially true for this rotor geometry since the splitter blades are thinner than the main blades. Accurate accounting of the deformed hot shape should improve the numerical prediction of performance.
3. That further studies should include aggressive sweep of the splitter blade. During the design phase the splitter blade shape was not changed while its placement in the main passage was being determined analytically, i.e. the splitter blade was not swept forward.
4. That further studies should consider other abradable materials for the inner casing strip in the vicinity of the rotor blade tips. The Dow Corning "One-Part Silicone Rubber Abradable" (3-6891) used in this study proved to be not suitable and required experimental testing be completed with an excessive TG resulting in degraded measured performance of the TASR. This material did not produce a repeatable finished product during successive installations. Additionally, the manner in which it abrades was not compatible with the sharp edges and thin blades of modern high-performance compressor rotors.

LIST OF REFERENCES

- [1] A. J. Wennerstrom, *Design of Highly Loaded Axial-Flow Fans and Compressors*, White River Junction, VT: Concepts ETI, Inc., 2000, p. 69.
- [2] A. J. Wennerstrom, "Some experiments with a supersonic axial compressor stage," *ASME Journal of Turbomachinery*, vol. 109, pp. 388–397, 1987.
- [3] K. L. Tzuoo, S. S. Hingorani, and A.K. Sehra, "Design methodology for splintered axial compressor rotors," in *Gas Turbine and Aeroengine Congress and Exposition*, Brussels, Belgium, 1990.
- [4] J. McClumphy, "Numerical investigation of subsonic axial-flow tandem airfoils for a core compressor rotor," Ph.D. dissertation, Dept. Mech. Eng., Virginia Polytechnic Institute and State University, Blacksburg, VA, 2008.
- [5] N. L. Sanger, "Design of a low aspect ratio transonic compressor stage using CFD techniques," *ASME Journal of Turbomachinery*, vol. 118, pp. 479–491, 1996.
- [6] N. L. Sanger, "Design methodology for the NPS transonic compressor," Turbopropulsion Laboratory, Naval Postgraduate School, Monterey, CA, Tech. Note 99–01, Aug. 1999.
- [7] R. A. Boyter, "Computational fluid dynamic simulation of transonic compressor fan performance," M.S. thesis, Dept. Mechanical and Aerospace Eng, Naval Postgraduate School, Monterey, CA, 2010.
- [8] D. J. McNab, "Experimental testing and CFD modeling of an advanced transonic compressor for military applications," M.S. Thesis, Dept. Mechanical and Aerospace Eng, Naval Postgraduate School, Monterey CA, 2011.
- [9] S. Drayton, "TPL transonic axial compressor rotor design tool software," Turbopropulsion Laboratory, Naval Postgraduate School, Monterey, CA, Tech. Note 13–01, Sep. 2013.
- [10] H. J. Sommer III. (2002, May 14). *Polygeom.m* [Online]. Available <http://www.me.psu.edu/sommer/>
- [11] F. M. White, *Fluid Mechanics*, 7th ed., New York: McGraw-Hill, 2011, p. 364.
- [12] Grossman, B. L., "Testing and analysis of a transonic axial compressor," M.S. thesis, Dept. Mechanical and Aerospace Eng, Naval Postgraduate School, Monterey CA, 1997.
- [13] Gannon, A. J. (private communication), 2013.

- [14] Londono, A., "Near-stall modal disturbances within a transonic compressor rotor," M.S. thesis, Dept. Mechanical and Aerospace Eng, Naval Postgraduate School, Monterey CA, 2011.

INITIAL DISTRIBUTION LIST

1. Defense Technical Information Center
Ft. Belvoir, Virginia
2. Dudley Knox Library
Naval Postgraduate School
Monterey, California